ABSTRACT

Title of Dissertation:	STRUCTURAL DYNAMICS OF TWO FRAGMENT SEQUENCES FROM BACTERIA AND VIRAL RNAs
	Rita Dill, Doctor of Philosophy, 2025
Dissertation directed by:	Theodore Kwaku Dayie Chemistry & Biochemistry Department

This research investigates the many roles and applications of ribonucleic acids (RNAs). Nobel Prize recognized discoveries and recent advances in biomedicine underscores RNA's emerging significance as a key molecule for pharmaceutical innovation and vaccine development. This thesis focuses on the structural dynamics of RNA molecules ultimately relevant to major global health concerns of antibiotic resistance and Human Immunodeficiency Virus (HIV) infection. In addressing antibiotic resistance, the conformational flexibility of prokaryotic rRNA sequence targeted by antimicrobials and those derived from an off-target eukaryotic rRNA sequence was characterized using Nuclear Magnetic Resonance (NMR) spectroscopy. NMR can characterize both local and global RNA dynamics across multiple timescales. These results may contribute to improving the efficacy of RNA-targeted antimicrobials. Similarly, the conformational flexibility of an RNA sequence specific to HIV type 2 was examined using NMR spectroscopy to gain deeper insight into its

dynamic properties. Characterizing the structural dynamics of these HIV type 2 RNA may inform strategies to enhance the efficacy of RNA-targeting therapeutics and expand the existing body of knowledge regarding their cellular function. Such insights could ultimately facilitate the development of drugs designed to recognize and bind biologically relevant HIV type 2 RNA conformations. Finally, this work integrates an educational component that details pedagogical strategies for teaching advanced RNA-related topics, namely solution nuclear magnetic resonance (NMR) spectroscopy dynamics experiments and NMR relaxation data analysis to undergraduate students.

STRUCTURAL DYNAMICS OF TWO FRAGMENT SEQUENCES FROM BACTERIA AND VIRAL RNAS

by

Rita Dill

Dissertation submitted to the Faculty of the Graduate School of the
University of Maryland, College Park, in partial fulfillment
of the requirements for the degree of
Doctorate of Philosophy,
2025

Advisory Committee:

Professor Theodore Kwaku Dayie
Professor Jeffery Davis
Assistant Professor Jinwoo Lee
Associate Professor Myles Poulin
Professor Antony Jose

Dedication

“The Christian shoemaker does his duty not by putting little crosses on shoes but by making good shoes because God is interested in good craftsmanship” -Martin Luther

Acknowledgements

There is little time and many I could acknowledge, but the hour to submit the thesis is at hand. I simply acknowledge the people of heightened importance relative to the nature of my graduate studies: Dr. Dayie, Dr. Osano, and Daniel Abebe.

Table of Contents

List of Tables

List of Figures

List of Illustrations

List of Abbreviations

A-site	Aminoacyl Site
AIDS	Acquired Immunodeficiency Syndrome
CPMG	Carr-Purcell-Meiboom-Gill
Cryo-EM	Cryo-Electron Microscopy
E-site	Exit Site
E. coli	Escherichia Coli
FRET	Fluorescence Resonance Energy Transfer
GBD	Global Burden of Disease
GLASS	Global antimicrobial resistance and use surveillance system
HIV	Human Immunodeficiency Virus
mRNA	Messenger Ribonucleic acid
NMR	Nuclear Magnetic Resonance
NOE	Nuclear Overhauser Effect
P-site	Peptidyl Site
PDB	Protein Data Bank
R_1	Longitudinal Relaxation Rate
R_2	Transverse Relaxation Rate
RNA	Ribonucleic Acid
SAXS	Small Angle X-Ray Scattering
smFRET	single-molecule Fluorescence Resonance Energy Transfer
TAR	Trans-activation Response Element
tRNA	Transfer Ribonucleic acid
USD	Unites States Dollars
UTP	Uridine Triphosphate
UV	Ultra-Violet
WHO	World Health Organization

Chapter 1

1.0 Focus of the chapter

I have focused on the binding site within the Aminoacyl- site (A-site) in rRNA and the uracil bases within the TAR-2 sequences of HIV-2 RNA. Both of which are RNA sequences of interest for drug development of antivirals and antimicrobials. In this chapter, I outline the urgency of antibiotic resistance and discuss how specific antimicrobials target the A-site and cause the production of aberrant proteins, the need to develop new drugs that specifically target HIV-2, and dynamics previously studied on the TAR-2 sequence.

1.1 Antibiotic resistance: a void in drug development and its state of urgency

The golden age of antibiotic development (1930-1980's) was a magnificent time filled with countless discoveries of new antimicrobials suitable to tackle all manner of bacteria[1-2]. Despite the exciting breakthroughs which promised resolution to countless illnesses, the impending potential for antibiotic resistance always lay ominously on the horizon. Antibiotic resistance may be defined as bacteria which are no longer susceptible to medicinal approaches of eradication [3]. Antimicrobial resistance is associated with over a million deaths globally in the year 2022 alone [5]. The recent Global Burden of Disease (GBD) findings highlight that, despite noble attempts, the world has yet to curb antibiotic resistance [5]. The World Health Organization (WHO), in agreement with these reports, has declared antibiotic resistance to be a major public health threat [6]. Additionally, the Global antimicrobial resistance and use surveillance system (GLASS) report, notes that the ramifications of antibiotic resistance may accrue healthcare costs of a trillion USD by the year 2050 [6].

There are over ten classes of antimicrobials; yet all classes have been documented to suffer from antibiotic resistance [13]. WHO has emphasized the urgency to address antibiotic resistance, and there are many means by which this can be accomplished. One approach to solving the public threat of antibiotic resistance is through the improvement of efficacy in currently existing drug classes [14-17].

While both Gram-negative and Gram-positive bacteria can become resistant to antimicrobials, data has shown that Gram-negative bacteria tend to become resistant more often than Gram-positive [18]. This may be due to some structural differences between the two [18]. With this being noted there is a need to prioritize Gram-negative bacteria when developing approaches to solving the problem of antimicrobial resistance. One type of Gram-negative bacteria that is resistant to multiple antibiotics. is *Escherichia. coli (E. coli).*

1.2 Antimicrobials capitalize on the biological process of protein synthesis

While most antibiotic classes target proteins, RNA can also adopt elaborate structures, making RNA suitable for drug targeting [19]. Antimicrobials can bind at a ribosomal site in either the Aminoacyl site (A-site) of the 16S rRNA within the 30S small subunit, or the Peptidyl site (P-site) or the Exit (E-site). Some of the Antimicrobials that currently bind to the rRNA of bacteria include Chloramphenicol, Puromycin, Lincomycin and Clindamycin, Tetracycline, and Paromomycin [20] (**Figure 1.1**). Paromomycin binds to the A-site of the rRNA in the place of the incoming amino-acylated tRNA (**Figure 1.2**) [21]. This binding may lead to the eventual production of aberrant proteins [22-24]. Aberrant proteins have the potential to kill cells [24].

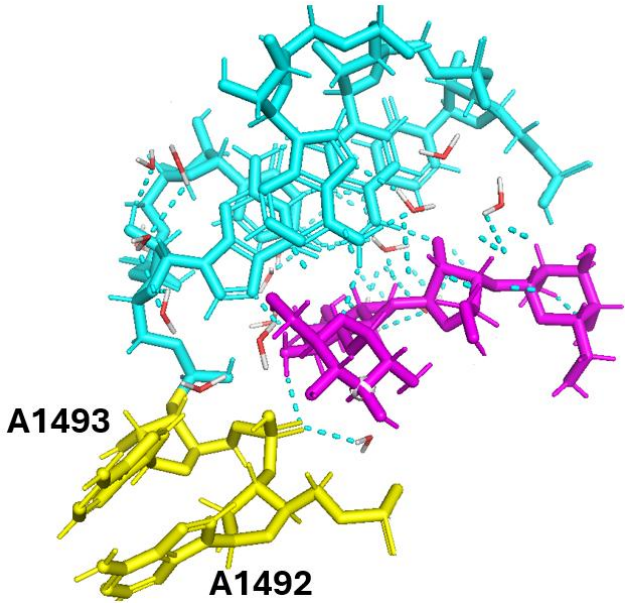

Figure 1.1 Protein data bank (PDB) structure 1J7T shows the contacts made between the aminoglycoside, Paromomycin (Magenta) and the rRNA fragment (cyan). We draw attention to the contacts made by water-bridged hydrogen bonds between the prokaryotic A-site's adenine 1942 (yellow) and 1493 (yellow). The red and white structures represent the water molecules which bridge hydrogen bond contacts (some hydrogen bonds may be obscured due to the angle of image).

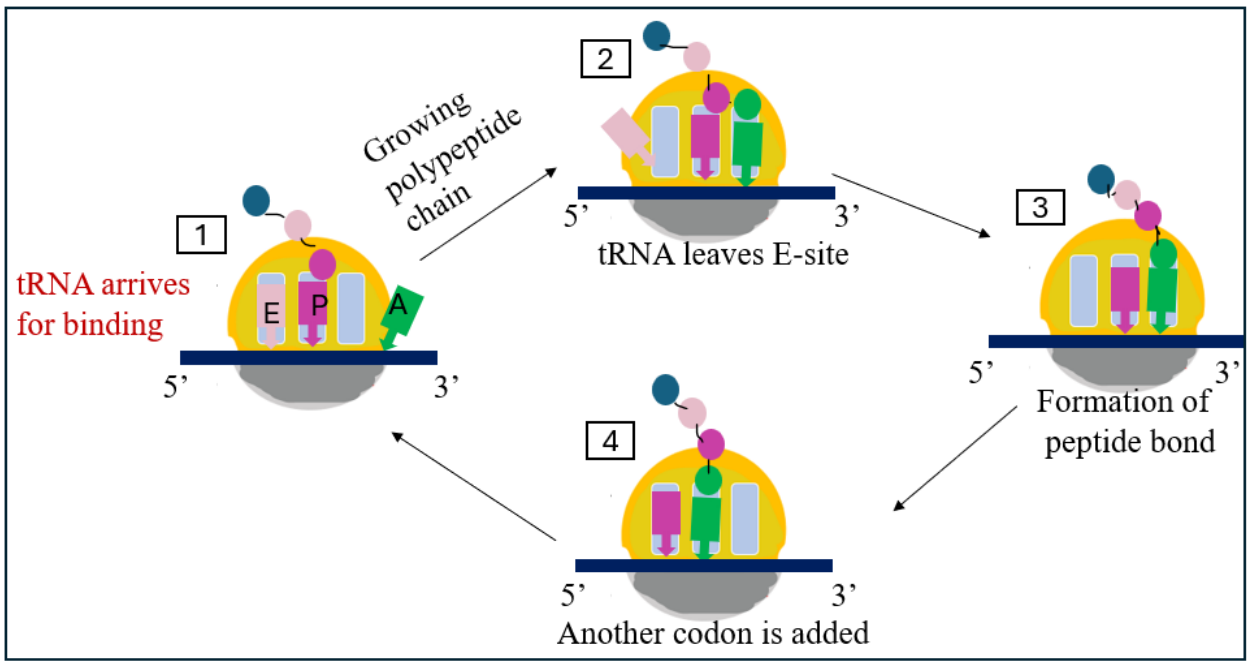

Figure 1.2 The typical process of translation at the ribosome would be halted at step 1 in the event a drug were to bind to the adenines 1492 and 1493 [127]

The typical means by which cells make proteins, for the sustainment of life, is through non-membrane bound organelles called ribosomes (**Figure 1.3**) [25]. Ribosomes can be found in the cytoplasm of prokaryote and eukaryote cells and exist in the mitochondria of eukaryotes. The steps by which the ribosomes synthesize proteins remain fundamentally the same regardless of where the ribosome is in the cell. The ribosome structurally consists of two main subunits: The large subunit and the small subunit. These subunits are made of ribosomal RNA and ribosomal proteins. Within either of these subunits exists the Aminoacyl site (A-site), the Peptidyl site (P-site) and Exit site (E-site). These three sites serve as the assembly line by which proteins are manufactured; and were first discovered by Warner & Rich in 1964 [26]. The manufacturing process begins at the A-site and can be divided into three main stages consisting of initiation, elongation and termination.

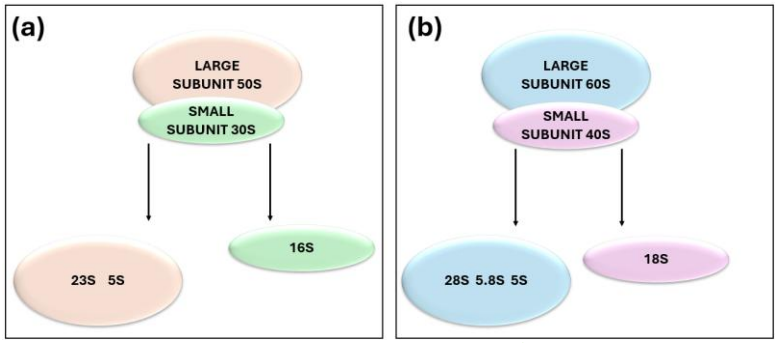

Figure 1.3 (a) Prokaryotic ribosome and **(b)** Eukaryotic ribosome and their rRNAs[53]

The initiation of translation starts with the first tRNA (carrying methionine) binding to the P site, not the A site, on the ribosome. The A site (Aminoacyl site) is for the next incoming tRNA during elongation, while the P site (Peptidyl site) holds the growing chain, and the E site (Exit site) is where tRNA leaves. A charged transfer RNA (tRNA) carrying an anticodon binds to a complementary codon on the messenger RNA (mRNA) strand. The two specific adenine residues that ensure the correct anticodon binds to the complementary mRNA's codon are A1492 and A1493 of the 16S ribosomal RNA (rRNA) in prokaryotes (Figure 1.4) [27]. These invariant adenines form A-minor type interactions in the minor groove of the first two base pairs of the codon-anticodon helix. This interaction acts as a crucial proofreading mechanism by sterically monitoring the geometry of the helix; thus, ensuring the accuracy of the protein product made [27]

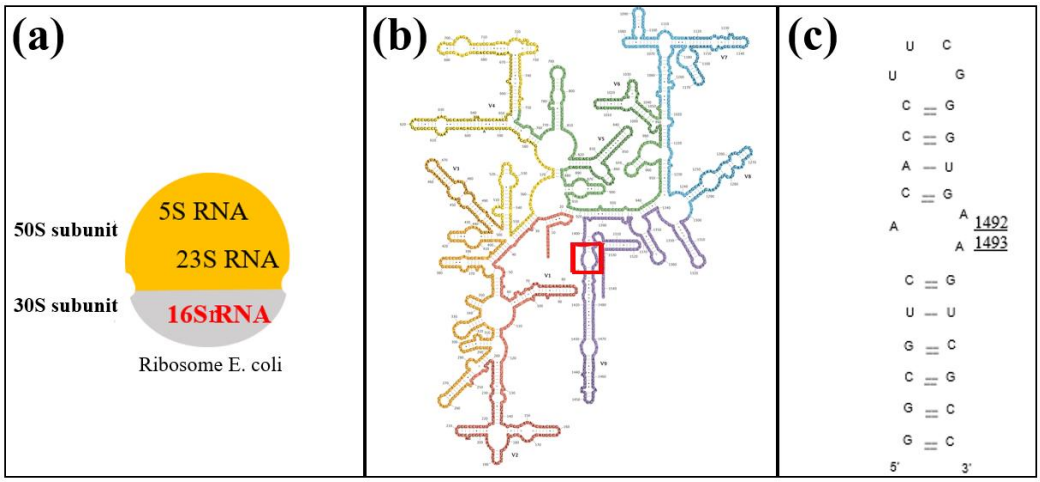

Figure 1.4 (a) Shows a simplified model of a bacterial E. coli ribosome with identifying labels. **(b)** Adapted from textbook [53] the 16S rRNA is shown with a red box denoting the location of the A-site sequence. **(c)** a fragment of the A-site sequence which contains the key adenines 1492 and 1493.

Several biophysical studies have shown that adenines 1492 and 1493 will bulge out into an extra helical conformation to hydrogen bond with the incoming amino acylated tRNA's codon [27-30]. The codon-anticodon interaction is checked by A1492 and A1493 in the A-site, and only after this verification and subsequent peptide bond formation does the ribosome move, effectively shifting the tRNAs to the P and E sites, continuing the elongation cycle [27]. (**Figure 1.5**). At termination phase of translation, a stop codon (UAA, UAG, UGA) enters the ribosome's A-site. This triggers release factors to bind, which causes the ribosome to release the completed polypeptide chain and dissociate, ending the process.

Previous work [167] from the Pilch group underscores the significance of the intra and extra helical movements. The Pilch group investigated how aminoglycosides affect the conformational dynamics of these two adenines A1492 and A1493. They substituted the adenine at position 1492 in this A-site with the fluorescent base analogue 2-aminopurine (2AP). Using steady-state and time-resolved 2-aminopurine fluorescence spectroscopy, they quantified the lifetimes of the intrahelical and extra helical states in the absence and presence of four aminoglycosides. These aminoglycosides served as representatives of the four subclasses of aminoglycosides.

Their data showed that, with or without drugs present, 1492 and 1493 exchange between intra and extrahelical conformations. When testing with aminoglycosides, it was noted that the average fluorescence intensity values decreased. This signaled a reduction in 1492 and 1493's mobility, and a stabilization of an extra-helical conformation. This very immobilization correlated with the potency of the drugs. This suggests that restricting the motion of 1492 and 1493 into an extra-helical state is a key determinant of antibacterial activity. However, fluorescent tags have been known to perturb RNA dynamics; thus to re-monitor this observation first without drugs and later with drugs would be meaningful to compare with the work of the Pilch lab This study serves as my motivation to observe the lifetimes of

the intra and extra helical states without drugs using solution NMR; solution NMR is a minimally perturbing technique suited for dynamics in solution.

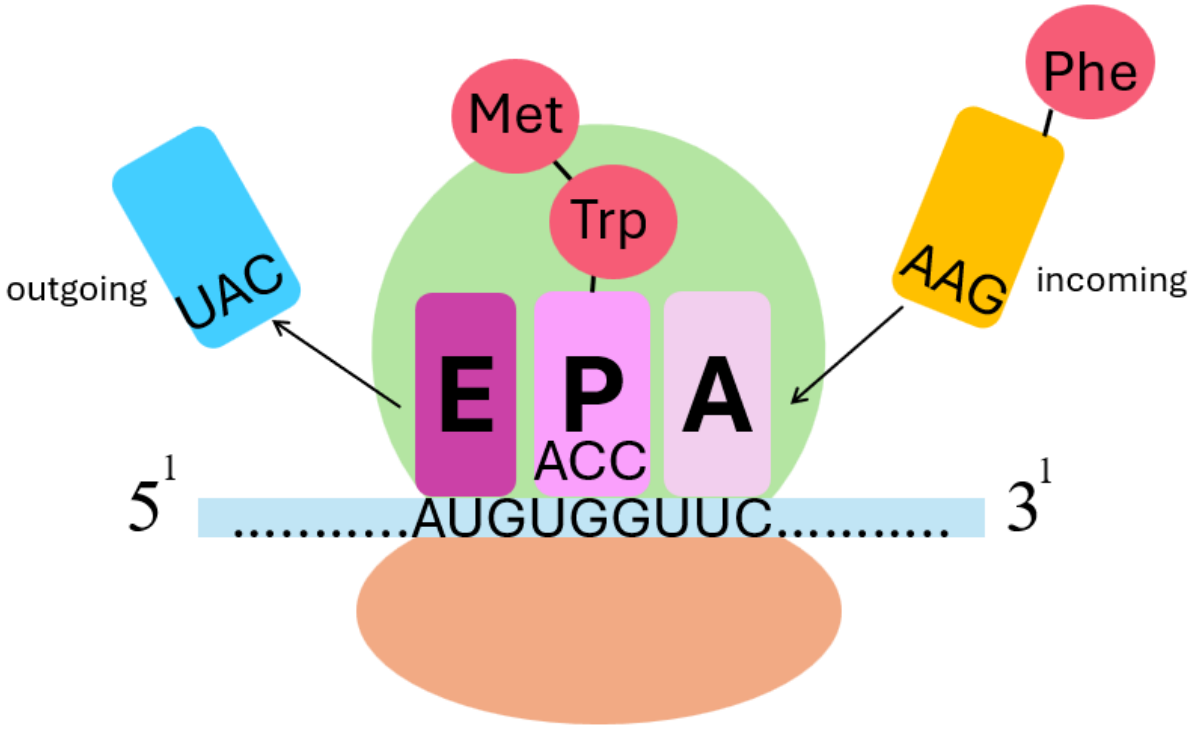

Figure 1.5 The process by which an incoming tRNA and its anticodon bind to the appropriate mRNA's codon [126]

In the case of ribosomes found within eukaryotic cells, it is desirable to make non-aberrant proteins, however if one wishes to impede bacteria cells, then making toxic proteins may be capitalized on. Several broad-spectrum Gram-negative antimicrobials are designed to engage adenines 1492 and 1493 by binding to them through hydrogen or water-bridged hydrogen bonds [20-21]. While the A-site may be the intended target of the antimicrobials, the antimicrobials are not full-proof. There have been reports of off-targeted binding in the corresponding positions in the human 18S rRNA or the mitochondrial 12S rRNA [31-34]. These off-targeted bindings can be due to pre-existing genetic mutations in sequences [31-34]. It is hopeful that understanding the movement of adenines 1492 and 1493 may lead to improvements in these antimicrobials and specifically to Gram-negative multidrug resistant bacteria, such as *E. coli.* While there

is a vast amount of Gram-negative multidrug resistant bacteria, this thesis will focus on the *E. coli* bacteria as a model bacterium. Better understanding of the "flipping in and out" conformation of A1492 and A1493 may aid in designing new, more effective antibiotics with reduced side effects and the ability to overcome resistance.

1.3 HIV: A global epidemic and its deficit in treatment options

While WHO declared antibiotic resistance to be a major threat, it has delineated human immunodeficiency virus (HIV) to be a global epidemic [35]. HIV is a chronic virus which weakens the immune system and if untreated, leads to AIDS [36]. HIV is generally transmitted through blood, birth and bodily fluids. HIV exists in two major strains: HIV type 1 (HIV-1) and HIV type 2 (HIV-2) [36-37]. While both may result in AIDS, there are some noteworthy differences between the two. HIV-2 is slower to show phenotypic expression when compared with HIV-1. A delay in the expression of outward symptoms can be challenging as this may result in the infected individuals unknowingly transmitting the virus to others and not receiving treatments in efficient timing [38]. Another difference between the two strains can be found in their lack of pharmacological therapy options [39-40]. To date there are 6 major classes of FDA approved medicinal options for HIV patients. These six classes are known as follows: Non-nucleoside Reverse Transcriptase Inhibitors (NRTIs), Nucleoside Reverse Transcriptase Inhibitors (NNRTIs), Protease Inhibitors, Fusion Inhibitors, CCR5 Antagonists, Integrase Strand Transfer Inhibitors (INSTIs), Post-attachment Inhibitors and Capsid Inhibitors (**Table 1.1**). They all possess varying mechanisms of action. These eight classes all encounter resistance. These medications' side effects along with other rationale have been documented as discouraging patients from consuming their medication consistently as directed [41-42]. Inconsistent medication doses have been shown to cause viral resistance [43]. Surely, there is a need to develop high performing medication that is effective and can treat both HIV-1 or HIV-2.

Table 1.1 A summary of the different first line of defense drug classes used to treat HIV. The applicability of these drugs to treat HIV-1 and HIV-2 is delineated. [44-63]

HIV-1 or HIV-2 Applicable	Class of HIV Medication	Mechanism of Action
HIV-1 & 2	NRTIs	Insert themselves into DNA sequence; interfering with reverse transcriptase
HIV-1	NNRTIs	Bind to the active site on reverse transcriptase
HIV-1 & 2	Protease Inhibitors	Prevent the creation of new viral particles by binding to protease enzyme
HIV-1	Fusion Inhibitors	Bind to the HIV envelope protein to restricts the conformation changes of Gp41 conjoining with CD4 T cells
HIV-1 & 2	Integrase Inhibitors	Binds to enzyme integrase to prevent DNA from being inserted into host cells
HIV-1 (low efficacy against HIV-2)	Capsid Inhibitors	Bind to the capsid of HIV to prevent the release of RNA used to make the viral DNA

1.4 RNA is a promising choice to address needs for treatment options regarding antimicrobials and HIV-2

The global threat of antimicrobials resistance coupled with the ever-present potential to spread HIV-2, signals the need for a solution. Ribonucleic acid (RNA) has proven a viable drug target through its role in the COVID-19 vaccine development [64]. Perhaps, RNA may serve as a suitable therapeutic target for antibiotic resistance and HIV-2. While it is common to manufacture antimicrobials towards targeting proteins, RNA proves itself a suitable alternative is through the many tertiary structures it can form: G-quadruplexes, pseudoknots, loops, bulges, triple helices and many others [19].

Additionally, RNA is produced in the cell before proteins [66]. This implies that targeting RNA would be attacking in an upstream fashion rather than downstream as with protein targeting. Some illnesses specific to RNA do not possess proteins to target; this can be seen in examples of noncoding RNA. Finally, while most antimicrobials do target proteins, targeting RNA would make way for the novel therapeutics which may result from RNA drug discoveries. It is worthwhile to underscore that RNA is not being proposed to be superior to protein targets; but rather it is proposed that RNA may be another

excellent target for antimicrobials. The key objective is to either improve performance of the currently available drug classes or to develop novel drug classes which target RNA.

RNA may indeed prove powerful in addressing antibiotic resistance, but also in serving as a drug target for the viral strand with fewer medication options: HIV-2. HIV 1 and 2 both have strikingly similar Transactivation Response element RNA (TAR-1 and TAR-2 respectively) sequences. The sequences (**Figures 1.6 and 1.7**) of TAR are located at the 5' end of the HIV (1 or 2) genome. The TAR sequence is within the R (repeat) region of the 5' long terminal repeat (LTR) downstream from the transcription starting site. The TAR forms a stem loop structure that binds with the protein, Tat. This binding event recruits enzymes that proliferate viral transcription.

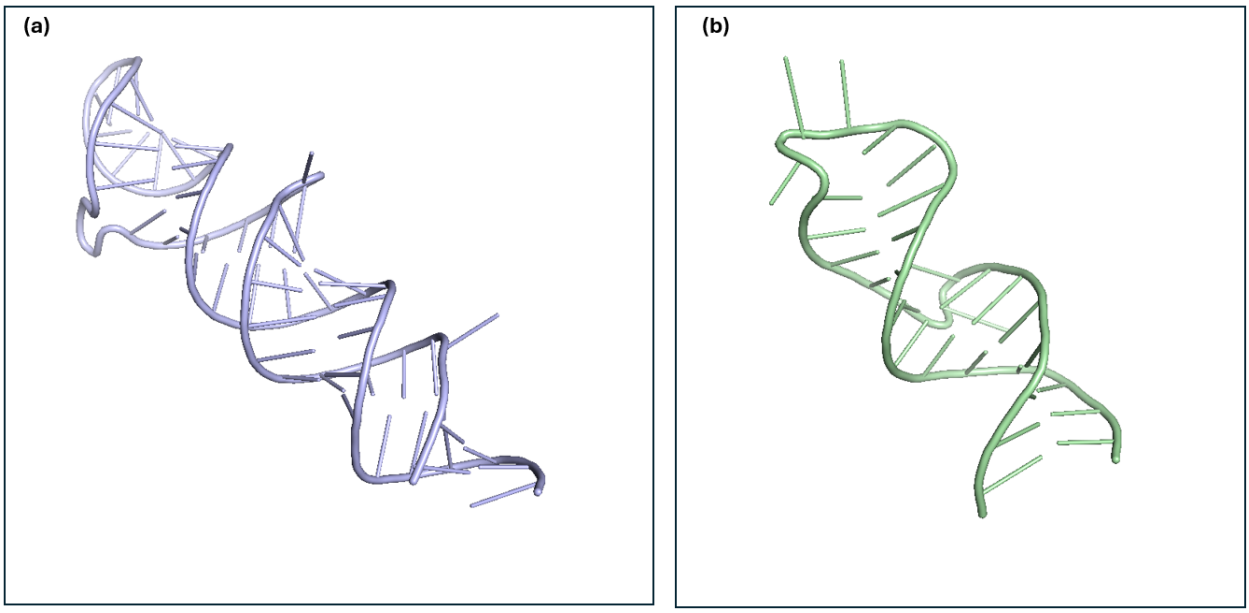

Figure 1.6 (a) HIV-1 (PDB: 9DE7) and **(b)** HIV-2 (PDB: 1AKX) TAR RNA tertiary structures[71,75]

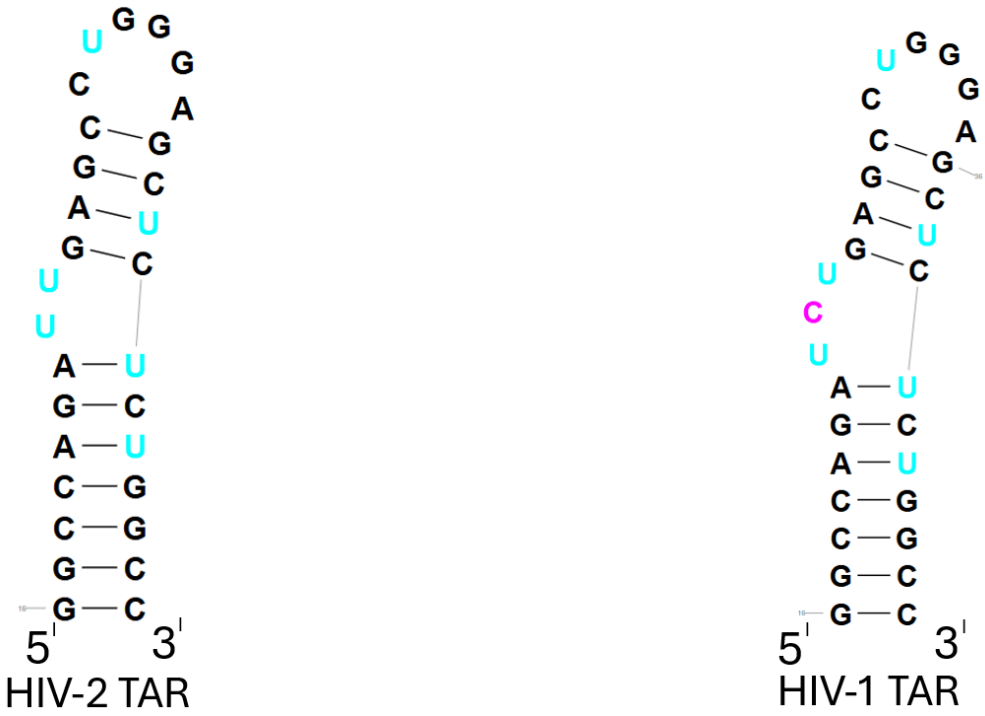

Figure 1.7 Comparison of the secondary structure HIV-1 and HIV-2 fragment sequences of RNA. The color magenta indicates the singular nucleotide difference between the two sequences. The color cyan highlights the uracils which are of particular focus throughout this thesis.

The TAR RNA found in HIV is special. Despite the mutations that take place in the mRNA of HIV-1 and HIV-2, the TAR sequences remain conserved [73]. An obstacle in developing suitable binding drugs may arise if the sequence landscape is often changing due to the frequency of mutations to the sequences. The conserved nature of the TAR RNA sequences makes the TAR RNA appear to be an attractive option for the development of binding drugs. Already it has been discovered that the TAR RNA serves as a critical site of binding within the framework of HIV replication[74]. The TAR RNA is located within the HIV particle, within its capsid lies the HIV RNA. The TAR sequence is located on the 5' end of the untranslated region of the sequence.

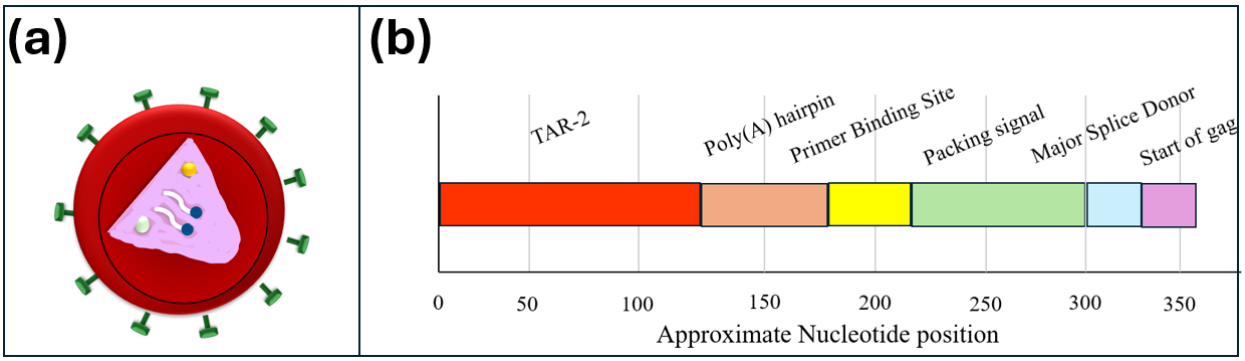

Figure 1.8 **(a)** shows a simplified model of the HIV particle: glycoproteins (green), capsid (pink), enzymes are circular shaped, and RNA (white) (**b)** depicts the nucleotide positioning of the TAR sequence.

Within TAR-1 is a binding pocket of nucleotides that participate in a binding reaction with a protein, Tat [75]. This binding is believed to take place between the nucleotides, U23, G26, A27, U38, C39 of the TAR-2, and an arginine-rich motif (**Figure 1.9**) in Tat [75]. The protein, Tat, is important because as a trans activator it activates the transcription needed for HIV replication[74].

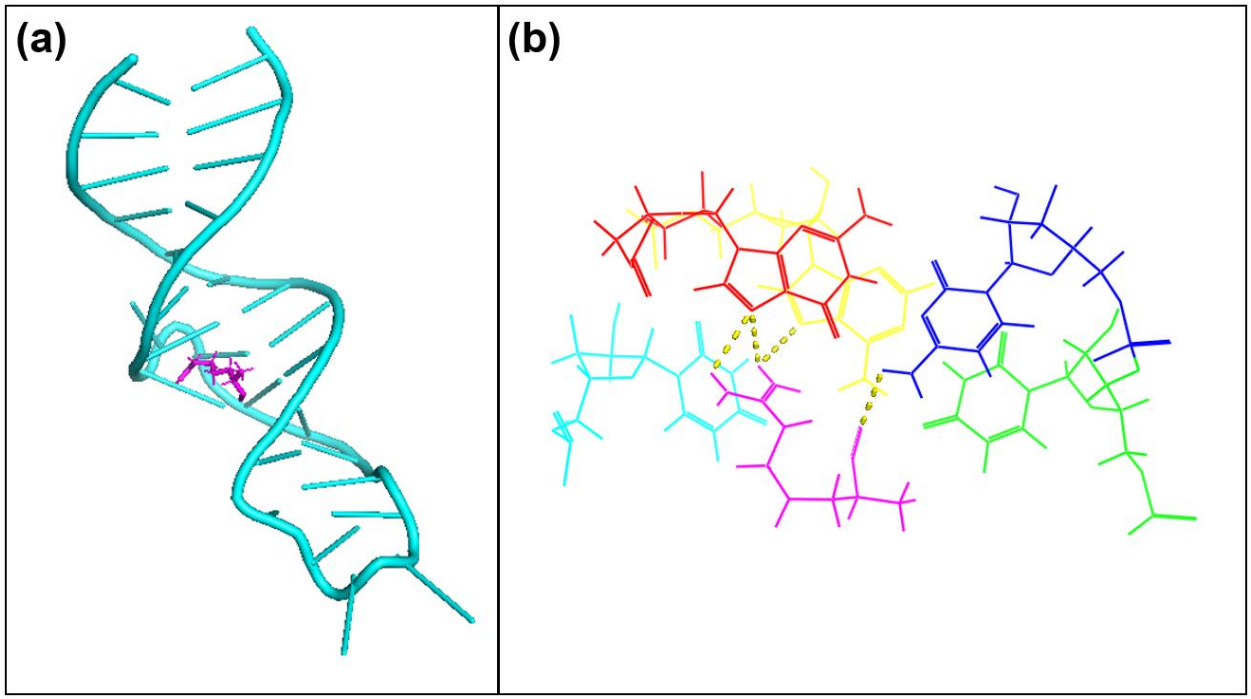

Figure 1.9 (a) Zoomed out view of Argininamide complex (Magenta) with TAR-2 RNA (Cyan) (PDB: 1AJU) [75] **(b)** Zoomed in view of Figure 1.9 (a) Argininamide complex (magenta), U23 (cyan), G26 (red), A27 (yellow), U38 (green), C39 (royal blue). Contacts are shown in yellow.

Shorter, representative sequences TAR-1 and TAR-2 are used because they are more practical and cost-effective for study while still retaining the original function in vitro and in vivo (**Figure 1.7**) [76]. Given the nature of TAR-2's role in the HIV's life cycle, and the previous success of others in developing TAR-1 specific small molecules, targeting TAR-2 would be an excellent approach in creating more effective treatments for HIV-2.

Before we discuss the dynamics experiments which have been conducted to study TAR-2 and A-site sequences, it is imperative to detail the different biophysical tools often used in such experiments. While our work specifically utilizes NMR, it is worthwhile to highlight other tools and explain their limitations which justify why we did not perform our analysis with said tools. It is additionally insightful to detail the different available approaches for making our RNA samples, while we elected to use a chemo-enzymatic approach, all techniques are excellent. Many of the other methods are being used within our lab for other projects currently as equipment and reagents are becoming available.

Chapter 2

2.0 The focus of chapter 2

In this chapter, I outline the biophysical techniques available for studying the dynamics and conformational changes of biomolecules such as RNA, a highly dynamic biomolecule that plays a crucial role in many biological processes, and understanding its motions is a valuable step in pre-clinical drug development. In this chapter, I discussed the capabilities and limitations of these various techniques, and underscore why some were more suitable than others for my research. Finally, I illustrated the

chemoenzymatic pathway for synthesizing an isotopically labeled guanine nucleotide, a process in which I directly contributed.

Table 2.1 A summary table of the advantages and disadvantages of a few common dynamics probing techniques[84-101, 121]

Tool	Advantages	Disadvantages
X-ray crystallography	Can show different conformations of RNA	Not all RNAs can be crystallized; modifications are sometimes needed to enable crystallization
SAXS	Can inform about the compactness of an RNA molecule along with other derived information relating to structure	Cannot detail the exact nucleotides participating in exchange
FRET	analysis of over all structure	Requires fluorescent probe
smFRET	nucleotide specific changes can be shown	Requires fluorescent probe
Cryo-EM	Near-natural state of RNA	Not well-suited for small (50nt or greater) RNA
NMR	Near-natural state of RNA, Studies dynamics on a wide time scale, Can study large and small sizes of RNA	Requires isotopic labels, requires high (>.5mM) concentration of RNA

2.1 Biophysical tools for dynamics analysis

X-ray crystallography has been used to study structures of biomolecules [84-86]. Yet, limitations to this instrumentation persists specific to RNA. RNA is negatively charged due to its phosphate backbone. This negative charge can impede its ability to crystallize and be studied. Another biophysical tool used for dynamics measurements is Förster Resonance Energy Transfer (FRET) [90] and it's more detailed version: single-molecule FRET (smFRET) [91]. Both tools find their power in fluorescence-detected energy transfers. Yet, both smFRET and FRET require a covalent attachment of a fluorophore

molecule. It has been proven that the attachment of fluorophores can impact the dynamics of RNA [92]. This would prevent the observation of the RNA in its least altered, natural state. A fourth popular tool used for studying RNA dynamics is small-angle x-ray scattering. This tool allows scientists to determine the radius of gyration, the maximum particle dimension, and if the RNA is rigid or flexible. However, SAXS is limited in that it cannot provide nucleotide specific information [93]. A fifth exciting instrumental tool for studying dynamics is cryogenic electron microscopy (Cryo-EM). Cryo-EM is a wonderful technique for large molecules; the drawback is that cryo-EM is not well-suited for small (<50 kDa) or highly dynamic RNA [94].

2.2 Nuclear Magnetic Resonance for RNA dynamics analysis

A particularly useful tool used for studying RNA dynamics is NMR [95-101]. NMR leverages the magnetic properties possessed by atomic nuclei and applies radiofrequency pulses to probe the underlying structures. By manipulating the radiofrequency pulses, the user can execute various experiments to study changes in motion to biomolecules over a wide range of time scales. Additionally, through the means of pulse manipulation (pulse programs) it is possible to elucidate structures. Furthermore, NMR allows for the use of water-based buffers with minimal salt additives to study the RNA in its near-natural state. NMR allows scientists to study atom-specific dynamics and accomplishes this in real-time across a wide-range of time scales (**Figure 2.1**). NMR has been used to study large (>90nt) and small (<30nt) RNAs[102].

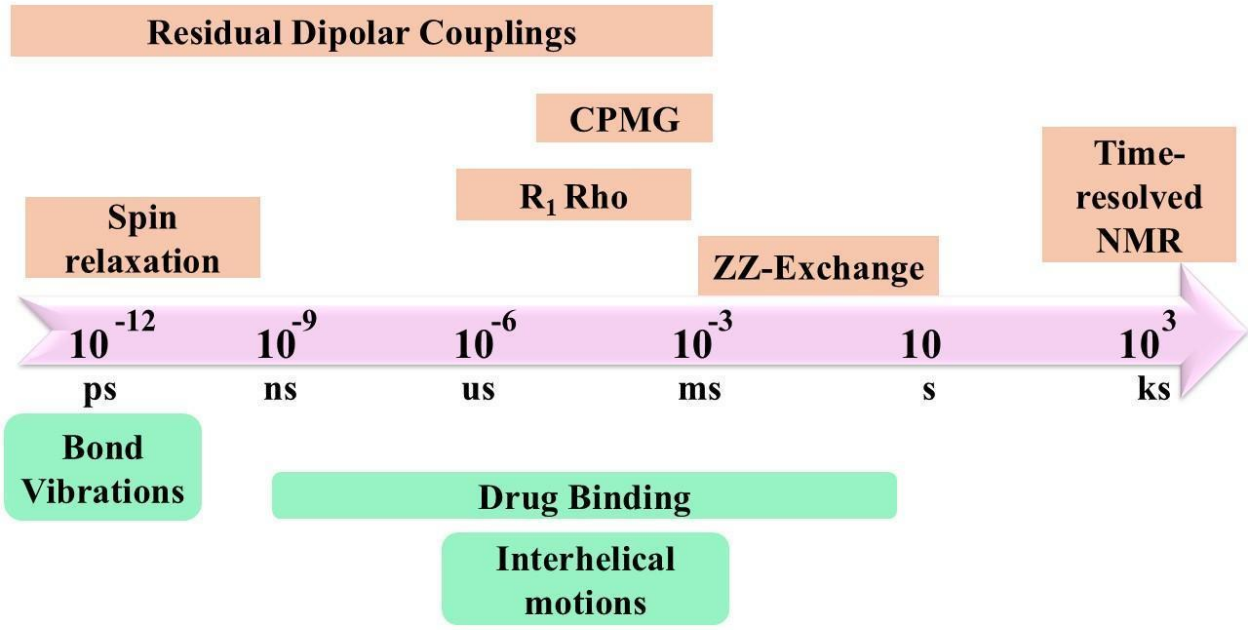

Figure 2.1 Various biological events that can be seen on the timescales of NMR experiments [103]

NMR is a viable choice for studying RNA dynamics. NMR makes possible the goal of understanding RNA better for the sake of future development of drugs tailored to RNA structures. To execute this goal of research, two objectives must be accomplished: (1) the selection of a method by which the RNA is produced, and (2) the incorporation of the required isotopic labels for NMR analysis into the RNA. The remainder of this chapter is dedicated to highlighting the many approaches used in achieving those two objectives, with a further delineation of what approaches were used within this thesis.

2.3 *In vitro* transcription

While there are many methods for producing RNA, *in vitro* transcription remains a classic, this may be due to its ability to make RNAs of small or large (up to 10kB) lengths. *In vitro* transcription mimics the process of what takes place in the cell but does so within a test tube. A DNA template, a DNA promoter sequence, nucleotide triphosphates, thermostable inorganic pyrophosphatase and buffers are combined

with a catalyzing enzyme (*e.g.*: RNA T7 Polymerase). In this reaction, the catalyzing enzyme will bind to the promoter sequence to transcribe the DNA sequence into RNA. The pH and temperature at which this reaction takes place is designed to mimic in-cell activity; thus, pH is approximately 7.5 and the temperature is 37°C. The nucleotide triphosphates have potential to be isotopically labeled; the incorporation of isotopic labels from this technique could result in uniform labeling or nucleotide specific labeling. The RNA that is made from this must be further purified after removing any remaining DNA, unused nucleotide triphosphates and proteins[104].

2.4 Enzymatic ligation of RNA fragments

A method by which RNA is made is through enzymatic ligation of fragmented RNA. In this technique, several pre-made RNA strands are joined together using enzymes such as RNA ligase, to create one longer strand of RNA. They are joined by making a phosphodiester bond between the 3' hydroxyl group of one RNA fragment and the 5'-α phosphate of another fragment of RNA. This reaction requires optimal pH (7.5) and temperature (37°C) to carry forth the reaction. The RNA fragments may have pre-existing isotopic labels. This is an ideal approach for introducing specific isotopic or structural modifications for very large RNA of lengths that solid-phase chemical RNA synthesis cannot accommodate[106-107].

2.5 *In Vivo* Labeling Using Bacterial Systems (Biomass labeling)

Another method used to make RNA with isotopic labels is by *in vivo* isotopic labeling. This technique produces isotopically labeled RNA through growing bacterial systems, in culture media containing stable isotope-labeled nutrients for the bacteria. Examples of these nutrients would be: ^{13}C-glucose, ^{15}N-ammonium salts, or deuterated water. The bacteria systems will use these nutrients and the isotopic labels are incorporated into the RNA which the bacteria make. However, this results in RNA transcripts that are uniformly labeled. The RNA from bacteria can be extracted and then purified. This approach is especially useful for producing large quantities of uniformly labeled RNA [87,108-110].

2.6 Segmental Labeling (SegModTeX)

A recently developed method from the D'Souza lab for labeling RNA is SegModTeX (Segmental Modification and Template-directed Extension). SegModTeX uses a mutant DNA polymerase that can add nucleotides to RNA primers, in efforts to extend the primers. These nucleotides can be isotopically labeled. This small RNA primer is annealed to a complement DNA template. It is through this that the fully desired RNA sequence is formed. Due to this experimental design, differently labeled nucleotides can be used through multiple successions of RNA extensions. This enables the introduction of different labeling patterns throughout a single final RNA molecule. RNA will be purified after completion of elongation [111].

While many options for making isotopically RNA are available, many do have cost, reagent or labelling pattern limitations. To circumvent these limitations, the Dayie lab has fine-tuned a method, chemo-enzymatic synthesis, by which we can couple any isotopically labeled nucleobase to an isotopically labeled ribose to form a nucleotide triphosphate. This nucleotide triphosphate with its site-specific labeling can further be incorporated into RNA.

2.7 Chemo-enzymatic synthesis

In the chemo-enzymatic synthesis approach, a nucleobase may be isotopically labeled through traditional synthesis. This nucleobase can then be coupled to a ribose to form NTPs. We have found this approach to permit control over the labeling patterns, but also to be cost-effective. An example of chemo-enzymatic synthesis can be seen through [^{13}C-8]-Adenine triphosphate synthesis, and the synthesis of another purine is discussed in the subsequent chapter[117-118]. There are many eligible isotopic atoms one may use for labeling. These atoms are discussed in greater detail in the subsequent paragraphs[112-116].

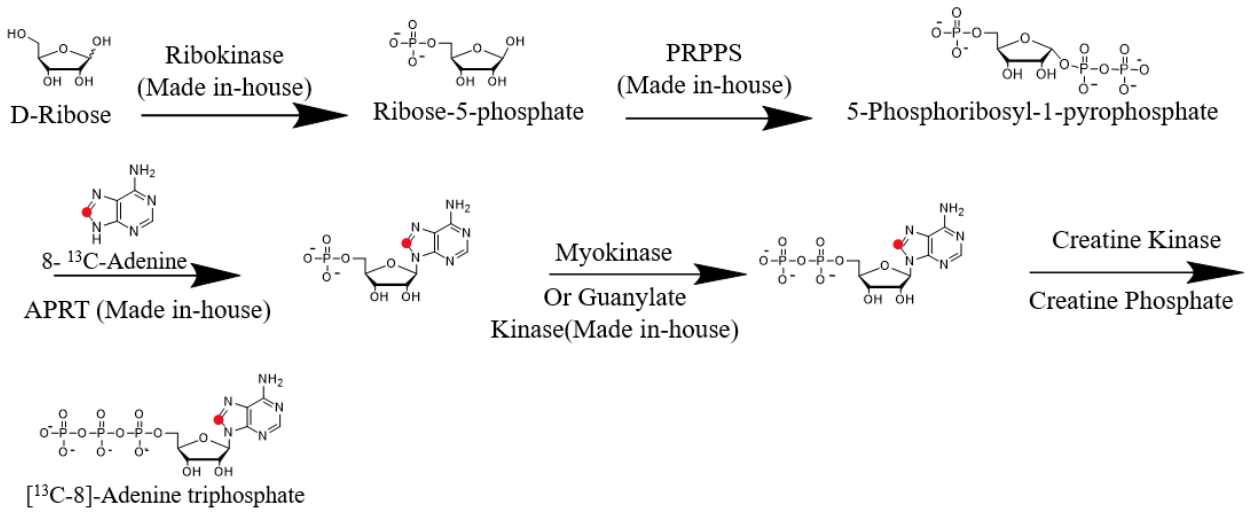

Scheme 2.1 The chemo-enzymatic synthesis pathway to make ATP-[^{13}C-8]; red = ^{13}C. [115-116]

2.8 isotope labels for NMR spectroscopy

Isotopes are the same elements within the periodic table, but they have different masses due to variations in the number of neutrons present in the element's atomic nucleus. Scientists have found many uses for isotopic labels. NMR that focuses on RNA has made extensive use of isotopic labels. RNA's can vary in size, and as they increase in nucleotide length, they produce far more peaks and broad peaks due to their size. This leads to peak overlaps (**Figure 2.2**). However, the replacement of atoms with their isotopic labels can simplify the NMR spectra as they will function as a flashlight and be the only atoms that appear on the resulting spectra. These isotopic labels can be made with different labeling patterns (**Figure 2.3**). The deuterium, proton, 13-carbon, and 15-nitrogen, atoms are often utilized to facilitate RNA studies via NMR. ^{1}H and ^{2}H are two isotopes of the hydrogen atom. ^{1}H is sensitive to the NMR and has a high natural abundance of ~100% (**Table 2.2**). Its sensitivity to the NMR is often capitalized upon, by using ^{1}H in multi-dimensional NMR experiments. In contrast, the heavier ^{2}H is not as sensitive to the NMR and requires a probe to detect the ^{2}H specifically [119-120]. A ^{13}C isotope is used heavily in RNA studies performed on NMR. Specific labeling patterns with the ^{13}C isotope would enable the differentiation of signals specific to purines or pyrimidines[119-120]. Nitrogen atoms are present in all the nucleotides which make up RNA. Certain nitrogen atoms, such as the N-7 position on Guanine, are

notably involved in various biological and drug binding events. This makes them an excellent option for replacing the ^{14}N naturally present isotope with the ^{15}N NMR-active isotopic labels [119-120].

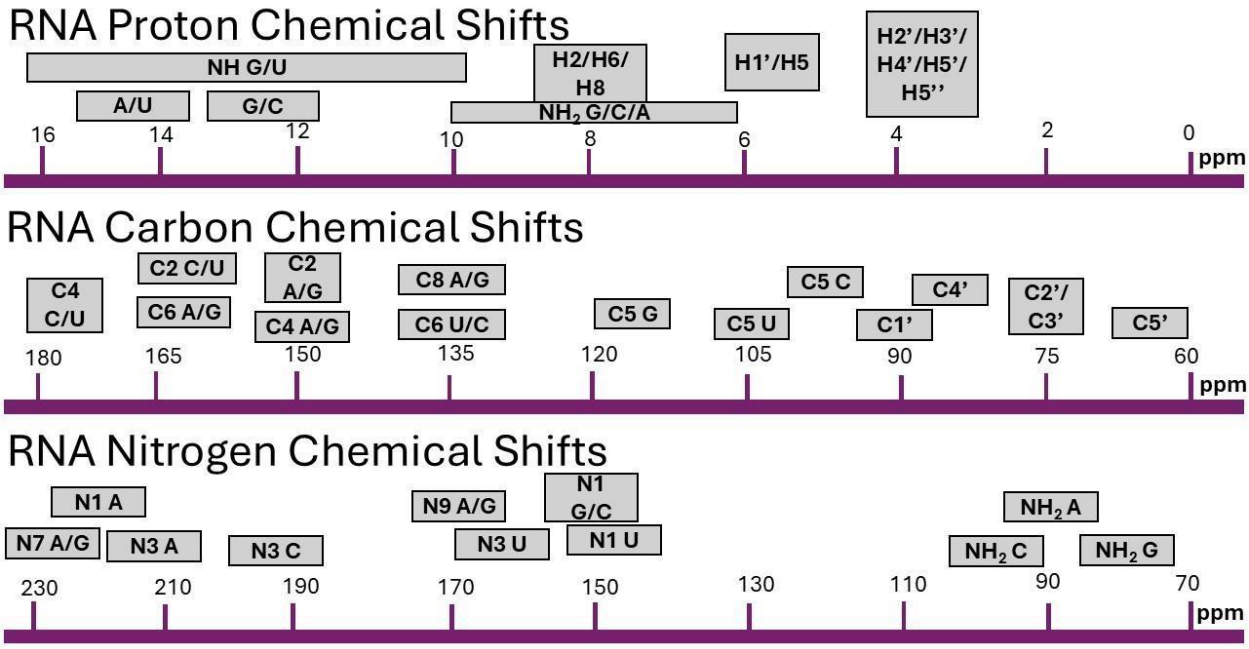

Figure 2.2 The chemical shift values of Carbons, Protons and Nitrogens from RNA nucleobases and riboses[124-123]

Table 2.2 The natural abundance and gyromagnetic ratio values of ^{1}H, ^{2}H, ^{13}C, ^{31}P, ^{15}N and ^{19}F isotopes (**Refence needed**)

Isotope	Natural Abundance (%)	Gyromagnetic Ratio (γ) ($rad \cdot s^{-1} \cdot T^{-1}$)
^{1}H	99.99%	267.5×10^{6}
^{2}H	0.01%	41.0×10^{6}
^{13}C	1.07%	67.2×10^{6}
^{15}N	0.37%	-27.1×10^{6}
^{31}P	100.00%	108.2×10^{6}
^{19}F	100.00%	251.6×10^{6}

N= ^{15}N isotopic label

● = ^{13}C isotopic label

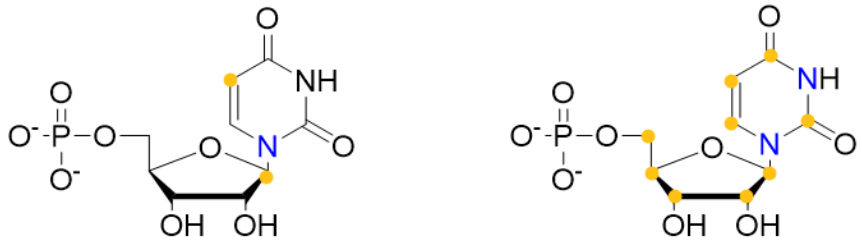

Figure 2.3 Examples of a site-specifically labeled nucleotide (left) and a uniformly nitrogen and carbon labeled nucleotide right).

Chapter 3

3.0 The focus of chapter 3

In this chapter, I focus on understanding the dynamics of RNA NMR spectroscopy. I highlight what is known about RNA's base pairings, imino protons, and physical principles which enable the measurement of flexibility and motion. I explain how relaxation experiments such as R_1, R_2, hNOE, and CPMG provide insight into molecular dynamics, and how magnetization transfer is effected by INEPT (Insensitive Nuclei Enhanced by Polarization Transfer). In short, this chapter aims to bridge the structural picture of RNA with the dynamics revealed by NMR relaxation experiments.

3.1 RNA is a biomolecule in motion

RNA is not a static macromolecule; it can move and take on different conformations to participate in critical functions such as, catalysis, folding, binding and molecular recognition [83, 168-169,91]. NMR relaxation measurements report on the internal and overall motions of the RNA [91, 170-171]. Experiments such as longitudinal (R_1) and transverse (R_2) relaxation, the heteronuclear NOE (hNOE), and the Carr-Purcell-Meiboom-Gill (CPMG) based R_2 report on motions over various timescales, spanning ps- ms [172-175,134] . By combining these measurements, a dynamic picture of the RNA can be formed.

3.2 RNA has many structural components observable through NMR

RNA molecules have secondary and tertiary structures that are stabilized by many interactions including canonical and noncanonical base pairings [176-177]. The helical regions of RNA form through Watson-Crick base pairs or through non-Watson-Crick base pairs.

The helical regions create stable structures, while bulges, internal loops, and pseudoknots can be flexible. Within all of these of these regions and base-pairings, are uracils and guanines, excellent for

NMR observation thanks to their imino protons (**Figure 3.1**). They are visible in the 10-15ppm region of the NMR and thus useful in probing hydrogen bonding and base-pair stability [110].

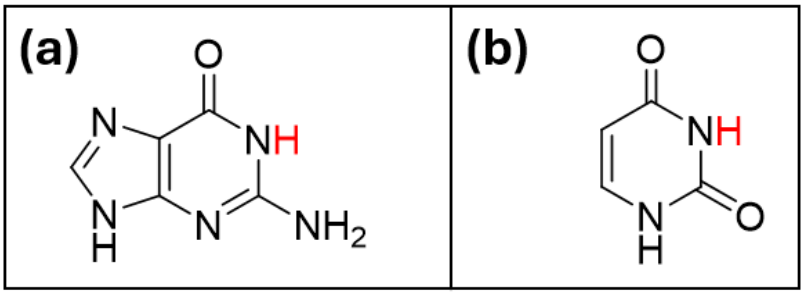

Figure 3.1 The imino protons are depicted in red color on the **(a)** guanine and **(b)** uracil nucleobases.

Due to imino protons participating in the hydrogen bonds that constitute RNA helices, their NMR signals can be seen only when protected from solvent exchange. This provides a means to directly probe structural integrity and base-pair lifetimes.

The monitoring of RNA motions offers a window into conformational dynamics, which is fundamental to RNA's activity and functions. NMR relaxation experiments, such as R_1, R_2, hNOE, and CPMG dispersion, detect the motion of RNA in efforts to characterize timescales of flexibility and exchange [172-175,134].

3.3 Efficient magnetization transfer is key in visualizing relaxation experiments

NMR relaxation suffers from a key limitation: most nuclei, such as ^{13}C and ^{15}N, possess low sensitivity due to their small gyromagnetic ratios (**Table 2.1**). To directly detect these signals in the NMR is a challenge. However, in 1979, efficient magnetization transfer from the abundant and highly sensitive ^{1}H spins became the solution [178]. The solution is known as the INEPT utilizes scalar (J) coupling between heteronuclei and protons to transfer magnetization. The transfer of magnetization improves the heteronuclear signal significantly. As a result, INEPT is often incorporated into relaxation NMR pulse programs.

3.4 Definition of Relaxation in NMR

When the RNA sample is placed in a magnetic field B_0, the spins will align to produce a net magnetization M_0 along the Z-axis. A radiofrequency pulse tips this magnetization away from equilibrium, and relaxation processes will return it to equilibrium[179-180]. Equation 3.1 describes this for inversion recovery.

Equation (3.1a)

$$M_z(t) = M_0(1 - e^{-t/T_1})$$

T_1 (longitudinal) relaxation describes the recovery of magnetization along the Z-axis through energy exchange with the surrounding lattice [179-180] .

This description is the simplified 1D ^{1}H T_1 inversion recovery experiment. To obtain an R_1 relaxation rate for ^{13}C or ^{15}N, more complex NMR pulse programs are used that include INEPT modules to transfer magnetization from protons to the carbons, pulses to eliminate any initial insensitive (^{13}C) magnetization or transverse magnetization, and phase sign alternating to allow for a single exponential decay[87-91] which can be fit to this equation (3.1b)

Equation (3.1b)

$$y(t) = y_0{}^{-R_1 t}$$

Meanwhile T_2 (transverse) relaxation describes the loss of phase coherence among the spins in the XY-plane [181-182]. The two have inverse relationships with their rates.

3.5 Mechanisms of Relaxation

Two major sources of relaxation in RNA are dipole-dipole coupling and chemical-shielding anisotropy (CSA). Dipole-dipole relaxation happens when nearby atomic nuclei affect each other's magnetic fields as molecules tumble in solution, causing changes that let the spins transition into different energy levels [183].

CSA relaxation happens due to the electrons around a nucleus shielding it unevenly in different orientations. As the RNA moves, this uneven shielding changes over time, and that creates fluctuating magnetic fields [184]. Both R_1 and R_2 (the rates for T_1 and T_2 respectively) can be expressed via the spectral density function J(ω). Spectral density function depicts how efficiently motions at frequency ω modulate magnetic interactions; this is seen in equations 3.2 and 3.3.

Equation (3.2)

$$R_1 = 3(d^2 + c^2)J(\omega_S) + d^2[J(\omega_I - \omega_S) + 6J(\omega_I + \omega_S)]$$

Equation (3.3)

$$R_2 = \frac{1}{2}(d^2 + c^2)[4J(0) + 3J(\omega_S)] + \frac{d^2}{2}[J(\omega_I - \omega_S) + 6J(\omega_I + \omega_S) + 6J(\omega_I)] + R_{ex}$$

$d = \left(\frac{\mu_0 h \gamma_S \gamma_I}{16\,\pi^2 r_{SI}^3}\right)$ and $c = \omega_S \Delta\sigma_S/3$ (**Definition in 3.3**)

In equations 3.2 and 3.3 γ depicts the gyromagnetic ratios and ω depicts the Larmor frequencies. These equations-based relationships highlight how relaxation depends on molecular motion through J(ω). For isotropic tumbling, J(ω) is given by:

Equation (3.4)

$$J(\omega) = \frac{\tau_C}{1+(\omega\tau_C)^2})$$

where τ_C is the rotational correlation time. The relationship between R_1, R_2, and J(ω) allows quantitively modelling flexibility.

3.6 Importance of dynamics experiments

By comparing R_1 and R_2 and hNOE measurements the parts of a molecule that are dynamic or static are revealed. Relaxation experiments can provide insight into motions that are used in RNA activity and

function. Yet, these experiments require the ability to observe weak heteronuclear signals with sufficient sensitivity. This is challenge is overcome by the INEPT sequence.

3.7 Purpose and Importance of INEPT

The INEPT pulse sequence allows for the detection of nuclei with low sensitivity, such as ^{13}C and ^{15}N. INEPT transfers polarization from ^{1}H to the heteronucleus via scalar coupling [178]. This process increases signal intensity of the ^{13}C or ^{15}N. INEPT relies on the J-coupling Hamiltonian ($2\pi J\, I \cdot S$). Delays within the pulse program allows proton magnetization to evolve into an antiphase state, which then is converted into the heteronuclear magnetization.

3.8 Product-Operator Description

The evolution of the density matrix seen in INEPT and its accompanying pulse program is as follows:

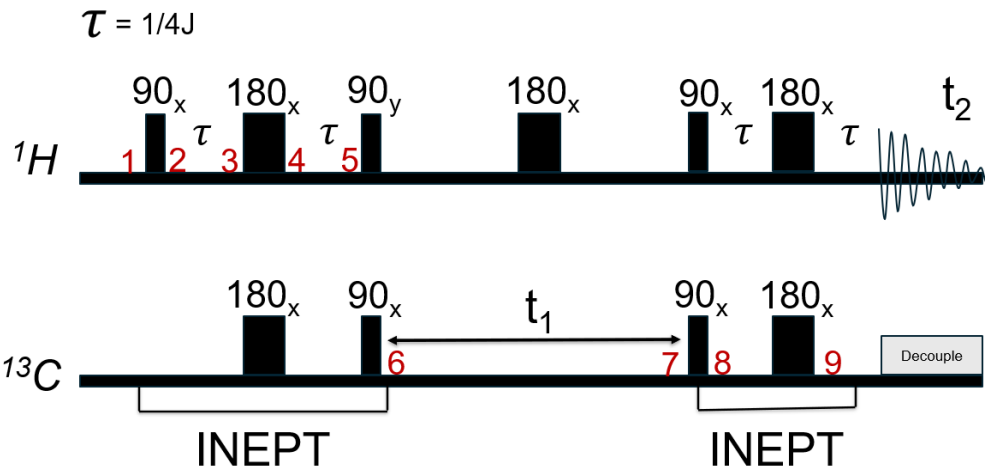

$(\varphi = \pi J\tau)$

$$1 H_z \overset{90_H^x}{\rightarrow} -H_y$$

$$2 \quad -H_y \overset{J}{\rightarrow} -[H_y cos\,(\varphi) - 2H_x C_z sin\,(\varphi)]$$

$$3 \quad \overset{180_H^x}{\rightarrow} -[-H_y cos\,(\varphi) - 2H_x C_z sin\,(\varphi)]$$

$$\overset{180_C^x}{\rightarrow} -[-H_y cos\,(\varphi) + 2H_x C_z sin\,(\varphi)]$$

$$4 \overset{J}{\rightarrow} cos\,(\varphi)[-H_y cos\,(\varphi) + 2H_x C_z sin\,(\varphi)] - sin\,(\varphi)[2H_z C_z cos\,(\varphi) + H_y sin\,(\varphi)]$$

$$5 = H_y[cos^{\,2}\varphi - sin^{\,2}\varphi] - 2H_z C_z[2sin\ \varphi cos\ \varphi] = H_y cos\,(2\varphi) - 2H_z C_z sin\,(2\varphi)$$

$$= \varphi = \pi/4 - 2H_z C_z$$

$$6 \quad -2H_z C_z \overset{90_C^x}{\rightarrow} -2H_z C_y$$

$$7 \quad -2H_z C_y \overset{\omega_C t_1}{\rightarrow} -2H_z[C_y cos\,(\Omega) + C_x sin\,(\Omega)](\Omega = \omega_C t_1)$$

$$8 \quad \overset{90_C^{-x}}{\rightarrow} -2H_z[C_z cos\,(\Omega) - C_y sin\,(\Omega)] \approx -2H_z C_z cos\,(\Omega)$$

$$9 \quad -2H_z C_z cos\,(\Omega) \overset{reverse\ INEPT}{\rightarrow} H_y cos\,(\Omega)$$

$$H_y cos\,(\Omega) \overset{90_H^{\pm x}}{\rightarrow} H_x cos\,(\Omega)$$

where the trigonometric identities $\cos(2\varphi) = \cos^2\varphi - \sin^2\varphi$ and $\sin(2\varphi) = 2\sin\varphi\cos\varphi$ were used in the last step. The delay τ is set equal to $1/(4J_{HC})$, rendering $\sin(2\varphi) = 1$ when $2\varphi = \pi/2$. As a result, the density matrix before the carbon 90° pulses at the end of the first INEPT period is:

$$\rho = -2H_z C_z$$

After the subsequent two 90° pulses on carbon and the second INEPT refocused delay, this term becomes $+H_x$, which produces a single resonance line for the in-phase $^1H_x \cos(wt)$ signal that can be seen on the NMR when carbons are decoupled during acquisition. This product operator formalism shows the transfer of the proton polarization to the carbon spin and back to the proton spins promotes the ability to detect even nuclei with lower gyromagnetic ratio.

3.9 R_1 (Longitudinal Relaxation) and R_2 (Transverse Relaxation)

The R_1 experiment monitors how starting from protons carbon magnetization is created by INEPT along the z-axis (C_z) and allowed to decay as a function of time. The data is fitted to equation (3.1b) to obtain T_1 and $R_1 = 1/T_1$. R_1 values are sensitive to molecular motions on the picosecond to nanosecond (ps-ns). The R_2 experiment monitors the decay of transverse magnetization in the XY-plane using (Equation 3.3). It includes contributions from chemical exchange. The observed R_2 relationship is seen below as:

Equation (3.5)

$$R_2(\text{observed}) = R_2^{o} + R_{ex}$$

where R_{ex} represents exchange broadening. Larger R_2 highlight regions of rigidity or reduced flexibility superimposed on potential contributions from conformational exchange processes (motions occurring on the micro- to millisecond timescale).. Thus, the R_1 and R_2 experiments are excellent options for detecting fast motions on the ps-ms timescale.

3.10 hNOE (Heteronuclear NOE)

In the hNOE experiment, proton saturation significantly affects the intensity of the heteronuclear peaks through cross-relaxation effects, specifically the dipolar coupling between the saturated protons and the observed carbon nuclei. Rigid regions show lower hNOE values, while flexible regions show larger values. Collectively, R_1 and R_2, hNOE may highlight key areas of flexibility. The equation relating hNOE to relaxation is seen in equation 3.6; with its definitions noted.

Equation (3.6)

$$hNOE == I_{SAT}\,/I_{NO\_SAT} = 1 + \left(\frac{\gamma_I}{\gamma_S}\right)\frac{d^2}{R_1}[6J(\omega_I + \omega_S) - J(\omega_I - \omega_S)]$$

$$d = \left(\frac{\mu_0 h \gamma_S \gamma_I}{16\,\pi^2 r_{SI}^3}\right) \quad \text{(Definition in eq 3.6)}$$

$$J(\omega) = \frac{\boldsymbol{\tau_C}}{\mathbf{1}+(\boldsymbol{\omega\tau_C})^{\mathbf{2}}} \quad \text{(Definition in eq 3.6)}$$

Here the steady state NOE is define as I_{SAT} /I_{NO_SAT} where I_{SAT} and I_{NO_SAT} are signal intensities of the carbon nucleus measured when the proton nucleus is in the saturated and in the equilibrium states, respectively.

3.11 CPMG (Relaxation Dispersion)

The Carr-Purcell-Meiboom-Gill (CPMG) relaxation dispersion experiment provides insight into conformational exchange occurring on µs-ms timescales. It allows for the measurement of the effective transverse relaxation rate $R_{2,\mathrm{eff}}$ as a function of the 180° pulse frequency ν_{CPMG} (equation 3.6).

Equation (3.6)

$$R_{2,\mathrm{eff}}(\nu_{\mathrm{CPMG}}) = R_2^0 + R_{ex}(\nu_{\mathrm{CPMG}})$$

When a nucleus exchanges between two states, A and B, with chemical-shift difference, Δω, with total exchange rate (equation 3.7)

Equation 3.7

$$k_{ex} = k_{AB} + k_{BA}.$$

A common description for fast exchange ($k_{ex} \gg |\Delta\omega|$), is seen in the Carver–Richard's equation:

Equation (3.8)

$$R_{cpmg}(\tau_{cp}) = \frac{1}{2}\left(R_2^A + R_2^B + k_{ex} - \frac{1}{2\tau_{cp}} cosh^{-1}\left[D_+ \cosh(\eta_+) - D_- \cos(\eta_-)\right]\right)$$

$$\eta_\pm = \sqrt{2}\tau_{cp}\left[\pm\psi + (\psi^2 + \xi^2)^{1/2}\right]^{1/2} \quad \text{(Definition in eq. 3.7)}$$

$$D_\pm = \frac{1}{2}\left[\pm 1 + \frac{\psi + 2\Delta\omega^2}{(\psi^2+\xi^2)^{1/2}}\right] \quad \text{(Definition in eq. 3.7)}$$

$$\psi = (R_2^A - R_2^B - p_A k_{ex} + p_B k_{ex})^2 - \Delta\omega^2 + 4p_B p_A\, k_{ex}^2 \quad \text{(Definition in eq. 3.7)}$$

$$\xi = 2\Delta\omega\,(R_2^A - R_2^B - p_A k_{ex} + p_B k_{ex}) \quad \text{(Definition in eq. 3.7)}$$

where $R_2^{A/B}$ is the R_2 rate, and $p_{A/B}$ are the relative populations of the A/B states. In the CPMG experiment conformational exchange of nuclei is represented by a non-flat CPMG curve when plotting $R_{2,eff}$ as a function of the various frequencies used when the 180° pulses are applied (ν_{CPMG}). In the absence of exchange, CPMG curve is flat. If no exchange is taking place $R_{2,\text{eff}} = R_2^0$. Δω scales with magnetic field B_0, thus, it is necessary to conduct CPMG experiments at multiple fields so that k_{ex} and Δω can be determined independently. When doing data analysis, the $R_{2,\text{eff}}$ values are fitted to Carver-Richard's [156] or Bloch- McConnell equations [155]. The CPMG experiment can complement R_1, R_2, and hNOE by broadening the range of NMR relaxation data into the region of kinetics.

3.12 Summary of chapter 3

NMR relaxation measurements reveal how RNA moves. NMR experiments can transform static structural data into a dynamic picture of RNA. R_1 and R_2 describes how magnetization returns to equilibrium, the hNOE shows high-frequency motions, and CPMG can detect conformational exchanges. Present in all these experiments is the INEPT sequence. INEPT transfers magnetization from protons to heteronuclei with smaller gyromagnetic ratios. These experiments are used in the subsequent chapters

along with isotopically labeled RNA; for it is isotopic labels which facilitate the use of relaxation experiments.

Chapter 4

4.0 The focus of chapter 4

In this chapter I detail the biological importance of a specific nitrogen position in the nucleobase of guanine. I share the synthetic route that was used to synthesize this nucleobase with a nitrogen-15 label on the N-7 position of guanine. I also provide NMR spectra which validates the success of the synthesis. This nucleobase was used in a paper by a previous lab member, Dr. Mary Taiwo. As a result, the HSQC spectra appear in her thesis as well [7].

4.1 Guanine's N-7 position has biological and NMR significance

The guanine N7 position is a hub for many biological events: it is a site for molecular recognition, metal ion coordination, and drug binding [21,185, 186-187]. This position is situated on the imidazole ring. The N7 position has a lone pair and thus can act as a hydrogen bond acceptor. This allows guanine to involve itself in tertiary and catalytic interactions.

N7 has a role in RNA capping. In the eukaryotic messenger RNA (mRNA), guanine is methylated at N7 to form 7-methylguanosine (m^7G). This produces the 5′ cap structure [185]. The methylation leaves a positive charge on purine ring, which may increase its π-stacking with proteins and promotes binding to the cap-binding complex. The methylation also protects RNA transcripts from 5′ exonuclease degradation.

Beyond the scope of capping, N7 is important due to its accessibility and coordinating potential. The N7 atom can coordinates Mg^{2+} or other divalent ions, and this stabilizes tertiary structures [186-187]. The N7 can also participate in noncanonical hydrogen bonds, like in Hoogsteen [188-190] and G-quadruplex motifs [191-193].

The chemical environment of N7 additionally makes it a target for drugs and electrophilic agents. Drugs that bind to N7 can alter RNA conformation, as seen in paromomycin [21]. In the NMR, guanine N7 can be used to probe for structure[105] and dynamics [106]. Site-specific ^{15}N labeling enables measurement of relaxation parameters such as R_1, R_2, and heteronuclear NOE. This can reveal motions across many timescales. CPMG relaxation dispersion studies on N7-labeled RNA may show conformational exchange using the Bloch–McConnell and Carver–Richards equations.

Given the importance of this site, I synthesized a guanine nucleobase isotopically enriched with ^{15}N specifically at the N7 position. This labeled nucleobase served as the control for subsequent NMR investigations with other peers in the lab. What follows is the synthetic protocol used for the preparation of the $^{15}N7$ - guanine that was adapted from other work [106,194].

4.2 The synthetic route used to make $^{15}N7$ - guanine

[5-^{15}N]-2,4,5-triaminopyrimidin-4(*3H*)-hydroxyl sulfate. 2,6-diaminopyrimidin-4(3H)-one, commercially purchased, (1.00 g, 7.95 mmol) and sodium nitrite (0.58 g, 8.41 mmol) were dissolved in 13 mL of 3M sodium hydroxide. The homogenous solution was added dropwise to 16.5 mL of glacial acetic acid with stirring and cooling on ice. The pink suspension which formed was centrifuged at 7500 rpm for 5 min and resuspended in water. The supernatant was decanted and the residue was resuspended in 24.5 mL of hot water to yield a pink suspension. The reaction was kept at 100 ^{o}C and several portions of sodium dithionite were added to the suspension, with stirring till the suspension eventually turned pale-yellow. The mixture was cooled in an ice bath for 30 min and 1.8 mL of concentrated sulfuric acid was added gradually to the suspension with stirring until the solution turned bright yellow in color. Subsequently, the suspension was heated at 85 ^{o}C for 4 h and allowed to cool to room temperature. The cooled suspension was centrifuged at 7500 rpm for 5 min and the resulting residue was resuspended in ethanol and centrifuged at 7500 rpm for 5 min. The suspension was filtered and washed with excess ethanol to yield 1.90 g of a compound (100%) as a pale-yellow solid.

[7-^{15}N]-Guanine. [5-^{15}N]-2,4,5-triaminopyrimidin-4(*3H*)-hydroxyl sulfate (1.90 g, 7.95 mmol) was dissolved in 3.6 mL formamide and 0.54 mL of formic acid and then refluxed at 110 °C and 180 °C for 1hr and subsequently for 2hr, under argon. A yellow precipitate was formed after cooling on ice for 30 minutes. The precipitate was filtered, rinsed with water and ethanol, and dried. The yellow solid was dissolved in 7.2 mL of 10% NaOH and reacidified dropwise with formic acid until pH 4. The off-white precipitate was filtered and washed severally with water to yield 0.69 g of pure compound guanine (58%) as an off-white solid.

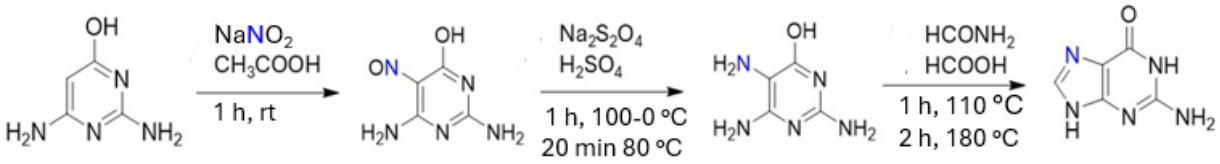

Scheme 4.1 This schematic shows the pathway to synthesizing isotopically labeled guanine on the N-7 position. The synthesis begins with a nitrosylation followed by a reduction, then acid treatment step. This renders a yield of 100%. However, this synthesis combines the nitrosylation step into the reduction step. Thus, NMR is available exclusively for the final two steps. Finally, the ring is closed through a n-formylation with a final yield of 58%. The alcohol tautomerizes and this yields the final product of the ^{15}N7-Guanine.

4.3 NMR of the synthesis of *[7-^{15}N]-Guanine*

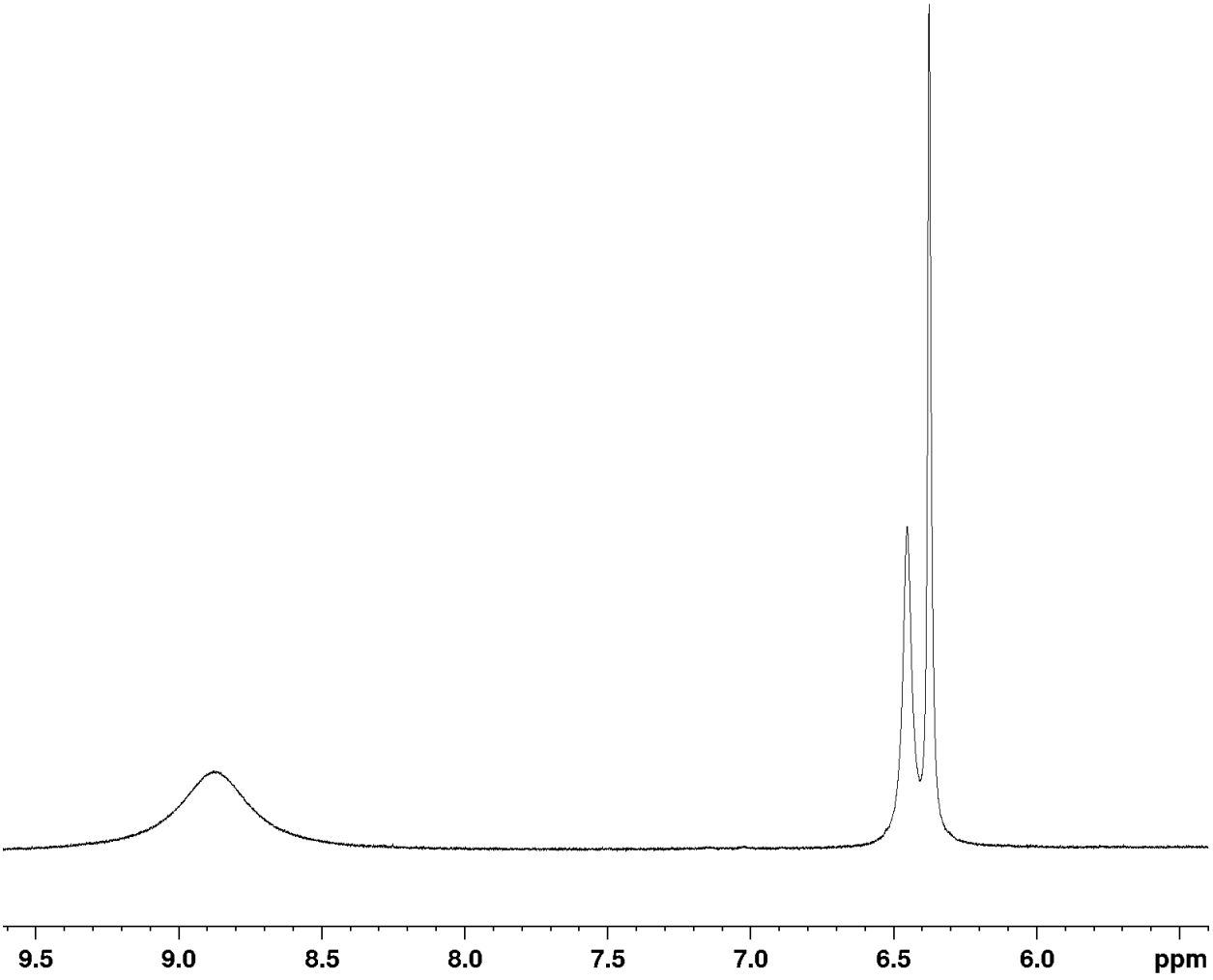

^{1}H NMR (600 MHz, DMSO-d_6): δ = 10.46 (b, 1H, OH), 8.94 (b, 1H, NH_2) 6.35 (s, 4H, $2NH_2$), 6.20 (s, 2H, NH_2) ppm. ***[5-^{15}N]-2,4,5-triaminopyrimidin-4(3H)-hydroxyl sulfate.*** The two peaks come from the two amino groups attached directly to the ring, and each one gives a broad looking singlet because their protons are exchanging rapidly in solution. They have different chemical shifts because the two ring positions, C4 and C6's amino groups are in different chemical environments. These peaks do not come from the amino group that contains the ^{15}N label, that labeled group appears separately at 8.94 ppm

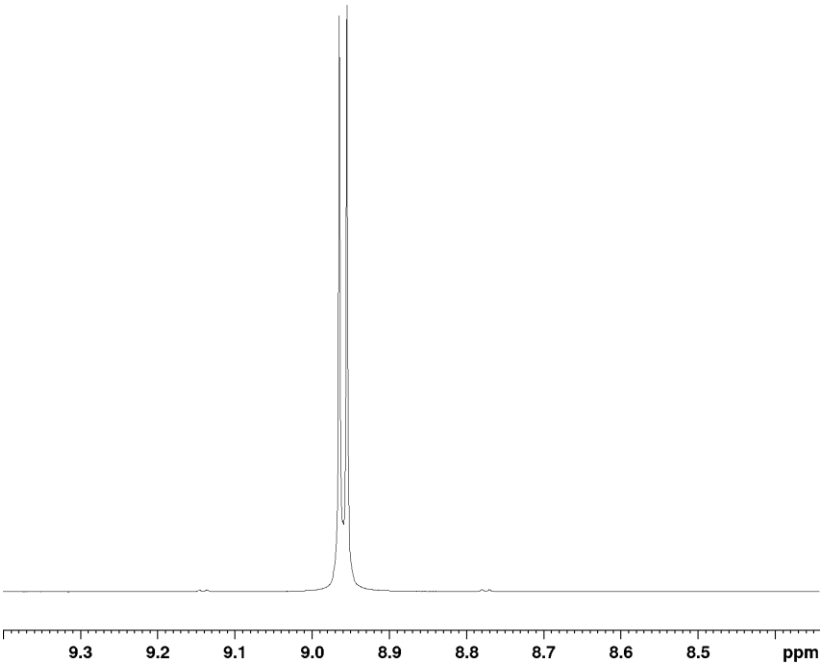

^{1}H NMR (600 MHz, DMSO-d_6, DCl): $\boldsymbol{\delta}$ = 8.96 (d, $^{2}J_{HN}$ = 5.92 Hz) ppm *[7-^{15}N]-Guanine. The peaks corr*espond to the H8 proto. The doublet comes from scalar coupling between H8 and the ^{15}N label at N7.

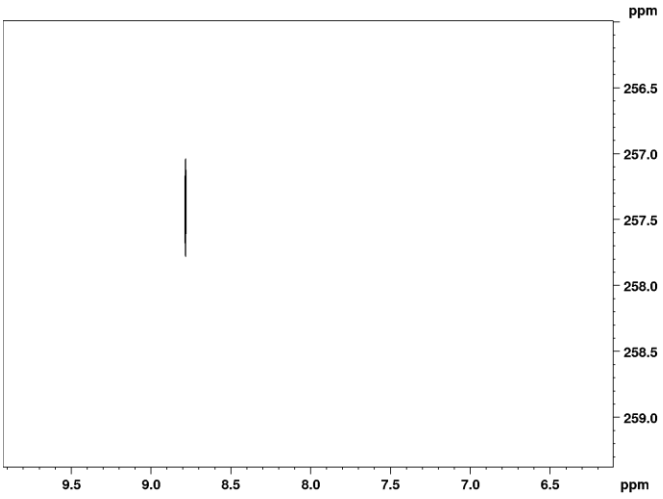

^{1}H-^{15}N NMR long range HSQC 10 mM NaOD in D_2O [7-^{15}N]-Guanine

4.4 Summary of chapter 4

In this chapter I detailed the synthesis and logic behind an isotopically labeled guanine at the N7 position. By emphasizing the biological and structural importance of this site, the work established shows how isotopic labeling can enhance the precision of NMR-based characterization of RNA. While this chapter focused on synthesizing a single label, my next chapter extends this concept by applying a different isotopic label to investigate biologically relevant processes that occur on NMR-detectable timescales

Chapter 5

5.0 The focus of chapter 5

In this chapter, I document the thermal stability and dynamics differences between prokaryotic and the eukaryotic A-site rRNA by NMR. I also tested thermal stability using UV spectroscopy. It was hypothesized, that thermal stability would be alike due to secondary and tertiary sequence similarities, but differences in dynamics would be noted, and this logic was rooted in prior publications [117,121, 167.] We determined the rates of exchange specific to adenines 1492/1493 and compared them between both rRNAs. We found subtle differences in the rates of exchange of the residues in question, along with minor differences in thermal stability. The results from this chapter could be useful in understanding the thermal stability and dynamics differences between the pathogenic and host rRNA in complex with aminoglycosides and may help in the development of more specific antibacterial agents. This work was done in efforts to publish a paper in which I and a prior member of the lab, Dr. M. Taiwo would both be first authors. Some of the data in this chapter may appear in her thesis as well. This has been approved by our P.I., T. K. Dayie.

5.1 The sequence location of Adenines 1492 and 1493

Aminoglycosides are a class of antimicrobials that treat Gram-negative bacteria [125]. Certain aminoglycosides disrupt the event of translation by binding to specific nucleotides in the rRNA of bacteria

[126]. Translation, in prokaryotes and eukaryotes involves the appropriate contacts between the anticodon cognate transfer RNA and the codons of the messenger RNA (mRNA) in a region of the ribosome: the aminoacyl site (A-site) [27]. The A-site is in helix 44 of the 16S rRNA (prokaryotes) or 18S rRNA (eukaryotes) [127].

5.2 Sequence and crystallographic differences in the prokaryotic and eukaryotic rRNA

The eukaryotic and prokaryotic sequences have great similarities; 11 of the 15 of the internal loop are conserved [128]. One of these differences can be noted as the nucleotide at 1408 position is a guanine in prokaryotes and an adenine in eukaryotes [128,129]. As we mentioned earlier, aminoglycosides are intended to bind to bacterial sequences, yet off-target binding has been reported in eukaryotic sequences [31-34]. Given the accelerating rate of antibiotic resistance there is a need for the design of new or functionally improved compounds that can bind the 16S rRNA with greater specificity. As underscored in chapter 1, rRNA has a major role in protein synthesis. This role has been well-leveraged by aminoglycosides [130,131]. Therein lies the importance in understanding the differences between the structures and conformation of the prokaryotic and eukaryotic A-site RNA; this may promote the design or improvement of antimicrobials that bind specifically to the bacterial RNA.

Previous crystallographic research from the Westhoff group finds that despite the sequence conservations between the prokaryotic and eukaryotic A-site rRNAs, there are conformational differences between the two [133] (**Figure 5.1**).

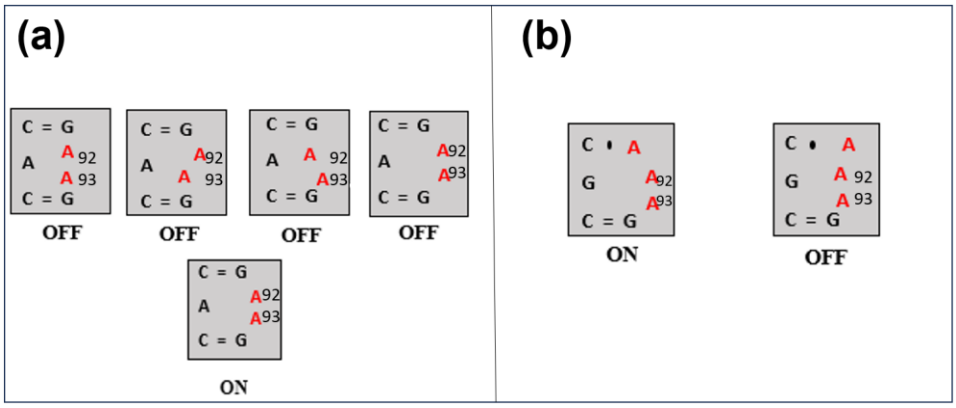

Figure 5.1. An adaptation of the crystal states as pictured in the crystal studies cited [133]. **(a)** prokaryotic bulge containing adenines 1492 and 1493. **(b)** Eukaryotic bulge containing adenines 1492 and 1493.

Both rRNAs have an asymmetric bulge positioned between an upper and lower helical stem [132,133]. Westhoff's group used fragments of these two rRNA sequences and found that the bulge region can adopt an “off” and “on” conformation [132, 133]. The defining characteristic of the “on” state is the flipping-out of the Adenines 1492 and 1493. As previously mentioned, these two adenines interact with incoming tRNA [27, 134], for the prokaryotic and eukaryotic sequences. It is this event that enforces the correct pairing between the anticodon of the cognate tRNA with the codons from the mRNA [127]. It is aminoglycosides that will bind in the place of tRNA at the A-site’s A1492/1493 nucleotides and disrupt this organized process to cause miscoding during translation [135].

5.3 NMR is a tool which may provide comparative details about dynamics and thermal stability

While work has been completed to compare the structures and conformation of the prokaryotic and eukaryotic A-site fragment sequences, minimal is known about the differences in the dynamics via NMR. As mentioned in chapters 2 and 3, NMR is a tool that allows for probing structural and conformational states on a wide timescale [136] that X-ray crystallography cannot capture.

5.4 The prokaryotic and eukaryotic A-site rRNA possess different thermal stabilities

The rRNA used in this work are fragments that recapitulate the behavior of their wild types [128]. Both rRNAs comprise a three-nucleotide internal bulge flanked by a lower and upper helix. Both rRNAs have UUCG tetraloops that caps the upper helix. This was added in this study to enhance stability in the structures (**Figure 5.1**). All adenines from both prokaryotic and eukaryotic sequences were isotopically labeled with ^{13}C on the 8 positions of the nucleobase (**Figure 5.2**).

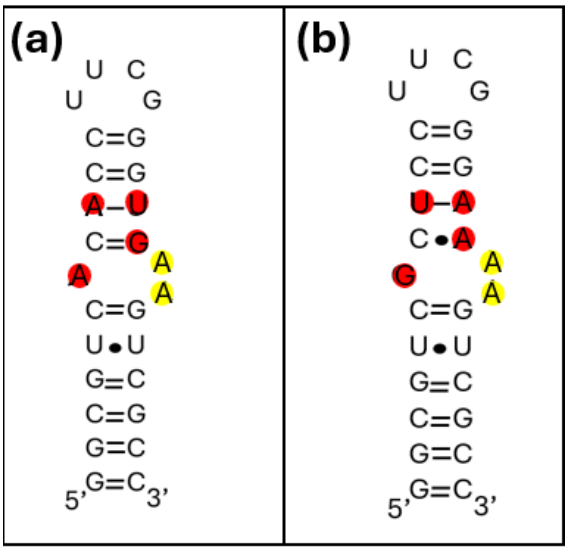

Figure 5.2 Secondary structure of the rRNA constructs **(a)** prokaryotic A-site rRNA **(b)** eukaryotic A-site rRNA. The sequence differences are highlighted in red color, and the adenines of interest are in yellow.

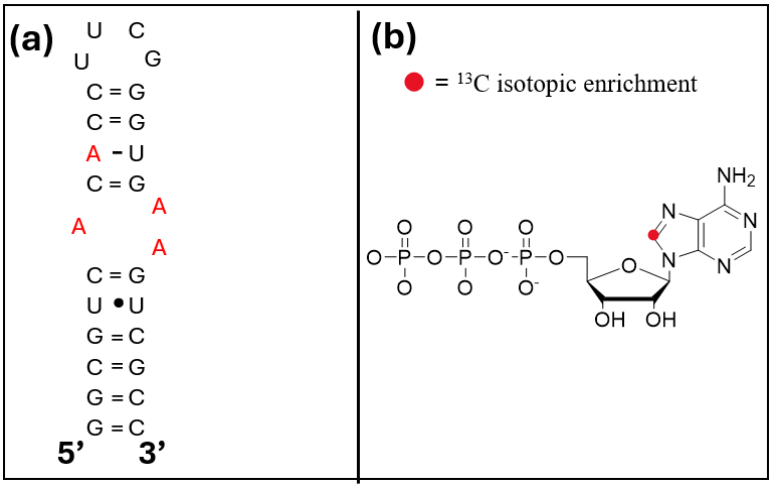

Figure 5.3 (a) Secondary structure of prokaryotic A-site rRNA; The sites of the isotopic label are highlighted in red color. **(b)** The placement of the adenine nucleotide triphosphate which shows the carbon label in red.

5.5 1-dimensional proton NMR of the imino region can be used to test nucleotide specific thermal stability in RNA

There are many regions within a typical 1-D proton NMR that would be specific to a particular type of proton's presence. The imino proton region ranges between 10 and 15 ppm [123-124]. The imino region is helpful in conducting NMR melting experiments. These experiments can study the thermal stability of RNA. Imino protons are involved in hydrogen bonding with base pairs, and their peaks change to depict structural rearrangements. As temperature increases, the hydrogen bonds in base pairs that possess imino protons begin to dissociate. This leads to a broadening and eventual disappearance of imino proton peaks. These changes were monitored for our RNAs to gain insight into sequence stability. A further discussion of the results is seen in the subsequent paragraphs.

5.6 NMR melt analysis reveals similar structural stability of prokaryotic and eukaryotic A-site rRNA

It is desirable to know the stability of the specific nucleotides in these sequences. NMR provides nucleotide-specific information [141]. A typical one-dimensional NMR spectrum of the imino proton chemical shift region (10-15 ppm) shows peaks from the imino protons from guanines and uracils. These protons are visible when either guanines or uracils are hydrogen bonded to an A, G, C or U base. The imino region of a spectrum reflects the secondary structure of an RNA. Additionally, the transition between a folded (bonded) and unfolded (unbonded) state can be monitored by the initial broadening and the final disappearance of imino peaks as a function of increasing temperature due to the exchange of protons with the solvent water.

In this experiment we monitored the melting of the two rRNA constructs as we increased the temperature from 278K to 326K in 10K increments. Previous work from members of the group provided resonance assignments. The disappearance of imino peaks followed in this order: non-canonically bonded nucleotides, the A-U pairs, and the G-C base pairs **(Figure 5.4)**. Interestingly, the G-C base pair near the bulge was the first to break when compared to other G-C pairs located in the upper and lower helices. This may be explained by the likely additional stacking interactions between adjacent base pairs in the helix which are not present in the bulge. In both the prokaryotic and eukaryotic rRNA, the amino peaks of G2, G4, G16 and G25 were visible through 316K; this indicates that those are very stable. Unfortunately, I could not monitor the adenine residues of both the prokaryotic and eukaryotic rRNAs in the bulge as they do not have imino protons. In the prokaryotic and eukaryotic rRNA the guanines and uracils that participated in Watson-Crick bonding were still visible at 316K. For additional confirmation of the similarities in stability, I used Python to calculate area under the curves using an image analyzing code which allowed me to derive the total area under the curves per heat increment of each rRNA. This is seen in the appendix **(Figure 1 and 2 a-f)**. It co-confirms these two sequences are overall similar in their NMR melt profiles.

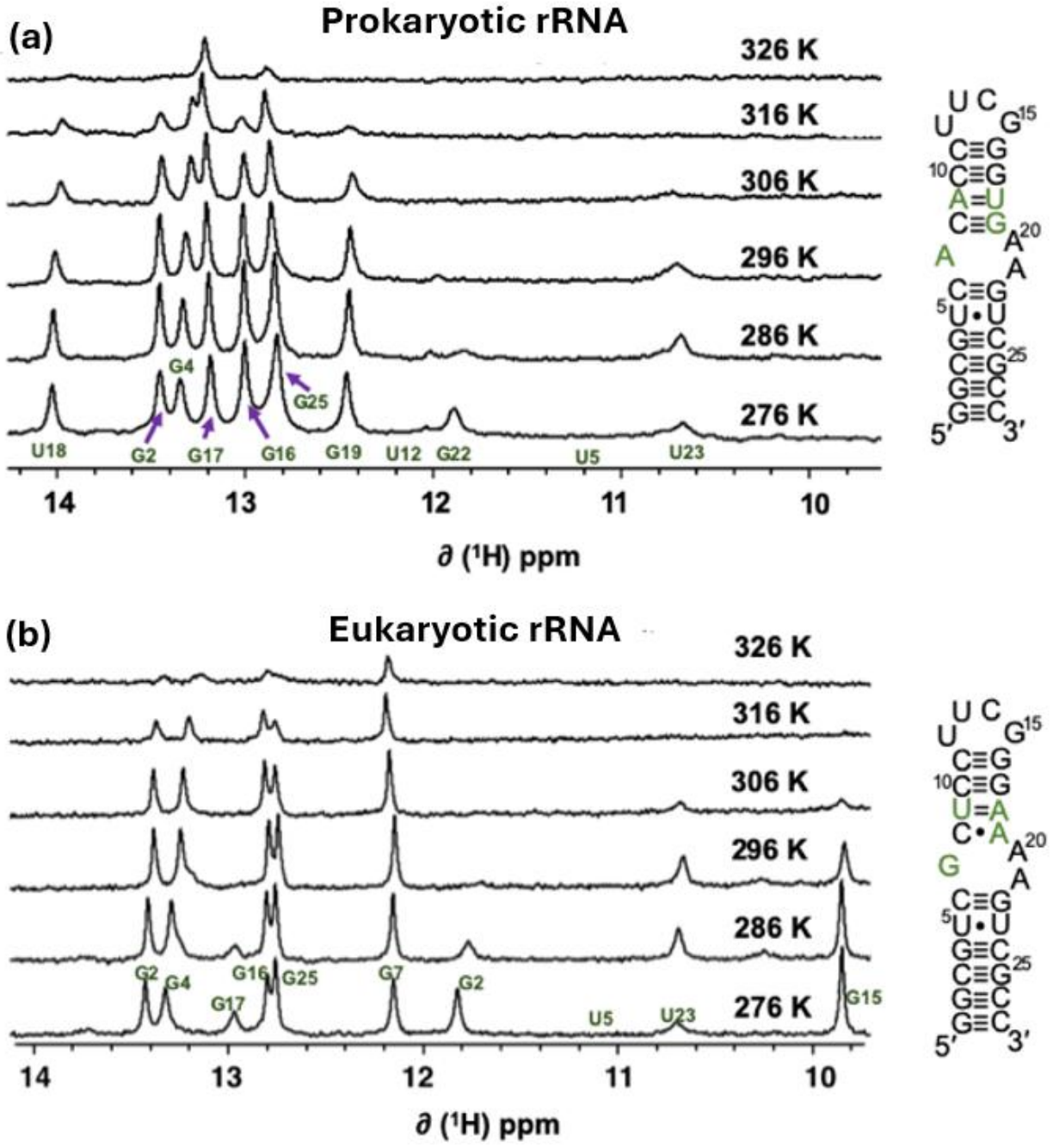

Figure 5.4 The NMR melt data of the prokaryotic **(a)** and eukaryotic A-site rRNA **(b)** The ^{1}H-imino region can be seen to range from 276 to 326 K.

5.7 R_1, R_2 and hNOE+ 1 NMR experiments can be used to assess differences in flexibility of the adenines

On the picosecond-to-nanosecond (ps-ns) time scale, spin relaxation experiments may provide information about motions within the rRNAs. Longitudinal (R_1) relaxation experiment depicts the decay of longitudinal magnetization with a rate constant R_1. The transverse relaxation experiment describes the decay of magnetization in the XY-plane with a rate constant of R_2. Finally, the heteronuclear Nuclear Overhauser Effect (hNOE) measures the rate at which proton magnetization is transferred to the heteroatom via their dipolar interaction. While the suite of relaxation experiments do not explicitly reveal the rate of chemical exchange that contributes to relaxation, these experiments do allow for a deeper understanding of the flexibility or rigidity of the nucleotides being probed **(Figure 5.5)**. In addition, we can further characterize the flexibility of the adenines by obtaining the ratio between the R_2 and R_1 rates (**Figure 5.6**). The R_2/R_1 ratio depicts flexibility of a nucleotide, and in future studies may be useful in generating other flexibility parameters.

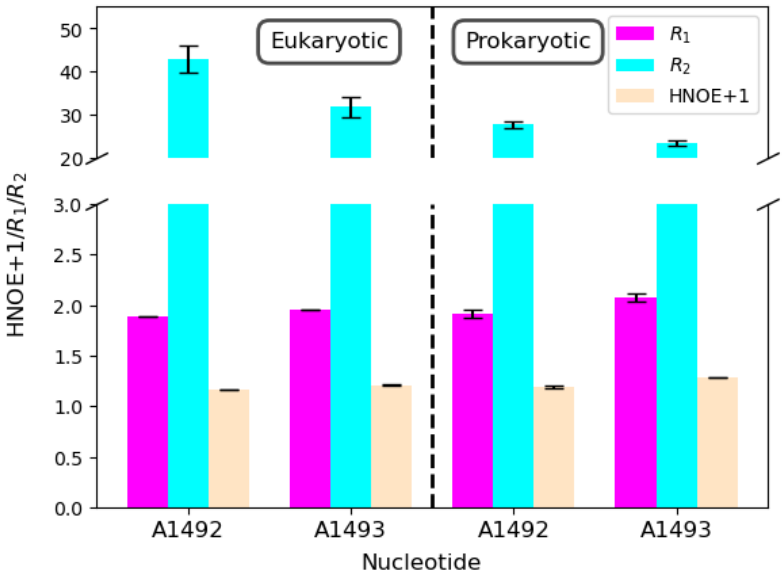

Figure 5.5 Bar chart shows the summary of the suite of spin-relaxation experimental results for the ^{13}C-8 adenine labeled sequences. Findings present eukaryotic A1492 to be of greatest flexibility followed by A1493. A similar trend of flexibility is seen in the prokaryotic A1492 and A1493. Comparatively, the eukaryotic A1492/93 is more flexible than the prokaryotic.

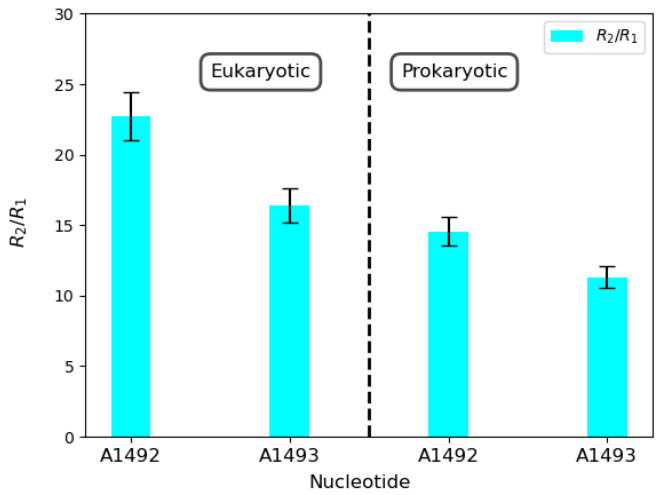

Figure 5.6 The R_2/R_1 ratios derived from experimental ^{13}C-8 adenine relaxation measurements for eukaryotic and prokaryotic rRNA at 600 MHz with a temperature of 25°C. The error bars represent ± standard deviation.

5.8 CPMG NMR as an NMR tool to observe exchange on a nucleotide-specific level

To further understand the differences in dynamics between the two rRNA's adenines, we elected to use the Carr-Purcell-Meiboom-Gill (CPMG) experiment. This choice was rooted in the experimental success from prior publications using this rRNA system [145]. Our CPMG experiment works to obtain the R_{2eff} during a constant-time period constituted by a train of equally spaced 180º refocusing pulses. This dispersion curve is the R_{2eff} plotted against the various frequencies applied (ν_{CPMG}) [140]. A flat curve implies there is not chemical exchange in the µs-ms timescale of the observed nuclei. In contrast, a non-flat dispersion curve implies the presence of chemical exchange. In our experiment we fit this data to a two-state chemical exchange model[141,142]. Through this we were able to gain insight into the kinetics (k_{ex}) of the adenines 1492/1493 within the prokaryotic and eukaryotic A-site rRNA constructs.

5.9 Dynamics differences exist between the two rRNAs on the ps-ns and µs-ms timescales

We compared both the thermal stability and the dynamics of the two sequences. We were interested in the dynamics differences at the location of nucleotides A1492 and A1493. This was a key point of focus due to their role in the fidelity of translation, and their current use in aminoglycoside drug performance. We used relaxation NMR experiments to accomplish this goal. We began our dynamics probing experiments with the longitudinal (R_1), transverse (R_2) and hNOE + 1 NMR experiments (**Figure 5.5**). We report that longitudinal experiments show enhanced flexibility in favor of prokaryotic rRNA, but differences between eukaryotic and prokaryotic flexibility is minimal (Appendix table 1). R_2 data and hNOE + 1 data co-confirm these conclusions. Additionally, the R_2/R_1 ratio (**Figure 5.6**) suggests there may be enhanced flexibility in the eukaryotic adenines as compared to the prokaryotic. We then used relaxation NMR (CPMG) to find the effective transverse relaxation rates (R_{2eff}) of the H8 atoms of the adenines 1492 and 1493 on the µs-ms timescale via a ^{1}H-based Carr–Purcell–Meiboom–Gill (CPMG) experiment that our group has used in several previous publications [145]. In the prokaryotic rRNA (**Figure 5.7**), we saw fast exchange taking place in both A1492 and A1493. The rate of exchange occurring is seen in (**Table 5.1**)[1].

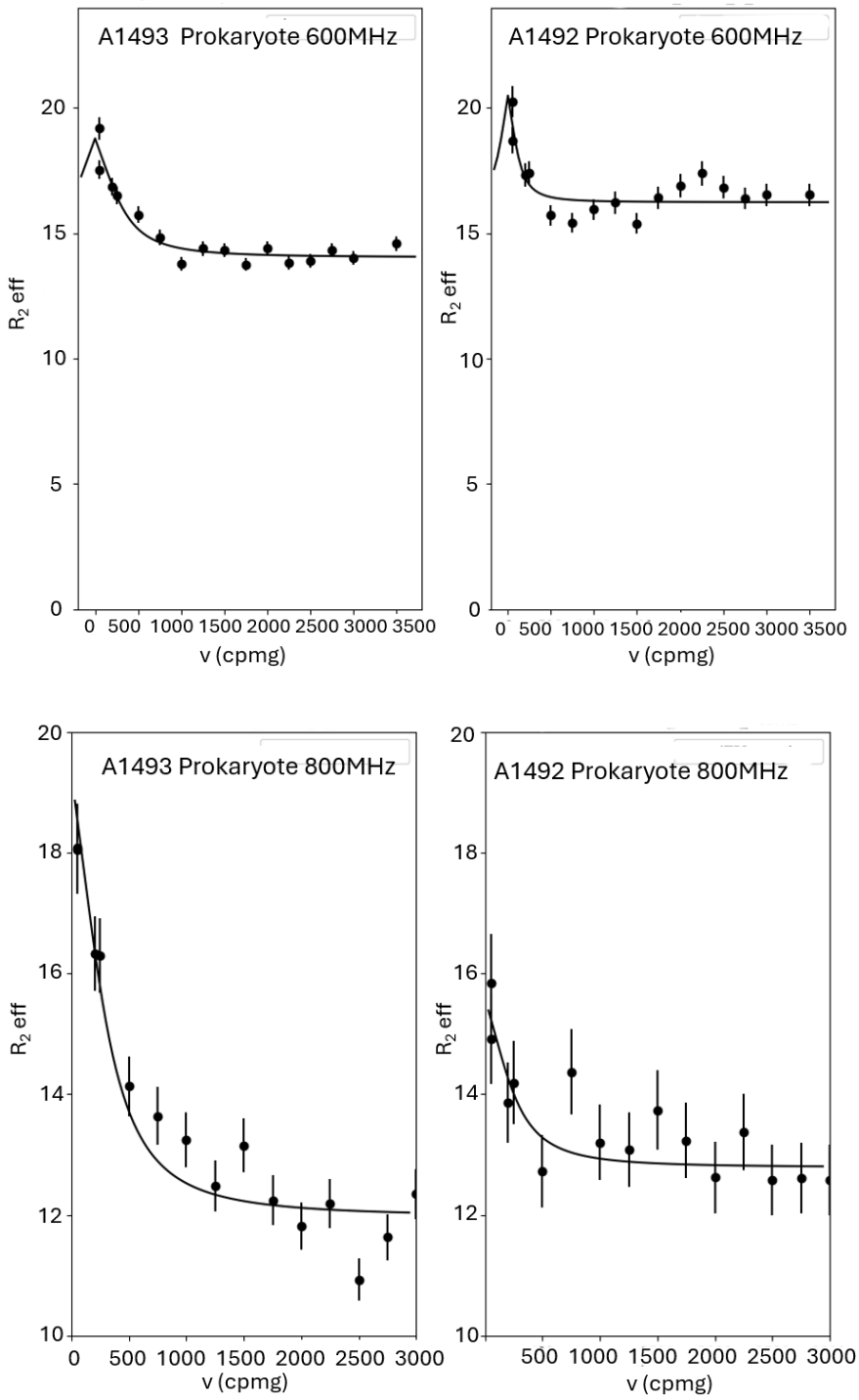

Figure 5.7 ^{1}H relaxation dispersion curves plotted as a function of $R_{2,}$eff against the ^{1}H CPMG pulse frequency of the prokaryotic A-site rRNA at a constant-time delay of 40 ms. This data was obtained at 600 and 800 MHz. A non-flat dispersion curve indicates the presence of exchange. The data was fit to the Bloch McConnell exchange model [167-168] using the RINGNMR software to obtain k_{ex} values [169].

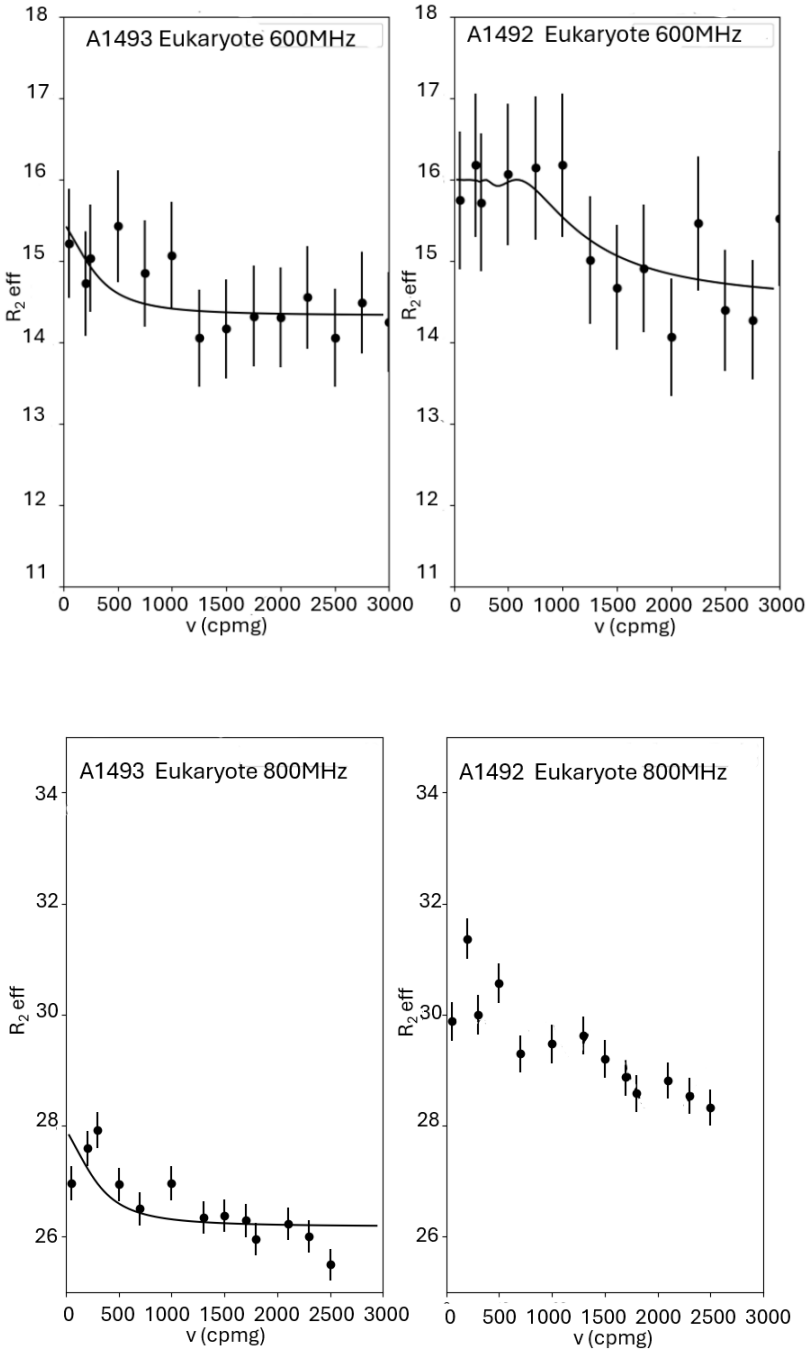

Figure 5.8 ^{1}H relaxation dispersion curves plotted as a function of R2,eff against the ^{1}H CPMG pulse frequency of the eukaryotic A-site rRNA at a constant-time delay of 40 ms. This data was obtained at 600 MHz.and 800 MHz. A non-flat dispersion curve indicates the presence of exchange. The data was fit to

the Bloch McConnell exchange model [167-168] using the RINGNMR software to obtain k_{ex} values [169]. Yet, the data from A1492 in the eukaryotic A-site rRNA could not be fit using this software

The eukaryotic A-site rRNA's Adenines 1492 and 1493 underwent fast and slow exchange respectively (**Figure 5.8**). 1492 had a fast k_{ex} exchange and 1493 had a slow k_{ex} exchange (**Table 5.1**) However, not all data could be fit by RINGNMR due to high error. After fitting the data with a 2-state exchange model in RINGNMR, we then used NESSY to report on exchange in 3-state models for slow, fast and intermediate regimes; the curves for those successfully fit, can be found in the appendix (**Appendix Figure 3 (a-e)**). Like RINGNMR [169], NESSY uses a statistical model framework for selection of best fit [195]. While RINGNMR uses AIC and RMS to select the best model for the user, NESSY uses residuals, maximum likelihood fitting, AIC and F-tests. NESSY could not fit the eukaryotic A-site rRNA 1493 and thus reported it to have no exchange. NESSY reported the prokaryotic adenine 1492 to have a k_{ex} value of 516.90 ± 62.78 s^{-1} and 4788.30 ± 577.68 s^{-1} on the 600 and 800MHz, respectively. Adenine 1493 in the prokaryotic sequence had a k_{ex} value of 1878.53 ± 144.47 s^{-1} and 3771.02 ± 229.74 s^{-1} on the 600 and 800MHz, respectively. In the eukaryotic sequence NESSY could not fit adenine 1492 and 1493 from the 800MHz data. NESSY did conclude that the adenine 1493 based on 600MHz data had a k_{ex} value of 3889.66 ± 930.909 s^{-1}, but NESSY could not fit adenine 1492 from the 600MHz data. (**Table 5.1)** summarizes these results.

Table 5.1 The summarized findings from NESSY and RINGNMR software for the CPMG data

Species	Residue	Software	600 MHz	800MHz
Bacterial	A1492	NESSY RING	516.90 ± 62.78 s^{-1} 775.96 ± 384.50 s^{-1}	4788.30 ± 577.68 s^{-1} 2000 ± 369.38 s^{-1}
Bacterial	A1493	NESSY RING	1878.53 ± 144.47 s^{-1} 1999 ± 330s^{-1}	3771.02 ± 229.74 s^{-1} 2000 ± .418 s^{-1}
Human	A1492	NESSY RING	No fit 1999.83 ± 33.86 s^{-1}	No fit Error too high despite fit
Human	A1493	NESSY RING	3889.66 ± 930.909 s^{-1} 22.66 ± 13.88 s^{-1}	No fit No fit

In short, the R_1, R_2, hNOE+ 1, and CPMG experiments underscore that while there are similarities in the thermal stabilities and secondary sequences, there are key differences in the rates of exchange from the prokaryotic bulge region compared to the eukaryotic A-site rRNA. Previous experiments [167] show the results of fluorescence studies using the 2-AP fluorescent analog of adenine. This enables the observation of A1492 and A1493 in the A-site rRNA of the prokaryotic sequence. When the base was stacked and intrahelical, its fluorescence readings were low. When the base flipped out or became extra-helical, fluorescence increased. Thus, by measuring fluorescence intensity, they inferred the intrahelical and extra helical lifetimes. While they did not compare the prokaryotic and eukaryotic sequences, they did compare if the binding affinity or the extrahelical lifetimes were connected to the potency of the aminoglycosides (**Table 5.2)**

Table 5.2 The summarized results from previous literature [167] depicting the connection between extra-helical life times and the potency of an aminoglycoside

Drug name	MIC (uM)	Ka (M^{-1})	Immobilize 92/93
ribostamycin	25	$1.2 \pm 0.1 \times 10^5$	1.04 ± 0.02 ns
paromomycin	12.5	$2.1 \pm 0.3 \times 10^6$	1.68 ± 0.05 ns
gentamycin	6.3	$5.4 \pm 0.4 \times 10^4$	2.00 ± 0.10 ns
neomycin	3.1	$3.0 \pm 0.5 \times 10^7$	2.29 ± 0.07 ns

Their study showed no correlation between binding affinity and potency, but rather found an association of longer extra helical lifetimes with drug potency. This connection motivated our study to examine differences in these lifetimes between the prokaryotic and eukaryotic sequence. Our results emphasize the need to factor in RNA dynamics into the drug design process.

5.10 Summary of chapter 5

Aminoglycosides function by modulating the nucleobases A1492 and A1493, and this results in aberrant protein synthesis [125]. While aminoglycosides are effective, the matter of their selectivity could be improved upon. The eukaryotic A-site rRNA is quite like the prokaryotic A-site rRNA, and their interaction with aminoglycosides have been associated with some deleterious side effects [31-34]. In efforts to design new antimicrobials or improve current ones, the specificity by which binding takes place must be improved. If the adenine 1493 of the eukaryotic A-site rRNA is in slower exchange this implies it spends more time in the extra helical position than its eukaryotic counterpart. Improvements in this area of research require an initial understanding of the dynamics involved and the differences between the eukaryotic and prokaryotic systems. Thus, we probed the differences and similarities in dynamics μs-ms timescale by NMR and tested their thermal stabilities using UV spectroscopy and NMR. Future studies

from our group may consist of utilizing other adenine specific isotopic labeling patterns to co-confirm the findings herein.

CHAPTER 6

6.0 The focus of chapter 6

In this chapter, I describe dynamics studies of an HIV-2 RNA. I purified an isotopically labeled uracil nucleotide triphosphate and successfully incorporated it into the TAR-2 RNA fragment. I then run a series of dynamics experiments with this RNA and summarize the main findings of these. Understanding this aspect of the TAR RNA has proven fruitful in drug development for the TAR-1 RNA sequence [79]. Additionally, this chapter uses TAR-2 RNA as a model construct for teaching undergraduates with little to no pre-existing knowledge about NMR theory. Within the chapter I share an overview of the cadence and techniques I used to teach a NMR theory and relaxation data processing course. I anticipate that this material could be adapted to teaching first year graduate students about NMR theory and relaxation data processing as well.

6.1 TAR-2 RNA is a target which has been previously researched

The Human Immunodeficiency Virus (HIV) negatively impacts millions around the globe [35]. HIV is predominantly found in two types: HIV-1 and HIV-2. As stated in chapter 1, these two have differences in their regions where found, and speed in progression to AIDS.[148-151]. Chapter 1 discussed the RNA element in HIV, which is paramount to the replication process is the Trans-Activation Response element (TAR). TAR is present in both HIV-1 and HIV-2. As mentioned in chapter 1, the site of binding in the HIV-1 TAR, Tat complex has been identified as an arginine-rich region [151-153]. Considering this, the Williamson group executed various NMR dynamics experiments using an HIV-2 TAR-argininamide complex [75,76]. This experiment was a model for the aforementioned binding interaction between HIV-1 TAR RNA and the Tat protein. Like the behavior of HIV-1 TAR, the HIV-2 TAR binds to Tat. This binding catalyzes conformational changes within the HIV-2 TAR RNA based on their work.

The Williamson group performed their TAR-2 NMR-based studies uniformly labeled with ^{15}N and ^{13}C [73, 147] RNA. However, uniform labeling patterns are known to introduce scalar and dipolar couplings complicating analysis of NMR measurements.[113, 155-156]. Couplings can impact the detection of NMR peaks from RNA and limit the accuracy of the findings [155–156]. In efforts to circumvent this obstacle, our chemo-enzymatic labeling approach was used for the incorporation of site-specific labeling (**Figure 6.1**)[157]. The use of these labels allowed us to explore NMR experiments that were previously not available for use [72]. This work promoted more detailed findings by using the previously not accessible experiment, CPMG, and this work rendered results with enhanced accuracy surrounding the dynamics of the therapeutic target, TAR-2 construct.

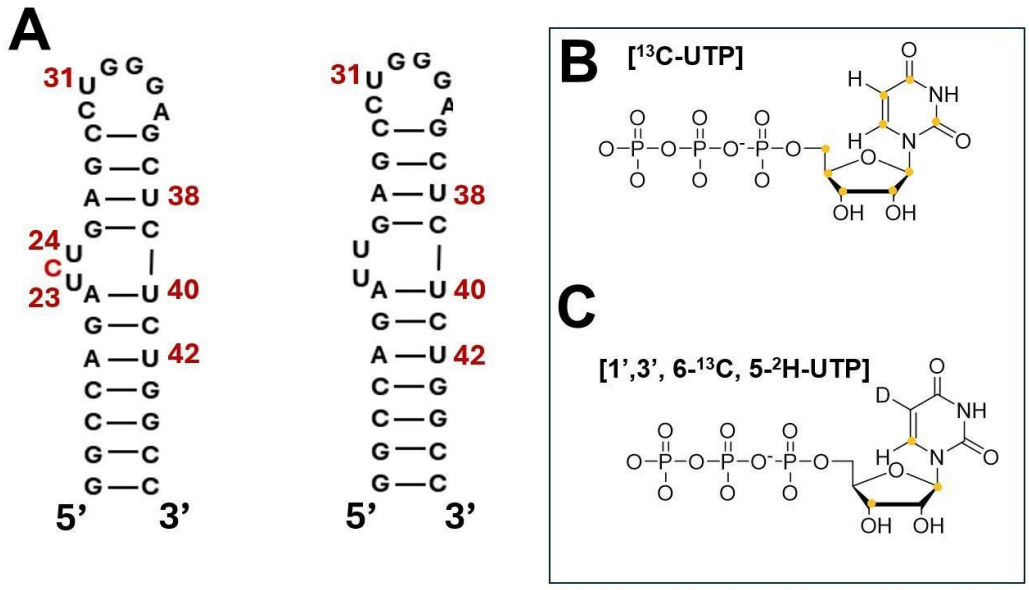

Figure 6.1 (A) The TAR-1 and TAR-2 secondary structures. The red-colored C in TAR-1 remains the key secondary sequence difference between the two. The two, uracil nucleotide triphosphate (UTP) structures are shown in **(B)** and **(C).** The yellow labeling serves to be indicative of the placement of a carbon-13 isotopic label. **(B)** shows the uniformly labeled UTP, while **(C)** shows the 1',3', 6-^{13}C, 5-^{2}H site-specifically labeled UTP.

In this work, we used NMR spectroscopy to observe the dynamics of the HIV-2 TAR RNA sequence (TAR-2), with focus devoted to the uracil residues via our site-selective ^{13}C chemo-enzymatic

labeling technique. The specific labeled (*1',3', 6-^{13}C, 5-^{2}H*) positions, and nucleotides can be seen in Figure 6.1. We used Carr-Purcell-Meiboom-Gill (CPMG) relaxation dispersion and transverse spin relaxation dispersion (R_2), longitudinal spin lattice relaxation dynamics and heteronuclear NOE (R_1, hNOE + 1) measurements to look at the TAR-2 ^{13}C6-H6 spin system on the picosecond to millisecond timescale. Improved knowledge of these dynamics and how they facilitate interactions with the Tat protein could promote the design of medication which targets the HIV-2 TAR RNA.

6.2 R_1 experiment with TAR-2 fragment RNA displays differences in flexibility between uracils located in bulges and helices

We wanted to know where the TAR-2 RNA's internal motions would be detected; thus, we planned and performed a series of high-frequency NMR experiments specific to monitoring the ^{13}C6-H6 spin system of the uracils. We recorded their longitudinal (R_1) relaxation, transverse (R_2) relaxation, and relaxation dispersion (CPMG) values. The R_1 experiment is commonly used to probe relaxation decay of longitudinal magnetization. In this experiment we use several 2D NMRs at varying delay times; we plot the ^{13}C6-H6 uracil signal intensities versus delay times to obtain an exponential decay curve, and from the exponential decay fitting equation, the relaxation rate, R_1 can be determined (**Figure 6.2**).

To extract the longitudinal relaxation rate (R_1), the signal versus delay time plot is fitted to a single-exponential function using the RELAXFIT MATLAB script for each uracil residue. Error analysis was executed using the same RELAXFIT MATLAB script with a duplicate delay data point (**Figure 6.2**)[159,160]. In this experiment, the possession of an elevated R_1 value is connected to having enhanced flexibility when compared with a low R_1 value.[161,162] We deduced from the R_1 experiment that the^{13}C6 atoms on the uracil in the bulge decay faster than the ^{13}C6 atoms on the uracil in the helices; we also assumed, based on this experiment, that the ^{13}C6 atoms on the uracils in the bulges are more flexible than those in the helices.

6.3 hNOE + 1 experiment with TAR-2 fragment RNA highlights the flexibility of the uracils.

The hNOE + 1 experiment may provide extra dynamics content when added to R_1 and R_2 data. The hNOE + 1 experiment detects flexibility on the picosecond time scale.[166] The experiment observes fluctuations in spin magnetization of a heteronuclear system when a proton is saturated by rf pulses[163]. This experiment found in Figure 2, that there are elevated hNOE+1 signals from half of the Uracils studied. Here we see the beauty of our lab-signature, site-specific labels. They removed any potential unwanted cross relaxation effects. When working with uniform ^{13}C labels, it is a possibility that the adjacently isotopically labeled carbons' protons may undergo ^{13}C longitudinal cross relaxation. This would lead to increased intensities (enhanced hNOE + 1 signals) of peaks on the resulting 2D spectra. Yet, these site-specific labels afforded the option to remove any potential cross relaxation which could have occurred by exchanging the hydrogen on H5 with a deuterium. Therefore, we removed the potential for the C5 carbon's proton which is adjacent to our ^{13}C labeled C6's proton to experience any enhanced detections of hNOE + 1 signals.

6.4 R_2 relaxation dispersion experiment shows a similar trend that the uracils located in the bulge are more flexible than uracil in helices

We determined the R_1 (longitudinal relaxation rate) value from the uracils studied in the NMR experiments. Additionally, we used a NMR experiment to find the R_2 (transverse relaxation rate constant) [158,163,164]. From this experiment we find that flexible nucleotides have decreased R_2 values[161-162]. Figure 6 shows the normalized peak intensities versus delay times from the R_2 experiment. Single exponential decay curve fitting and error analysis was achieved by using RELAXFIT.[159,160] When the intensities are fit to an exponential decay curve, a R_2 value of each of the six uracils could be derived. We found that the $^{13}C6$ uracils with the lowest R_2 values were the ones in the bulges.

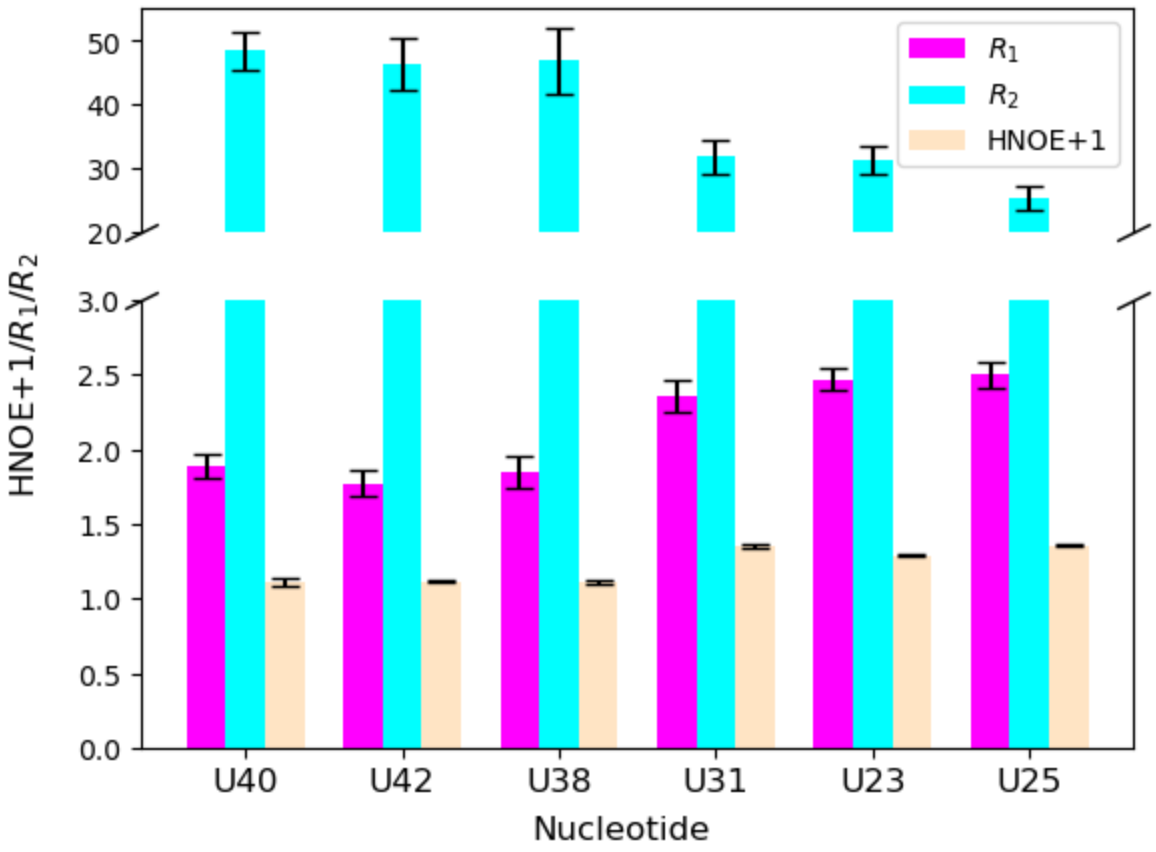

Figure 6.2 The uracil relaxation measurements for 1',3', 6-^{13}C, 5-^{2}H -UTP in TAR-2 RNA from 600 MHz at 25 °C. Uracil R_1, and R_2, rates and steady-state hNOE measurements are shown herein. The error bars represent ± s.d. The Residues U31, U23 and U25 show high R_1, hNOE, and low R_2. This suggests the occurrence of increased internal motions within these residues. The Y-axis depicts rates (1/s) of R_1 and R_2 and the dimensionless unit of hNOE + 1.

We compared the R_1, R_2 and NOE+ 1 data, and saw that the ^{13}C6 atoms on the uracils in the bulges were more dynamic than those in the helices. We also compared the flexibility of the ^{13}C6 atoms on the uracils by studying the ratio between the R_2 and R_1 rates. The R_2/R_1 ratio is an extra analysis that can provide us with an additional way of looking at the data (**Figure 6.3**). The R_2/R_1 ratio yields a normalized, field-independent picture of the molecular motion the TAR-2 experiences by incorporating the R_2 and R_1 relaxation processes. Both R_1 and R_2 primarily reflect ps-ns motions due to dipole-dipole and chemical

shielding anisotropy relaxation mechanisms. The ratio of the two also report on motional heterogeneity across nucleotides. However, RNA is dynamic and may deviate from the average of this ratio. The average of this ratio bar provides a baseline for differences in motion. Deviations from the baseline, seen as elevated R_2/R_1 ratios, would signal that those nucleotides may be experiencing conformational exchange[170]. This would prompt the investigating a slower timescale of NMR relaxation experiments.

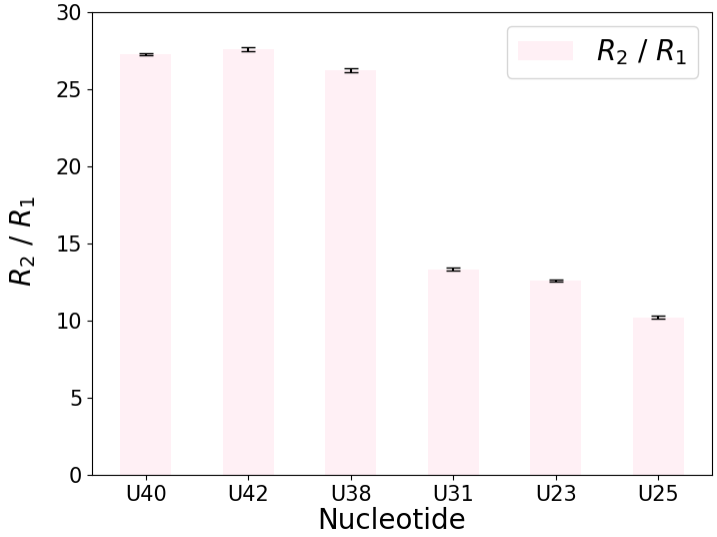

Figure 6.3 The R_2/R_1 ratios derived from experimental uracil C6 relaxation measurements for 1',3', 6-^{13}C, 5-^{2}H -UTP labeled TAR-2 at 600 MHz with a temperature of 25°C. The error bars represent ± standard deviation.

6.5 CPMG experiment with TAR-2 fragment RNA will show which H6 atoms on the uracils are in exchange.

From the R_1, R_2, hNOE +1 experiments, we learned that the uracils in the bulges are more flexible than those in the helices (**Figure 6.2**). Yet, there remains a lack of knowledge regarding which uracils are in exchange. CPMG will be used to measure the effective transverse relaxation rates (R_{2eff}) of the uracils on the µs-ms on both a 600 and 800 MHz NMR spectrometer magnetic fields. [165-167] In our CPMG experiment, the R_{2eff} will be determined using a constant-time period containing a train of equally spaced 180º refocusing pulses.[146] The conformational exchange will be seen by a non-flat curve in a plot of R_{2eff}

as a function of the CPMG field (ν_{CPMG}). A flat dispersion curve will imply that no exchange in the nuclei could be detected on that timescale. We will fit the data to a two-state chemical exchange model using the Carver-Richards equations shown in chapter 3 [167,168]. With the assistance of RINGNMR software,[171] we will gain insight into the kinetics (k_{ex}) of which the uracils underwent fast, slow or no exchange on the µs-ms timescale.

Chapter 7

7.0 Author contributions for chapter 7

The research and data presented in this chapter were conducted as part of a collaborative project with Frances Stump, a fellow graduate student in the Chemistry & Biochemistry Department. Both of us contributed equally to experimental design, data collection, and analysis. As a result, figures 6.1 and 6.2 may also appear in Frances's thesis submitted to the University of Maryland, College Park. The inclusion of these materials in both theses reflects our shared contribution to the work and has been approved by our advisor, Dr. T.K. Dayie.

7.1 Learning objectives of teaching NMR theory and dynamics to undergraduate students

NMR spectroscopy has been used as an instrument in the field of TAR RNA-based drug development [171]. One instrumental steppingstone used in the pathway to TAR RNA-based drug discovery was the structure and dynamics analysis of its intended therapeutic target using NMR [172-176, 79]. Recent data states that only a small percentage of chemistry and biochemistry undergraduates will attend graduate schools [179]. This implies that many of these undergraduates will enter the work force upon graduation with their undergraduate biology STEM degrees. It was desirable to equip these students with skills which may be transferable to various biological occupations. It was our overall research goal to provide students with the ability to interpret dynamics data from a simple NMR experiment on at minimum a novice level. Our goal was executed by implementing the following objectives: to equip the students with background knowledge in classical NMR theory, teach the students about RNA structure assignment through NMR

data base BMRB, educate students in the classical T_1 experiment theory, and provide the students with our previously collected raw T_1 data from the work with the TAR-2 construct. The students used this raw data to reprocess and draw their own conclusions about the flexibility of the uracil residues. Students were provided with pre and post-assessments which covered multiple choice and open response questions from all the specific goals of teaching. The pre and post assessments were used to document the furtherance of their knowledge in the subject matter; the pre-assessment was administered on the first day or class, and the post-assessment was administered on the last day or class. Students were also given, simultaneously to the pre and post assessments, a pre and post self-assessment. The self-assessment was useful in gauging the growth of the students' confidence levels in the subject matter.

7.2 Practicum cadence of teaching material

The curriculum for this course was designed to be taught in three lectures; however, the material may be expounded upon in deeper detail to promote a longer series of lectures being taught. We developed this course with several assumptions regarding the students' pre-existing knowledge relevant to the course. We assumed students would recall the following foundational concepts: electron donating and withdrawing properties, the periodic table of elements, atoms, basic organic chemistry functional groups, and the radiation spectrum. This implies that a great deal of traditionally needed physics, quantum mechanics, and other underlying theory was not a prerequisite for learning. This was intentional as we desired to develop a curriculum that could be taught to those of diverse educational foundations. In this first lecture we taught students about the theory of NMR, the components of the NMR spectra, not specific to biomolecules, and the interpretation for simple pulse programs. In the second lecture we taught the students to interpret the NMR spectra relevant to RNA nucleotides, to utilize the BMRB for RNA structures, and the inversion recovery theory of the relaxation experiment, T_1. In the final lecture we provided students with raw NMR files from a T_1 experiment performed on a RNA structure. In this final lecture, the students learned how to independently process the data and determine the R_1 values of the nucleotides which were monitored during the T_1 experiment. They also were educated concerning the relationship between T_1 and R_1, and how R_1 values relate to flexibility.

7.3 Teaching NMR theory and dynamics to undergraduates improves self-confidence and general understanding

From the results of the pre/post-assessments and the pre/post self-assessments, we find that the students improved significantly in both their self-confidence and their understanding of the subject matter (**Figures 7.1 and 7.2**). The students assembled a research poster which was presented at a NASA-hosted symposium. One of the students has since joined me in my work and has rerouted his plans of becoming a medical doctor, to becoming a chemist with great interest in applying to UMD for fall 2026 to join the Dayie lab.

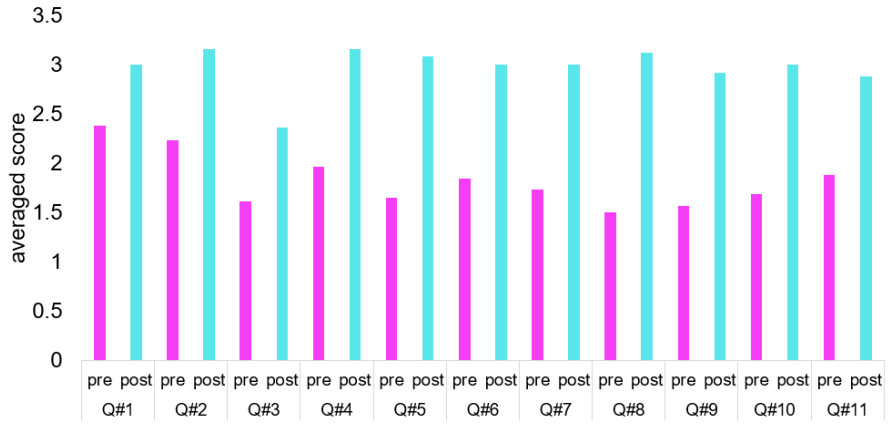

Figure 7.1 *The average scores of self-assessments per question. These scores are compared to the pre- and post-self-assessments. (cyan) The post self-assessment compared with the (magenta) pre-self-assessment results show the significant growth in self confidence which came from the students.*

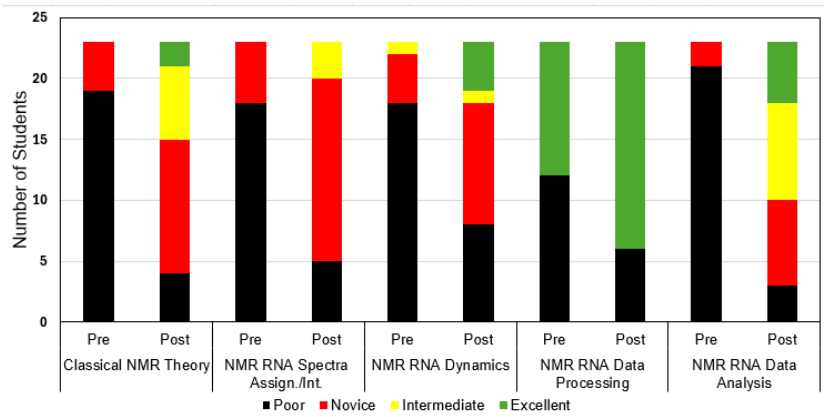

Figure 7.2 *The bar chart shows the results of the pre and post assessments administered to the student. While students improved in all areas overall, we find that the areas which students developed significantly in were the classical NMR theory, NMR RNA dynamics, and NMR RNA data analysis sections.*

7.4 Summary of the work in chapter 6 and 7

We probed dynamics across the ps-ns and µs-ms timescales to comprehend the internal motions of the HIV-2 TAR-2 RNA sequence. We witnessed a general trend of greater flexibility in the bulge residues when compared to those in helices. This trend was consistent across R_1, R_2 and hNOE experiments (**Figures 6.2 and 6.3**). These results aligned with earlier studies conducted on uniformly ^{13}C-labeled HIV-2 TAR RNA but provide more detailed insights by resolving the U31 and U42 peaks which were previously not visible due to scalar couplings [72]. It is worthwhile to underscore that the longitudinal relaxation rates measured in this thesis are lower than those reported in the Williamson group's work with the exception of U23. This alludes that prior values may have been overestimated. R_1, R_2 and hNOE experiments were useful in comparing flexibility between the groups of uracils. These experiments had limitations in that they could not highlight residue-specific exchange rates. This limitation will be addressed by incorporating the CPMG experiment. CPMG will showcase detailed nucleotide-specific exchange on the µs-ms timescale. Through the CPMG experiment we will learn which uracils are in slow exchange, fast exchange or experiencing no exchange. The CPMG information is critical for uncovering TAR-2 RNA's functional dynamics. This work is a part of a larger effort to assemble a full picture of the HIV-2 TAR RNA's structural and dynamic ensemble. We also used the R_1 experimental results and incorporated it into an undergraduate teaching practicum. The general feedback from the student body

was positive and this course has encouraged students from the class to participate in NMR-based undergraduate research. The future work is to build on this by systematically studying the dynamics of each nucleotide in the TAR-2 sequence using various isotopic labels. It is anticipated that we will be able to map the full range of conformational states accessible to TAR-2 RNA as has been accomplished with the TAR-1 sequence which has resulted in medicinal developments [79]. It may also be exciting to see future iterations of our practicum take place with minor improvements to the lecturing style.

Chapter 8

8.0 The focus of chapter 8

The future directions of this research expand the use of our isotopes to further characterize the dynamics of the A-site and TAR-2 sequences by NMR and complementary spectroscopic methods. Both sequences are connected to major global challenges: antimicrobial resistance and HIV. Both rely on nucleotides that participate in binding events to perform their activity. The use of site-specific ^{13}C-8 adenine labeling has proven to be effective at monitoring nucleotide-level motions on the ps-ns and µs-ms timescales. A coherent next step of this research is to extend our labeling strategies to other rRNA constructs, such as the one found in human mitochondria, to better understand way to improve aminoglycosides. Or to incorporate other labels into the TAR-2 sequence to fully map the dynamics of the RNA.

8.1 Future directions

An immediate direction includes the incorporation of the ^{13}C-8 adenine label to the mitochondrial A-site rRNA. Aminoglycosides are reported to exhibit off-target interactions with this mitochondrial rRNA. Although mitochondrial and bacterial ribosomes possess distinct sequence variations and thus, observing their conformational exchange is of interest. An investigation of the counter parts of adenines 1492 and 1493 in the mitochondrial rRNA [121] would reveal whether these nucleotides experience similar or distinct dynamic behavior relative to the bacterial and cytosolic eukaryotic A-site sequences. By using the same

labeling scheme used in Chapter 5, it would be possible to compare all three rRNA under identical NMR experimental conditions. The longitudinal and transverse relaxation experiments (R_1, R_2, and hNOE) would characterize flexibility, while CPMG R_{1r} and CEST relaxation dispersion experiments would identify differences in conformational exchange between the intra and extra helical lifetimes.

For TAR-2 future directions, the ability to apply the use of our adenine label to nucleotides within the TAR-2 sequence would be enlightening as there is an adenine involved in the binding pocket, A27 [63]. Generating TAR-2 fragments that are specifically isotopically labeled at A27 is a powerful method to resolve these microsecond-millisecond, site-specific dynamics that are otherwise difficult to observe. This data would complement the work accomplished in chapter 6.

While NMR is a well-suited technique for studying site-specific dynamics in RNA, other spectroscopic tools may be useful as well. UV melting could be used to compare the thermal stability of the bacterial, mitochondrial and eukaryotic A-site constructs. Those findings could be compared with NMR for co-confirmation.

Furthermore, my results and methods presented throughout this dissertation suggest an additional direction: using labeled RNA NMR data for computational modeling. Molecular dynamics simulations using data generated by R_1, R_2, hNOE, and relaxation dispersion-derived may be vital for identifying and characterizing the relevant conformational states that facilitate functional interactions, directly impacting the rational design and efficacy of new drugs. This data may assist in visualizing transient conformations that are difficult to isolate through experimental means. This would also assist in predicting behavior of the RNAs as well.

8.2 Summary of chapter 8

In summary, future research will involve applying the new ^{13}C-8 adenine labeling method to study mitochondrial A-site rRNA, and the Tat-binding pocket of TAR-2. If NMR relaxation is integrated with UV melting, such studies can provide a more comprehensive and comparative study of RNA conformational dynamics, in efforts to better understand and anticipate activity.

Appendices

RNA preparation

The 27-nt and 30-nt RNA fragments used in this study were synthesized from DNA templates (TAR: 5´-GGC CAG AGA GCT CCC AGG CTC AAT CTG GCC TAT AGT GAG TCG TAT TAG-3´), (A-site Bacteria: 5´-mGmGC GAC TTC ACC CGA AGG TGT GAC GCC TAT AGT GAG TCG TAT TAG-3´), (A-site Human: 5´-mGmGC GAC TTT TCC CGA AGG AGC GAC GCT ATA GTG AGT CGT ATT TAG-3´) (promotor sequence: 5´- CTA TAG TGA GTC GTA TTA G-3´) purchased from Integrated DNA Technologies (IDT) Coralville, IA. Site selectively labeled 8-^{13}C-ATP (A-site rRNA samples) and 1',3',6-^{13}C,5-^{2}H (TAR-2 sample) were synthesized via a T7 polymerase-based *in-vitro* transcription reaction from DNA templates. The different RNAs were synthesized in a 10 mL reaction carried out at 310 K for 3 h. The reaction mixture was composed of 1X transcription buffer (40 mM Tris-HCl pH 8.0, 1 mM spermidine and 0.01% TritonX-100), 80 mg/mL PEG, 1 mM DTT, 20% DMSO, 2.5 mM NTPs (e.g.: 2.5mM ATP, 2.5mM GTP, 2.5mM CTP, or 2.5mM UTP) that were unlabeled and or site selectively labeled, 7.5 mM $MgCl_2$, 0.3 µM single strand DNA template for the individual RNA, 2 U/µL thermostable inorganic pyrophosphatase (TIPP) and 10 mg/mL T7 RNA polymerase. Following transcription, the RNAs were purified by 12% preparative acrylamide gel and electroeluted at 200 V in 1X TBE (Tris Borate Ethylenediaminetetraacetic acid (EDTA)). The samples were then exchanged into deionized water, lyophilized and then dissolved in 1X NMR buffer (50 mM sodium phosphate (pH 6.5), 50 mM sodium chloride, 0.1 mM EDTA, 0.1 mM, 0.1 mM 4,4-Dimethyl-4-silapentane-1-sulfonic acid (DSS), 100% D_2O, 0.02% NaN_3). The average concentration of the purified samples as determined using a Nanodrop at 260 nm was 0.5 mM. The molar extinction coefficients used were 387.5 mM^{-1} cm^{-1} TAR-2 and 283 mM^{-1} cm^{-1} for A-site sequences.

NMR data

All NMR experiments were performed at 298 K on an Avance III Bruker Ultrashield Plus 600 MHz spectrometer equipped with a triple resonance probe (^{1}H, ^{13}C, and ^{15}N) or a 800 MHz spectrometer with a QCI-31P cryoprobe. 2D and pseudo-3D data were processed and displayed using the Bruker software Topspin version 4.0.7 and RINGNMR software.

R_1 and R_2 (A-site RNA specific)

Transverse relaxation optimized spectroscopy (TROSY) based pulse sequences adapted from earlier works were used to obtain R_1, and R_2, data. R_2 relaxation rates were measured by carrying out an R_2 experiment. For the pseudo-3D R_1 and R_2, experiments, a hard 180º pulse was applied during the second INEPT period in place of selective pulses normally applied for decoupling of ^{13}C-^{13}C scalar couplings in a uniform labeled RNA. The carrier and sweep widths for the indirect dimensions were optimized for the C6, atom. The ^{13}C carrier was set to 140.4 ppm for UTP-C6 and the ^{1}H carrier was set to 4.7 ppm. The sweep width was set to 4.0 ppm for F1 dimension and 8.6 ppm for F2 dimension. The recycle delay (D1) in the R_1, hNOE and R_2 experiments were set to 2.5 s recycle; 6 (R_1) and 7 (R_2) delay times were used to extract relaxation rates. The delay times for the R_1 experiments were: 0.05, 0.1, 0.2 (duplicate), 0.4, 0.5, 0.6, and 0.7 seconds, while the $R_{1\rho}$ measurements were performed using delay times of 4 (duplicate), 8, 16, 28, 36, 48 milliseconds. The coupling constants for all experiments were set to 185 Hz for the C6 atom. For each FID, an average of 64 scans and 1024 complex points were collected. The coupling constants for all experiments were set to 185 Hz for the uracil $^{13}C6$ atom. For each FID, an average of 64 scans and 1024 complex points were collected. The ^{1}H spectra were referenced to internal DSS while the ^{13}C dimension was referenced by multiplying the proton frequency at 0 ppm by the gyromagnetic ratio (γ) of ^{1}H to ^{13}C. The MATLAB program RELAXFIT was used for relaxation rate extraction and Monte-Carlo error estimation was made from duplicate delay times for R_1 experiment and R_2. From the R_1 and R_2 values obtained, corrected R_2 values were determined using the following equation:

$$R_2 = \left(\frac{R_{1\rho}}{sin^2\theta}\right) - \left(\frac{R_1}{tan^2\theta}\right) \; ; \; \theta = \; \tan^{-1}\left(\frac{\omega_1}{\Omega}\right)$$

Equation 1

ω_1 is equal to the strength of the spin-lock field (1.6 kHz) and Ω is equal to the ^{13}C chemical shift offset in Hz.

hNOE (A-site RNA specific)

The hNOE experiment consisted of **duplicates** of saturated and unsaturated NMR experiments; this was done to perform error analysis. To saturate the proton, a hard 180° pulse was applied. The saturated hNOE experiments used a saturation delay (D35) of **5s**. The unsaturated hNOE, used a delay (D9) of **6.5s** was used. The NOE+1 values reported in Figure 7 were obtained using the equation:

$$NOE \; + 1 \; = \left(\frac{I_{sat} - I_{no\ sat}}{I_{no\ sat}} \right)$$

Equation 2

^{1}H CPMG (A-site RNA specific)

For relaxation dispersion CPMG experiments, R_{2eff} rates were obtained using a CPMG module consisting of a train of 180º pulse inserted between a series of delays (τCPMG- π- τCPMG). The R_2eff is expressed as a function of the frequency at which the 180º pulses are applied (V_{CPMG}) during a constant relaxation time[51] (τ_{relax}) where $\tau_{relax} = 2 \times N \times \tau_{CPMG}$. The coupling constant was set to 215 Hz. For each FID, an average of 16 scans and 1024 complex points were collected. The recycle delay for this experiment was set to 2.5s, and a constant-time delay (TCPMG) of 40ms was employed. Each delay

curve can be fit to analytical solutions for quantifying slow, intermediate or chemical contribution to transverse relaxation rates.

R_1 and R_2 (TAR-2 RNA specific)

Transverse relaxation optimized spectroscopy (TROSY) based pulse sequences adapted from earlier works were used to obtain R_1, and R_2, data. R_2 relaxation rates were measured by carrying out an R_2 experiment. For the pseudo-3D R_1 and R_2, experiments, a hard 180º pulse was applied during the second INEPT period in place of selective pulses normally applied for decoupling of ^{13}C-^{13}C scalar couplings in a uniform labeled RNA. The carrier and sweep widths for the indirect dimensions were optimized for the C6, atom. The ^{13}C carrier was set to 140.4 ppm for UTP-C6 and the ^{1}H carrier was set to 4.7 ppm. The sweep width was set to 4.0 ppm for F1 dimension and 8.6 ppm for F2 dimension. The recycle delay (D1) in the R_1, hNOE and R_2 experiments were set to 2.5 s; 6 (R_1) and 7 (R_2) delay times were used to extract relaxation rates. The delay times for the R_1 experiments were: 0.05, 0.1, 0.2 (duplicate), 0.4, 0.5, 0.6, and 0.7 seconds, while the R_2 measurements were performed using delay times of 4 (duplicate), 8, 16, 28, 36, 48 milliseconds. The coupling constants for all experiments were set to 185 Hz for the C6 atom. For each FID, an average of 64 scans and 1024 complex points were collected. The coupling constants for all experiments were set to 185 Hz for the uracil $^{13}C6$ atom. For each FID, an average of 64 scans and 1024 complex points were collected. The ^{1}H spectra were referenced to internal DSS while the ^{13}C dimension was referenced by multiplying the proton frequency at 0 ppm by the gyromagnetic ratio (γ) of ^{1}H to ^{13}C. The MATLAB program RELAXFIT was used for relaxation rate extraction and Monte-Carlo error estimation was made from duplicate delay times for R_1 experiment and R_2. From the R_1 and R_2 values obtained, corrected R_2 values were determined using the following equation 1 as used for the A-site rRNAs.

hNOE (TAR-2 RNA specific)

The hNOE experiment consisted of two replicates of saturated and unsaturated NMR experiments;

this was done to perform error analysis. To saturate the proton, a hard 180° pulse was applied. The saturated hNOE experiments used a saturation delay (D35) of 5s. The unsaturated hNOE, used a delay (D9) of 6.5s was used. The NOE+1 values reported in Figure 7 were obtained using the equation 2 as used for the A-site rRNAs.

Table 1. R_1, R_2 and hNOE +1 (Spin relaxation) rates of ^{13}C nuclear spins of A1492 and A1493 (P = Prokaryotic; E = Eukaryotic)

Residue	R_1 (s^{-1})	Error	R_2 (s^{-1})	Error	hNOE (s^{-1})	Error
P. 1492	1.91	0.04	27.81	0.68	1.19	0.01
P. 1493	2.08	0.04	23.51	0.72	1.28	0.00
E. 1492	1.89	0.00	43.00	3.21	1.16	0.00
E. 1493	1.95	0.00	31.93	2.34	1.21	0.01

Table 2. R_1, R_2 and hNOE +1 values for TAR RNA (Spin relaxation) rates of the uracils

Residue	R_1 (s^{-1})	Error	R_2 (s^{-1})	Error	hNOE (s^{-1})	Error
U40	1.8	0.08	48.48	2.95	1.11	0.02
U42	1.7	0.08	46.36	4.05	1.11	0.00
U38	1.8	0.11	46.84	5.23	1.11	0.01
U31	2.4	0.10	31.95	2.62	1.35	0.01
U23	2.5	0.08	31.49	2.21	1.28	0.00
U25	2.5	0.09	25.45	2.01	1.35	0.00

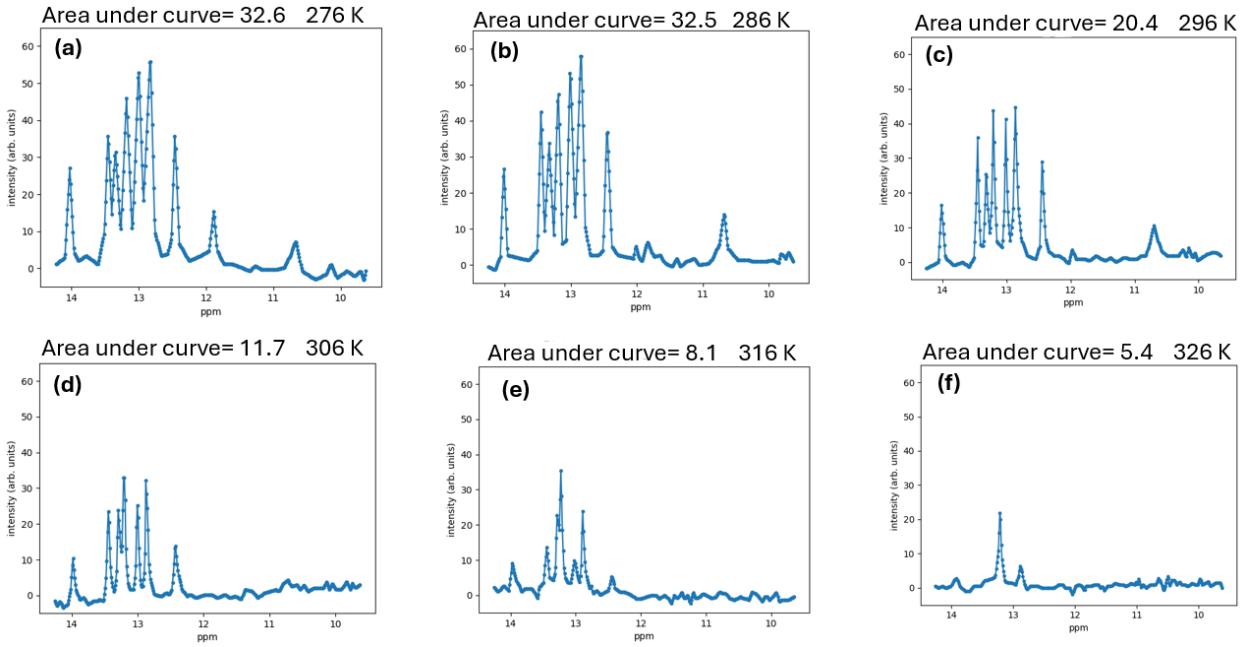

Appendix Figure 1 (a-f). The imino melt area under curve calculations for the prokaryotic rRNA A-site**.** The plots show the general reconstructions of the NMR spectra coded in python to receive a total area under all peaks. The code extracts each trace by using a small number of user-selected guide points and automatically interpolating all intermediate values along the curve. After calibrating the x-axis from pixel space to ppm, it converts the traced intensity profile into numerical arrays and integrates them using the trapezoidal rule. The script then processes all traces in the image, compiles their calibrated data, and exports both the raw traces and the calculated areas into an Excel file. The data shows a decrease in as bonds break in the presence of heat. An overall 83% decrease in peak area can be noted. Comparably, the prokaryotic sequence is more stable than the eukaryotic sequence.

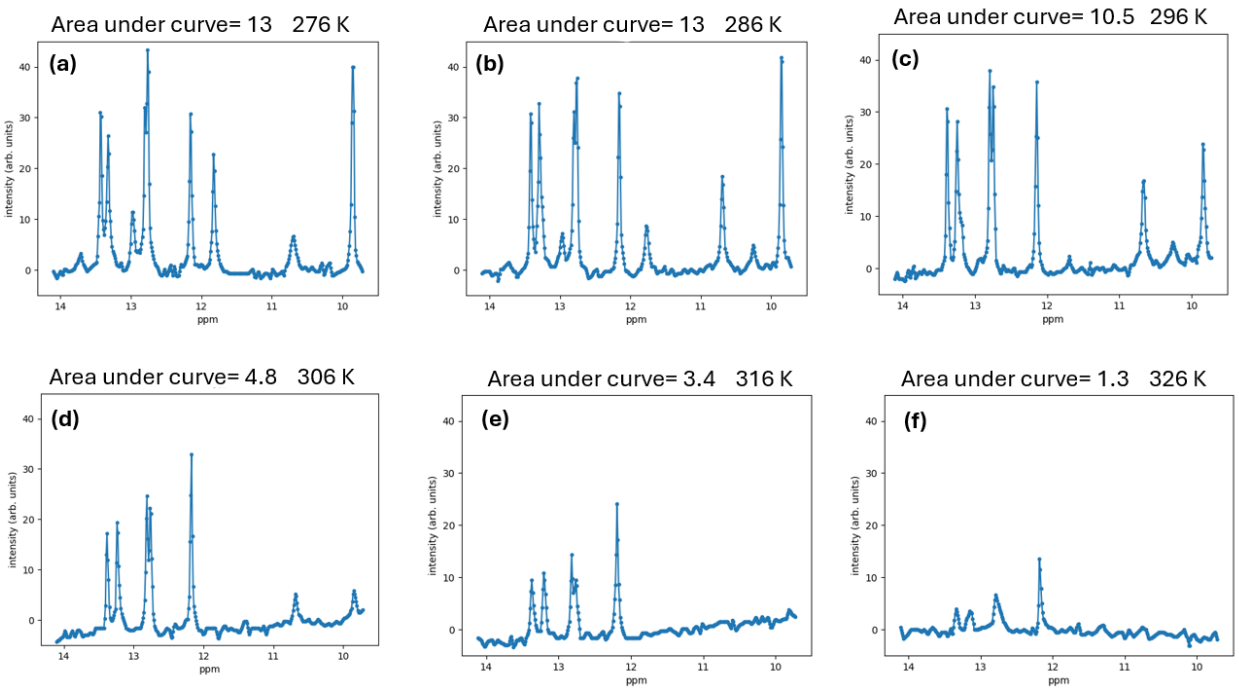

Appendix Figure 2 (a-f). The imino melt area under curve calculations for the eukaryotic rRNA A-site**.** The plots show the general reconstructions of the NMR spectra coded in python to receive a total area under all peaks. The code extracts each trace by using a small number of user-selected guide points and automatically interpolating all intermediate values along the curve. After calibrating the x-axis from pixel space to ppm, it converts the traced intensity profile into numerical arrays and integrates them using the trapezoidal rule. The script then processes all traces in the image and compiles their calibrated data. The data shows a decrease in area as bonds break in the presence of heat. An overall 90% decrease in peak area can be noted. Comparably, the eukaryotic sequence is less stable than the eukaryotic sequence. Python code is seen below .

```
import numpy as np
import matplotlib.pyplot as plt
from PIL import Image
import pandas as pd

# ---------- helper functions ----------

def calibrate_x_axis(img):
    """
    Click 14 ppm tick (left) then 10 ppm tick (right).
    Returns slope, intercept so that:
```

```
    ppm = slope * x_pixel + intercept
    """
    fig, ax = plt.subplots()
    ax.imshow(img)
    ax.set_title("Click 14 ppm tick, then 10 ppm tick on the x-axis")
    pts = np.array(plt.ginput(2, timeout=-1))
    plt.close(fig)

    x1, x2 = pts[:, 0]
    ppm1, ppm2 = 14.0, 10.0

    slope = (ppm2 - ppm1) / (x2 - x1)
    intercept = ppm1 - slope * x1
    return slope, intercept


def digitize_trace(img, slope, intercept, label, n_dense=400):
    """
    Digitize one trace with sparse clicks and interpolate between them.

    Steps:
      1) Click two baseline points for that temperature.
      2) Click ~10–30 guide points along the trace with left click.
         Right or middle click to finish.
      3) The function interpolates between x,y guide points to create
         a dense curve, converts to ppm and intensity, and integrates.

    Returns:
        x_ppm (np.ndarray), intens (np.ndarray), area (float)
    """
    # ---- baseline selection ----
    fig, ax = plt.subplots()
    ax.imshow(img)
    ax.set_title(f"{label}: Click TWO baseline points near this trace")
    base_pts = np.array(plt.ginput(2, timeout=-1))
    plt.close(fig)

    baseline_y = base_pts[:, 1].mean()

    # ---- sparse guide points ----
    fig, ax = plt.subplots()
    ax.imshow(img)
    ax.set_title(
        f"{label}: Click guide points along the trace (left click).\n"
        "Right or middle click when finished."
    )
    pts = np.array(plt.ginput(-1, timeout=-1))
    plt.close(fig)

    if len(pts) < 2:
        raise ValueError(f"Not enough points selected for {label}.")

    # sort by x so the curve is single valued in x
    order = np.argsort(pts[:, 0])
    x_click = pts[order, 0]
```

```
    y_click = pts[order, 1]

    # dense interpolation in pixel space
    x_pix_dense = np.linspace(x_click[0], x_click[-1], n_dense)
    y_pix_dense = np.interp(x_pix_dense, x_click, y_click)

    # convert x pixels → ppm
    x_ppm = slope * x_pix_dense + intercept

    # convert y pixels → intensity (baseline_y - y, so peaks are positive)
    intens = baseline_y - y_pix_dense

    # trapezoidal integration over the whole digitized region
    area = np.trapz(intens, x_ppm)

    # quick check plot
    fig, ax = plt.subplots()
    ax.plot(x_ppm, intens, marker='.')
    ax.set_xlabel("ppm")
    ax.set_ylabel("intensity (arb. units)")
    ax.set_title(f"Digitized trace (interpolated): {label}\nArea = {area:.3g}")
    ax.invert_xaxis()
    plt.show()

    return x_ppm, intens, area


# ---------- main script ----------

def main():
    # 1) load your PNG
    img_path = r"C:\Users\rdani\Downloads\NMR Images\Human\Human NMR Melt.png"
    img = np.array(Image.open(img_path))

    # 2) calibrate x-axis once
    slope, intercept = calibrate_x_axis(img)

    # 3) list all traces you want to digitize (top to bottom or whatever order you prefer)
    labels = ["276 K", "286 K", "296 K", "306 K", "316 K", "326 K"]

    traces = {}
    areas = {}

    for lab in labels:
        x_ppm, intens, area = digitize_trace(img, slope, intercept, lab, n_dense=400)
        traces[lab] = (x_ppm, intens)
        areas[lab] = area
        print(f"{lab}: area = {area:.6g}")

    # ratio examples
    if "306 K" in areas and "316 K" in areas:
        a306 = areas["306 K"]
        a316 = areas["316 K"]
        if a306 != 0:
            print(f"316 K / 306 K area ratio: {a316 / a306:.3f}")
```

```
    # 4) save everything to Excel
    out_path = "digitized_traces_all_temps.xlsx"
    with pd.ExcelWriter(out_path) as writer:
        # one sheet per trace
        for lab in labels:
            x_ppm, intens = traces[lab]
            df = pd.DataFrame({"ppm": x_ppm, "intensity": intens})
            # Excel sheet names can not contain ":" so strip or replace
            sheet_name = lab.replace(":", "_")
            df.to_excel(writer, sheet_name=sheet_name, index=False)

        # summary sheet
        df_summary = pd.DataFrame(
            {
                "Label": labels,
                "Area": [areas[lab] for lab in labels],
            }
        )
        writer.sheets  # force writer to be created
        df_summary.to_excel(writer, sheet_name="Summary", index=False)

    print(f"All digitized traces written to {out_path}")


if __name__ == "__main__":
    main()
```

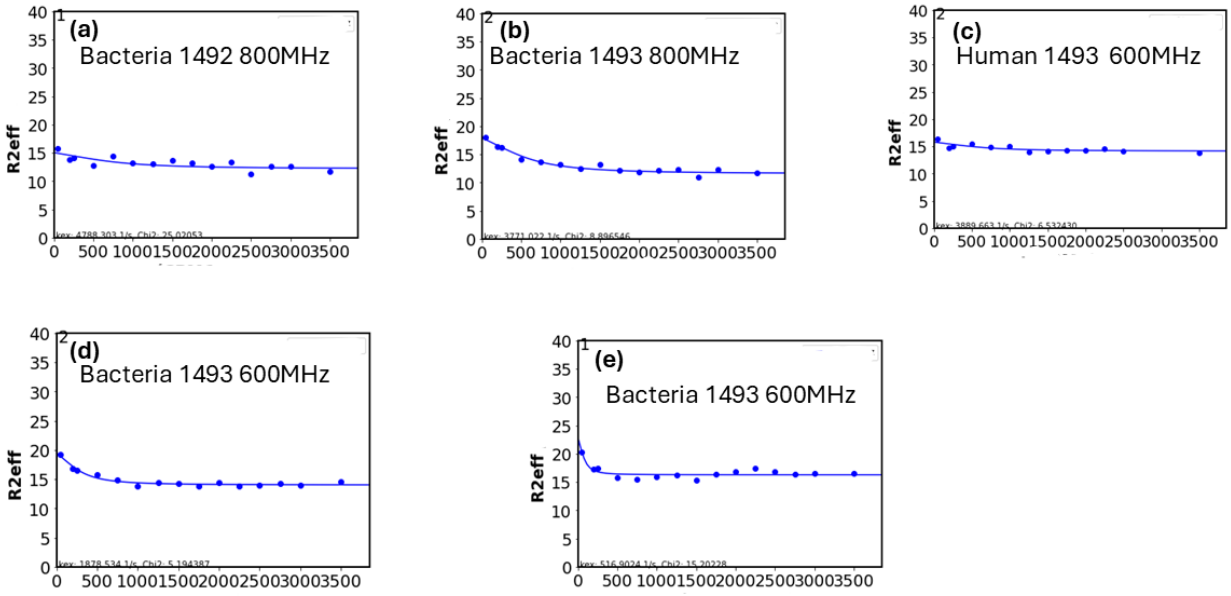

Appendix Figure 3 (a-e). The curves produced by NESSY that correspond to the results detailed in the main text. **(a, b, d and e)** represent data from the bacteria rRNA sequence and **(c)** is from the human rRNA sequence

NESSY analyzed the CPMG data by taking the manually entered $R_{2,\text{eff}}$ from each $\nu_{\text{CPMG}}$and attempted to fit them to many different exchange models. These models ranged from no exchange to more complex multi-parameter exchange models. As an initial reference, NESSY will test a no-exchange model where the $R_{2,\text{eff}}$is independent of refocusing frequency. This is seen below.

$$R_{2,\text{eff}}(\nu_{\text{CPMG}}) = R_2^0.$$

Then, NESSY evaluated other exchange models. NESSY begins with the two-site Carver–Richards model, which accounts for exchange contributions through the equation seen below

$$R_{2,\text{eff}}(\nu_{\text{CPMG}}) = R_2^0 + R_{\text{ex}}(\nu_{\text{CPMG}}),$$

where the analytical exchange term is seen below

$$R_{\text{ex}}(\nu_{\text{CPMG}}) = \frac{p_A p_B \, \Delta\omega^2 \, k_{\text{ex}}}{k_{\text{ex}}^2 + (\pi \nu_{\text{CPMG}})^2}.$$

Additionally, NESSY In addition to testing two-state models, NESSY can test for 3-state slow, fast and intermediate exchange. For every candidate model, NESSY optimized all parameters by looking for the lowest root-mean-square deviation between the predicted and experimental $R_{2,\text{eff}}$values. NESSY then computed the Akaike Information Criterion (AIC), which penalizes unnecessary parameters to prevent any over-fitting. NESSY compares AIC across all the available models (3-state slow, fast and intermediate exchange) for fitting. Then, NESSY selects the statistically best-supported model for each residue based on those factors.

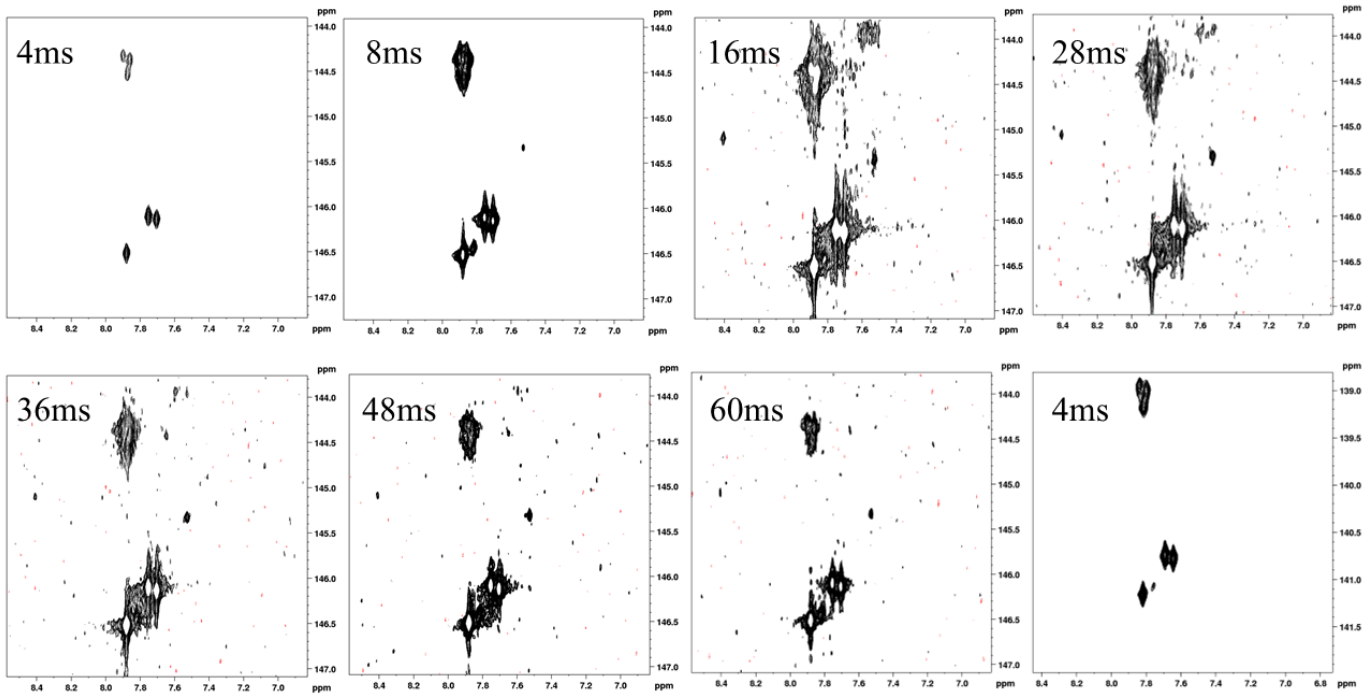

Appendix Figure 4. The NMR files from a T_1 ^{1}H- ^{13}C experiment using the TAR-2 construct. Uracil is labeled with a ^{13}C isotope on 6-position and deuteration on the 5-position of the nucleobase

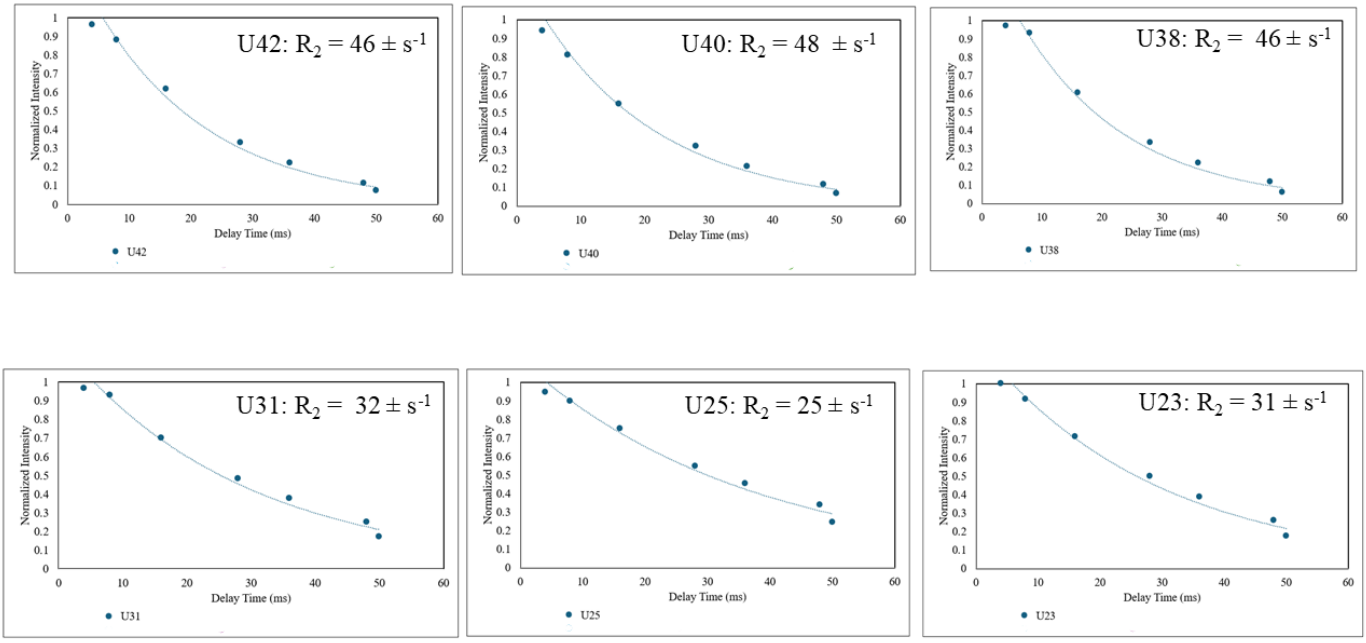

Appendix Figure 5. Analysis of the fit from a ^{1}H- ^{13}C R_2 experiment using the TAR-2 construct. Displayed are the transverse relaxation rate values adjusted by Matlab code 147-148. Uracil is labeled with a ^{13}C isotope on 6-position and deuteration on the 5-position of the nucleobase.

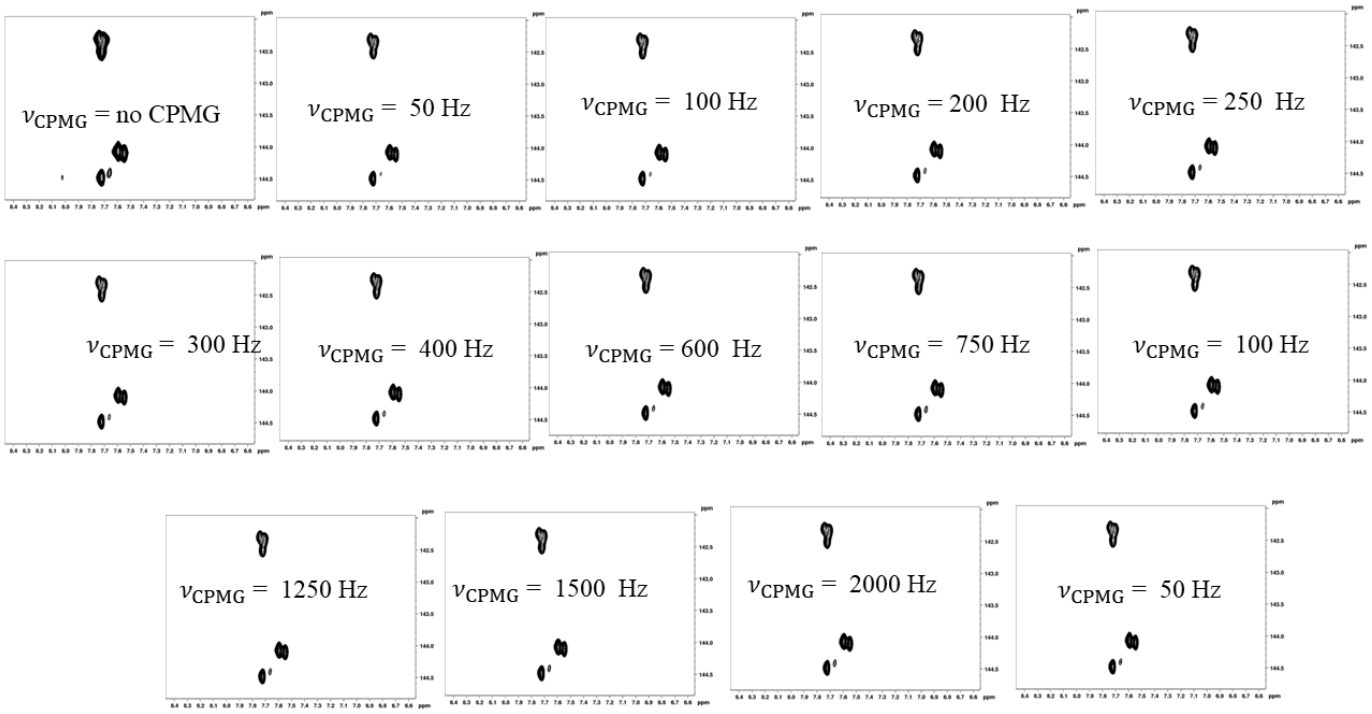

Appendix Figure 6. CPMG data from the TAR-2 mentioned in the text. Files depict intensity changes as an effect of various frequencies (displayed on each data file) applied. CPMG depits a ^{1}H- ^{13}C R_2 experiment. Uracil is labeled with a ^{13}C isotope on 6-position and deuteration on the 5-position of the nucleobase.

Experiment Type	NMR Spectrometer	Folder Name	Pulse Program
CPMG	NMR600 CP800 NMR600 CP800	241216_RO_RD_FS_TAR-2-BASE_CPMG 240202RitaRegan_Asite_Alabel_Base_CPMG 2023_07_16_CPMG-test Mary_SEL_ATP_HC_RNA_CPMG__BASE_9_14_20 Mary_1',5',8_13C_ATP_HC_RNA_Base_9_28_20	tkd_TROSY_HCP_1HCPMG.RML
hNOE	NMR600	Mary_1',5',8_13C_ATP_HC_RNA_11_7_19 (Expt 100) 250122_FPS_RD_RO_tar-2_Base+HNOE	TKD_13C_TrosyNOESat_NoDecSelt
R_1	NMR600	241031_FPS_RD_tar-2_Base_t1 Mary_1',8_13C_ATP_HC_RNA_11_15_19	13C_TD_T1_ALH 10ms_3D_HN
R_2	NMR600	241114_RD_FS_TAR-2_Base_HSQC_T1rho Mary_1',8_13C_ATP_HC_RNA_11_15_19_New	Hsqctretf2gpsi3d

Bibliography

1.Fleming, A. On the Antibacterial Action of Cultures of a Penicillium, with Special Reference to Their Use in the Isolation of B. Influenzae. *Rev. Infect. Dis.* **1980**, *2* (1), 129–139.

2.Bartlett, J. G.; Gilbert, D. N.; Spellberg, B. Seven Ways to Preserve the Miracle of Antibiotics. *IDSA.* **2013**, *56* (10), 1445–1450.

3.Spellberg, B.; Gilbert, D. N. The Future of Antibiotics and Resistance: A Tribute to a Career of Leadership by John Bartlett. *Clin. Infect. Dis.* **2014**, *59* (suppl 2), S71–S75.

4.Fleming, A. Nobel Lecture, December 11, 1945.

5.Naghavi, M.; Vollset, S. E.; Ikuta, K. S.; Swetschinski, L. R.; Gray, A. P.; Wool, E. E.; Robles Aguilar, G.; Mestrovic, T.; Smith, G.; Han, C.; Hsu, R. L.; Chalek, J.; Araki, D. T.; Chung, E.; Raggi, C.; Gershberg Hayoon, A.; Davis Weaver, N.; Lindstedt, P. A.; Smith, A. E.; Altay, U. Global Burden of Bacterial Antimicrobial Resistance 1990–2021: A Systematic Analysis with Forecasts to 2050. *Lancet Neorl.* **2024**, *404* (10459), 1199–1226.

6.World Health Organization. *Global Antimicrobial Resistance and Use Surveillance System (GLASS)* Report **2022**.

7.Taiwo, K. M. Screening for Potential Antibacterial Agents and the Application of Isotopic Labels for the Characterization of their Effects on the Dynamics of the Bacterial 16S Ribosomal RNA. Philosopher's Doctorate Dissertation, University of Maryland College Park, **2022**.

8.Reygaert, W. C. An Overview of the Antimicrobial Resistance Mechanisms of Bacteria. *AIMS Microbiol.* **2018**, *4* (3), 482–501.

9.Kapoor, G.; Saigal, S.; Elongavan, A. Action and Resistance Mechanisms of Antibiotics: A Guide for Clinicians. *J. Anaesthesiol. Clin. Pharmaco.* **2017**, *33* (3), 300–305.

10.Kumar, A.; Schweizer, H. Bacterial Resistance to Antibiotics: Active Efflux and Reduced Uptake. *Adv. Drug Deliv. Rev.* **2005**, *57* (10), 1486–1513.

11.Blair, J. M.; Richmond, G. E.; Piddock, L. J. Multidrug Efflux Pumps in Gram-Negative Bacteria and Their Role in Antibiotic Resistance. *Future Microbiol.* **2014**, *9* (10), 1165-77.

12.Mah, T.-F. Biofilm-Specific Antibiotic Resistance. *Future Microbiol.* **2012**, *7* (9), 1061–1072.

13.Uddin, T. M.; Chakraborty, A. J.; Khusro, A.; Zidan, B. R. M.; Mitra, S.; Emran, T. B.; Dhama, K.; Ripon, Md. K. H.; Gajdács, M.; Sahibzada, M. U. K.; Hossain, Md. J.; Koirala, N. Antibiotic Resistance in Microbes: History, Mechanisms, Therapeutic Strategies and Future Prospects. *J. Infect. Public Health.* **2021**, *14* (12), 1750–1766.

14.Lee, P.; Chu, C.; Tsai, Y.; Chuang, Y.; Lung, F. Design, Synthesis, and Antimicrobial Activities of Novel Functional Peptides against Gram-Positive and Gram-Negative Bacteria. *Chem Biol Drug Des*. **2019**, *94* (2), 1537–1544.

15.Sabath, L. D. Mechanisms of Resistance to Beta-Lactam Antibiotics in Strains of Staphylococcus Aureus. *Ann Intern Med*. **1982**, *97* (3), 339.

16.Wilke, M. S.; Lovering, A. L.; Strynadka, N. C. β-Lactam Antibiotic Resistance: A Current Structural Perspective. *Curr Opin Microbiol*. **2005**, *8* (5), 525–533.

17.Eiamphungporn, W.; Schaduangrat, N.; Malik, A.; Nantasenamat, C. Tackling the Antibiotic Resistance Caused by Class a β-Lactamases through the Use of β-Lactamase Inhibitory Protein. *Int. J. Mol. Sci.* **2018**, *19* (8), 2222.

18.Boucher, H. W.; Talbot, G. H.; Bradley, J. S.; Edwards, J. E.; Gilbert, D.; Rice, L. B.; Scheld, M.; Spellberg, B.; Bartlett, J. Bad Bugs, No Drugs: No ESKAPE! An Update from the Infectious Diseases Society of America. *Clin. Infect. Dis.* **2009**, *48* (1), 1–12.

19.Batey, R.; Rambo, R.; Doudna, J. *Tertiary Motifs in RNA Structure and Folding*. *Angew. Chem. Int. Ed. Engl.* **1999,** *38* (16), 2326-2343

20.Hong, W.; Zeng, J.; Xie, J. Antibiotic Drugs Targeting Bacterial RNAs. *Acta Pharm. Sin. B.* **2014**, *4* (4), 258–265.

21.Fourmy, D.; Yoshizawa, S.; Puglisi, J. D. Paromomycin Binding Induces a Local Conformational Change in the A-Site of 16 S rRNA. *J. Mol. Biol.* **1998**, *277* (2), 333–345.

22.Davies, J.; Gilbert, W.; Gorini, L. Streptomycin, suppression, and the code. *PNAS.* **1964**, *51* (5), 883–890.

23.Rivera, J. A.; Larsson, J.; Volkov, I. L.; Seefeldt, A. C.; Sanyal, S.; Johansson, M. Real-Time Measurements of Aminoglycoside Effects on Protein Synthesis in Live Cells. *PNAS.* **2021**, *118*

(9) e2013315118.

24.Kohanski, M. A.; Dwyer, D. J.; Wierzbowski, J.; Cottarel, G.; Collins, J. J. Mistranslation of Membrane Proteins and Two-Component System Activation Trigger Antibiotic-Mediated Cell Death. *Cell* **2008**, *135* (4), 679–690.

25.Tissieres, A.; Schlessinger, D.; Gros, F. Amino Acid Incorporation into Proteins by *Escherichia coli* Ribosomes. *PNAS.* **1960**, *46* (11), 1450–1463.

26.Warner, J. R.; Rich, A. The Number of Soluble RNA Molecules on Reticulocyte Polyribosomes. *PNAS.* **1964,** *51* (6), 1134-1141.

27.Inês Moranguinho; Taveira, N.; Inês Bártolo. Antiretroviral Treatment of HIV-2 Infection: Available Drugs, Resistance Pathways, and Promising New Compounds. *IJMS.* **2023**, *24* (6), 5905–5905.

28.Shah, S. S.; Fine, S. M.; Vail, R. M.; McGowan, J. P.; Merrick, S. T.; Radix, A. E.; Hoffmann, C. J.; Gonzalez, C. J. *Diagnosis and Management of HIV-2 in Adults*; Johns Hopkins University: Baltimore (MD) **2022**.

29.Shabalala, F. S.; Vernooij, E.; Pell, C.; Simelane, N.; Masilela, N.; Spiegelman, D.; Chai, B.; Khan, S.; Reis, R. Understanding Reasons for Discontinued Antiretroviral Treatment among Clients in Test and Treat: A Qualitative Study in Swaziland. *J. Int. AIDS Soc.* **2018**, *21*, e25120.

30.Marcus, U.; Hickson, F.; Weatherburn, P.; Furegato, M.; Breveglieri, M.; Berg, R. C.; Schmidt, A. J. Antiretroviral Therapy and Reasons for Not Taking It among Men Having Sex with Men (MSM)—Results from the European MSM Internet Survey (EMIS). *PLoS ONE* **2015**, *10* (3), e0121047.

31.Bertrand, J., Barrail-Tran, A., Fayette, L., Savic, R., Goujard, C., Teicher, E., Barau, C., Pruvost, A., Taburet, A. M., Mentré, F., & Verstuyft, C. Pharmacokinetic Model of Tenofovir and Emtricitabine and Their Intracellular Metabolites in Patients in the ANRS 134-COPHAR 3 Trial Using Dose Records. *Antimicrob. Agents Chemother.* **2023**, *67* (5), e0233918.

32.Singh, A. K.; Kumar, A.; Arora, S.; Kumar, R.; Verma, A.; Khalilullah, H.; Jaremko, M.; Emwas, A.-H.; Kumar, P. Current Insights and Molecular Docking Studies of HIV-1 Reverse Transcriptase Inhibitors. *Chem Biol Drug Des.* **2023**, *103* (1), e14372.

33.Temin, H. M.; Mizutani, S. Viral RNA-Dependent DNA Polymerase: RNA-Dependent DNA

Polymerase in Virions of Rous Sarcoma Virus. *Nat.* **1970**, *226* (5252), 1211–1213.

34. Mitsuya, H.; Weinhold, K. J.; Furman, P. A.; St Clair, M. H.; Lehrman, S. N.; Gallo, R. C.; Bolognesi, D.; Barry, D. W.; Broder, S. 3'-Azido-3'-Deoxythymidine (BW A509U): An Antiviral Agent That Inhibits the Infectivity and Cytopathic Effect of Human T-Lymphotropic Virus Type III/Lymphadenopathy-Associated Virus *in Vitro*. *PNAS.* **1985**, *82* (20), 7096–7100.

35. Cramer, P.; Bushnell, D. A.; Kornberg, R. D. Structural Basis of Transcription: RNA Polymerase II at 2.8 Ångstrom Resolution. *Sci.* **2001**, *292* (5523), 1863–1876.

36. Saag, M. S.; Benson, C. A.; Gandhi, R. T.; Hoy, J. F.; Landovitz, R. J.; Mugavero, M. J.; Sax, P. E.; Smith, D. M.; Thompson, M. A.; Buchbinder, S. P.; Rio, C. del; Eron, J. J.; Fätkenheuer, G.; Günthard, H. F.; Molina, J.-M.; Jacobsen, D. M.; Volberding, P. A. Antiretroviral Drugs for Treatment and Prevention of HIV Infection in Adults: 2018 Recommendations of the International Antiviral Society–USA Panel. *JAMA.* **2018**, *320* (4), 379–396.

37. Nunberg J. H., Schleif W. A., Boots E. J., O'Brien J. A., Quintero J. C., Hoffman J. M., Emini E. A., Goldman M. E. Viral resistance to human immunodeficiency virus type 1-specific pyridinone reverse transcriptase inhibitors**.** *J. Virol.* **1991**, *65* (9):4887–4892.

38. Kohl, N. E.; Emini, E. A.; Schleif, W. A.; Davis, L. J.; Heimbach, J. C.; Dixon, R. A.; Scolnick, E. M.; Sigal, I. S. Active Human Immunodeficiency Virus Protease Is Required for Viral Infectivity. *PNAS.* **1988**, *85* (13), 4686–4690.

39. Hilton, B. J., & Wolkowicz, R. An assay to monitor HIV-1 protease activity for the identification of novel inhibitors in T-cells. *PloS one* **2010**, *5* (6), e10940.

40. Venkatachalam, S.; Krishnan, S. R.; Sayed, Y.; M Michael Gromiha. Structural and Functional Studies on HIV Protease: Mechanism of Action, Subtypes, Inhibitors, and Drug Resistance. *Methods Mol. Biol.* **2024,** *2867* 185–200.

41. Smith JS, Roth MJ. Purification and characterization of an active human immunodeficiency virus type 1 RNase H domain. *J. Virol.* **1993** *67* (7) 4037-4049.

42. Das, D. HIV-1 protease inhibitors and mechanisms of HIV-1's resistance. *J. glob. health med.* **2024,** *6* (6), 357–362.

*43.*Checkley, M. A., Luttge, B. G., & Freed, E. O. HIV-1 envelope glycoprotein biosynthesis, trafficking, and incorporation. *J. Mol. Biol.* **2022**, *410* (4), 582–608.

*44.*Liu, Z., Shan, M., Li, L., Lu, L., Meng, S., Chen, C., He, Y., Jiang, S., & Zhang, L. *In vitro* selection and characterization of HIV-1 variants with increased resistance to sifuvirtide, a novel HIV-1 fusion inhibitor, *J. Biol. Chem.* **2011**, 286 (5), 3277–3287.

45.Wu, L.; Paxton, W. A.; Kassam, N.; Ruffing, N.; Rottman, J. B.; Sullivan, N.; Choe, H.; Sodroski, J.; Newman, W.; Koup, R. A.; Mackay, C. R. CCR5 Levels and Expression Pattern Correlate with Infectability by Macrophage-Tropic HIV-1, *in Vitro*. *J. Exp. Med.* **1997**, *185* (9), 1681–1692.

46.Craigie, R. The Molecular Biology of HIV Integrase. *Future Virol.* **2012**, *7* (7), 679–686.

47.Pandey, K.; Grandgenett , D. HIV-1 Integrase Strand Transfer Inhibitors: Novel Insights into Their Mechanism of Action. *Int. j. radiol. radiat. ther.* **2008**, 11–16.

48.Bester, S. M.; Wei, G.; Zhao, H.; Adu-Ampratwum, D.; Iqbal, N.; Courouble, V. V.; Francis, A. C.; Annamalai, A. S.; Singh, P. K.; Shkriabai, N.; Blerkom, P. V.; Morrison, J.; Poeschla, E. M.; Engelman, A. N.; Melikyan, G. B.; Griffin, P. R.; Fuchs, J. R.; Asturias, F. J.; Kvaratskhelia, M. Structural and Mechanistic Bases for a Potent HIV-1 Capsid Inhibitor. *Sci.* **2020**, *370* (6514), 360–364.

49.Link, J. O.; Rhee, M. S.; Tse, W. C.; Zheng, J.; Somoza, J. R.; Rowe, W.; Begley, R.; Chiu, A.; Mulato, A.; Hansen, D.; Singer, E.; Tsai, L. K.; Bam, R. A.; Chou, C.-H.; Canales, E.; Brizgys, G.; Zhang, J. R.; Li, J.; Graupe, M.; Morganelli, P. Clinical Targeting of HIV Capsid Protein with a Long-Acting Small Molecule. *Nat.* **2020**, *584* (7822), 614–618.

50.Boyer, P. L.; Clark, P. K.; Hughes, S. H. HIV-1 and HIV-2 Reverse Transcriptases: Different Mechanisms of Resistance to Nucleoside Reverse Transcriptase Inhibitors. *J. Virol.* **2012**, *86* (10), 5885–5894.

51.Kuritzkes, D. R. Drug Resistance in HIV-1. *COVIRO.* **2011**, *1* (6), 582–589.

52.Karikó, K.; Buckstein, M.; Ni, H.; Weissman, D. Suppression of RNA Recognition by Toll-like Receptors: The Impact of Nucleoside Modification and the Evolutionary Origin of RNA. *Immunity* **2005**, *23* (2), 165–175.

53.Nelson, D. L.; Cox, M. M.; Hoskins, A. A. *Lehninger Principles of Biochemistry*, 8th ed.; W. H. Freeman: New York, 2021.

54.Nelson, D. L.; Cox, M. M.; Hoskins, A. A. *Lehninger Principles of Biochemistry*, 8th ed.; W. H. Freeman: New York, 2021; 1055–1057.

55.Collie, G. W.; Haider, S. M.; Neidle, S.; Parkinson, G. N. A Crystallographic and Modelling Study of a Human Telomeric RNA (TERRA) Quadruplex. *NAR.* **2010**, *38* (16), 5569–5580.

56.Shen, L.; Tinoco, I. The Structure of an RNA Pseudoknot That Causes Efficient Frameshifting in Mouse Mammary Tumor Virus. *J. Mol. Biol.* **1995**, *247* (5), 963–978.

57.Murray, J. B.; Meroueh, S. O.; Russell, R. J. M.; Georg Lentzen; Haddad, J.; Shahriar Mobashery. Interactions of Designer Antibiotics and the Bacterial Ribosomal Aminoacyl-TRNA Site. *Chem. Biol.* **2006**, *13* (2), 129–138.

58.Brown, J. A.; Bulkley, D.; Wang, J.; Valenstein, M. L.; Yario, T. A.; Steitz, T. A.; Steitz, J. A. Structural Insights into the Stabilization of MALAT1 Noncoding RNA by a Bipartite Triple Helix. *Nat. Struct. Mol. Biol.* **2014**, *21* (7), 633–640.

59.Bou-Nader, C.; Link, K. A.; Suddala, K. C.; Knutson, J. R.; Zhang, J. Structures of Complete HIV-1 TAR RNA Portray a Dynamic Platform Poised for Protein Binding and Structural Remodeling. *Nat Commun.* **2025**, *16* (1).

60.Dayie, K. T.; Brodsky, A. S.; Williamson, J. R. Base Flexibility in HIV-2 TAR RNA Mapped by Solution 15N, 13C NMR Relaxation. *J. Mol. Biol.* **2002**, *317* (2), 263–278.

61.Ebbe Sloth Andersen; Sonia Antoranz Contera; Knudsen, B.; Damgaard, C.; Flemming Besenbacher; Jørgen Kjems. Role of the Trans-Activation Response Element in Dimerization of HIV-1 RNA. *J. Biol. Chem.* **2004**, *279* (21), 22243–22249.

62.Giraldo-Ocampo, S.; Valiente-Echeverría, F.; Soto-Rifo, R. Host RNA-Binding Proteins as Regulators of HIV-1 Replication. *Viruses* **2024**, *17* (1), 43–43.

63.Brodsky, A. S.; Williamson, J. R. Solution Structure of the HIV-2 TAR-Argininamide Complex 1 1Edited by I. Tinoco. *J. Mol. Biol.* **1997**, *267* (3), 624–639.

64.Tao, J.; Frankel, A. D. Specific Binding of Arginine to TAR RNA. *PNAS.* **1992**, *89* (7), 2723–2726.

65.Yonath, A.; Leonard, K.; Wittmann, H. G. A Tunnel in the Large Ribosomal Subunit Revealed by

Three-Dimensional Image Reconstruction. *Sci.* **1987**, *236* (4803), 813–816.

66. Wimberly, B. T.; Brodersen, D. E.; Clemons, W. M.; Morgan-Warren, R. J.; Carter, A. P.; Vonrhein, C.; Hartsch, T.; Ramakrishnan, V. Structure of the 30S Ribosomal Subunit. *Nat.* **2000**, *407* (6802), 327–339.

67. Kelly, M. L.; Roy, R.; Geng, A.; Ganser, L. R.; Akanksha Manghrani; Cullen, B. R.; Schulze-Gahmen, U.; Herschlag, D.; Al-Hashimi, H. M. RNA Conformational Propensities Determine Cellular Activity. *Nat.* **2023**, *617* (7962), 835–841.

68. Paunovska, K.; Loughrey, D.; Dahlman, J. E. Drug Delivery Systems for RNA Therapeutics. *Nat. Rev. Genet.* **2022**, *23* (5) 265–280.

69. Phei Er Saw; Song, E. Advancements in Clinical RNA Therapeutics: Present Developments and Prospective Outlooks. *Cell Rep. Med.* **2024**, *5* (5), 101555–101555.

70. Li, X.; Bhullar, A. S.; Binzel, D. W.; Guo, P. The Dynamic, Motile and Deformative Properties of RNA Nanoparticles Facilitate the Third Milestone of Drug Development. *Adv. Drug Deliv. Rev.* **2022**, *186*, 114316.

71. Bush, J. A.; Williams, C. C.; Meyer, S. M.; Tong, Y.; Haniff, H. S.; Childs-Disney, J. L.; Disney, M. D. Systematically Studying the Effect of Small Molecules Interacting with RNA in Cellular and Preclinical Models. *ACS Chem. Biol.* **2021**, *16* (7), 1111–1127.

72. Bernal, J. D.; Crowfoot, D. X-Ray Photographs of Crystalline Pepsin. *Nat.* **1934**, *133* (3369), 794–795.

73. Kendrew, J. C.; Bodo, G.; Dintzis, H. M.; Parrish, R. G.; Wyckoff, H.; Phillips, D. C. A Three-Dimensional Model of the Myoglobin Molecule Obtained by X-Ray Analysis. *Nat.* **1958**, *181* (4610), 662–666.

74. Perutz, M. F.; Rossmann, M. G.; Cullis, A. F.; Muirhead, H.; Will, G.; North, A. C. T. *Structure of haemoglobin: a three-dimensional Fourier synthesis at 5.5-Å resolution, obtained by X-ray analysis*. *Nat.* **1960,** *185* (4711), 416-22.

75. Polson, A. G.; Crain, P. F.; Pomerantz, S. C.; McCloskey, J. A.; Bass, B. L. The Mechanism of Adenosine to Inosine Conversion by the Double-Stranded RNA Unwinding/Modifying Activity: A High-Performance Liquid Chromatography-Mass Spectrometry Analysis. *Biochem.* **1991**, *30* (49),

11507–11514.

76.X-ray Crystallography of RNA Adrian R. Ferré-D'Amaré In: RNA Structure and Folding, Meth *Methods Mol Biol*. **2017,** 319–348.

77.Stagno, J. R.; Bhandari, Y. R.; Conrad, C. E.; Liu, Y.; Wang, Y. Real-Time Crystallographic Studies of the Adenine Riboswitch Using an X-Ray Free-Electron Laser. *FEBS.* **2017**, *284* (20), 3374–3380.

78.Hengesbach, M.; Andrei Kobitski; Voigts-Hoffmann, F.; Frauer, C.; Nienhaus, G. U.; Helm, M. RNA Intramolecular Dynamics by Single-Molecule FRET. *Curr. Protoc. Nucleic Acid Chem.* **2008**, *34* (1) e11.

79.Zhuang, X.; Bartley, L. E.; Babcock, H. P.; Russell, R.; Ha, T.; Herschlag, D.; Chu, S. A Single-Molecule Study of RNA Catalysis and Folding. *Sci.* **2000**, *288* (5473), 2048–2051.

80.Helm, M.; Kobitski, A. Y.; Nienhaus, G. U. Single-Molecule Förster Resonance Energy Transfer Studies of RNA Structure, Dynamics and Function. *Biophys. Rev.* **2009**, *1* (4), 161–176.

81.Rambo, R. P.; Tainer, J. A. Accurate Assessment of Mass, Models and Resolution by Small-Angle Scattering. *Nat.* **2013**, *496* (7446), 477–481.

82.Chen, X.; Wang, L.; Xie, J.; Nowak, J. S.; Luo, B.; Zhang, C.; Jia, G.; Zou, J.; Huang, D.; Glatt, S.; Yang, Y.; Su, Z. RNA Sample Optimization for Cryo-EM Analysis. *Nat. Protoc.* **2024**.

83.Dethoff, E. A.; Chugh, J.; Mustoe, A. M.; Al-Hashimi, H. M. Functional Complexity and Regulation through RNA Dynamics. *Nat.* **2012**, *482* (7385), 322–330.

84.Ganser, L. R.; Kelly, M. L.; Herschlag, D.; Al-Hashimi, H. M. The Roles of Structural Dynamics in the Cellular Functions of RNAs. *Nat. Rev. Mol. Cell Biol.* **2019**, *20* (8), 474–489.

85.Fürtig, B.; Richter, C.; Wöhnert, J.; Schwalbe, H. NMR Spectroscopy of RNA. *ChemBioChem.* **2003**, *4* (10), 936–962.

86.Jackson, R. W.; Smathers, C. M.; Robart, A. R. General Strategies for RNA X-Ray Crystallography. *Mol.* **2023**, *28* (5), 2111–2111.

87.Eshel Faraggi; A Keith Dunker; Sussman, J. L.; Andrzej Kloczkowski. Comparing NMR and X-Ray Protein Structure: Lindemann-like Parameters and NMR Disorder. *J. Biomol Struct Dyn.* **2017**, *36* (9), 2331–2341.

88.Pielak, G. J.; Li, C.; Miklos, A. C.; Schlesinger, A. P.; Slade, K. M.; Gui Fang Wang; Zigoneanu, I. G. Protein Nuclear Magnetic Resonance under Physiological Conditions. *Biochem.* **2008**, *48* (2), 226–234.

89.Lu, K., Miyazaki, Y., & Summers, M. F. Isotope labeling strategies for NMR studies of RNA. *J. Biomol. NMR.* **2010**, *46* (1), 113–125.

90.Al-Hashimi, H. M. Dynamics-Based Amplification of RNA Function and Its Characterization by Using NMR Spectroscopy. *ChemBioChem*. **2005**, *6* (9), 1506–1519.

91.Marušič, M.; Schlagnitweit, J.; Petzold, K. RNA Dynamics by NMR Spectroscopy. *ChemBioChem.* **2019**, *20* (21), 2685–2710.

92.Milligan, J. F.; Uhlenbeck, O. C. [5] Synthesis of Small RNAs Using T7 RNA Polymerase. *Methods Enzymol.* **1989**, *180*, 51–62.

93.Becette, O.; Olenginski, L. T.; Dayie, T. K. Solid-Phase Chemical Synthesis of Stable Isotope-Labeled RNA to Aid Structure and Dynamics Studies by NMR Spectroscopy. *Mol.* **2019**, *24* (19), 3476.

94.Nelissen, F. H. T.; van Gammeren, A. J.; Tessari, M.; Girard, F. C.; Heus, H. A.; Wijmenga, S. S. Multiple Segmental and Selective Isotope Labeling of Large RNA for NMR Structural Studies. *NAR*. **2008**, *36* (14), e89–e89.

95.Feyrer, H.; Cenk Onur Gurdap; Maja Marušič; Schlagnitweit, J.; Petzold, K. Enzymatic Incorporation of an Isotope-Labeled Adenine into RNA for the Study of Conformational Dynamics by NMR. *PLoS ONE* **2022**, *17* (7), e0264662–e0264662.

96.Thakur, C. S.; Luo, Y.; Chen, B.; Eldho, N. V.; T. Kwaku Dayie. Biomass Production of Site Selective 13C/15N Nucleotides Using Wild Type and a Transketolase E. Coli Mutant for Labeling RNA for High Resolution NMR. *J. Biomol. NMR.* **2011**, *52* (2), 103–114.

97.Nikonowicz, E. P.; Sirr, A.; Legault, P.; Jucker, F. M.; Baer, L. M.; Pardi, A. Preparation of ^{13}C and^{15}N Labelled RNAs for Heteronuclear Multi-Dimensional NMR Studies. *NAR*. **1992**, *20* (17), 4507–4513.

98.Batey, R. T.; Inada, M.; Kujawinski, E.; Puglisi, J. D.; Williamson, J. R. Preparation of Isotopically

Labeled Ribonucleotides for Multidimensional NMR Spectroscopy of RNA. *NAR.* **1992**, *20* (17), 4515–4523.

99. Haslecker, R.; Pham, V. V.; Glänzer, D.; Kreutz, C.; Dayie, T. K.; D'Souza, V. M. Extending the Toolbox for RNA Biology with SegModTeX: A Polymerase-Driven Method for Site-Specific and Segmental Labeling of RNA. *Nature commun.* **2023**, *14* (1), 8422.

100. LeBlanc, R. M.; Longhini, A. P.; Le Grice, S. F. J.; Johnson, B. A.; Dayie, T. K. Combining Asymmetric 13C-Labeling and Isotopic Filter/Edit NOESY: A Novel Strategy for Rapid and Logical RNA Resonance Assignment. *NAR.* **2017**, *45* (16), e146–e146.

101. Nam, H.; Becette, O.; LeBlanc, R. M.; Oh, D.; Case, D. A.; Dayie, T. K. Deleterious Effects of Carbon–Carbon Dipolar Coupling on RNA NMR Dynamics. *J. Biomol. NMR.* **2020**, *74* (6-7), 321–331.

102. Longhini, A. P.; LeBlanc, R. M.; Becette, O.; Salguero, C.; Wunderlich, C. H.; Johnson, B. A.; D'Souza, V. M.; Kreutz, C.; Dayie, T. K. Chemo-Enzymatic Synthesis of Site-Specific Isotopically Labeled Nucleotides for Use in NMR Resonance Assignment, Dynamics and Structural Characterizations. *NAR.* **2015**, *44* (6), e52–e52.

103. SantaLucia J., Shen L.X., Cai Z., Lewis H., Tinoco I. Synthesis and NMR of RNA with Selective isotopic enrichment in the bases. *NAR.* **1995**, *23,* 4913–4921.

104. Arthur, P. K.; Alvarado, L. J.; Dayie, T. K. Expression, Purification and Analysis of the Activity of Enzymes from the Pentose Phosphate Pathway. *Protein Expr. Purif*. **2011**, *76* (2), 229–237.

105. Taiwo, K. M.; Olenginski, L. T.; Nußbaumer, F.; Nam, H.; Hilber, S.; Kreutz, C.; Dayie, T. K. Synthesis of [7-15N]-GTPs for RNA Structure and Dynamics by NMR Spectroscopy. *Monatsh. Chem***. 2022**, *153* (3), 293–299.

106. Attionu, S. K.; Dill, R.; Summers, M. F.; Case, D. A.; Marchant, J.; Dayie, T. K. Selective [9-^{15}N] Guanosine for Nuclear Magnetic Resonance Studies of Large Ribonucleic Acids. *ChemBioChem.* **2025**, *26* (12).

107. Cavanagh, J.; Skelton, N. J.; Fairbrother, W. J.; Rance, M.; Palmer III, A. G. *Protein NMR Spectroscopy : Principles and Practice* **2007** 675–710.

108. Levitt, M. H. Appendix A: Properties of Selected Nuclei. In Spin Dynamics: Basics of Nuclear

Magnetic Resonance **2008,** 707–711.

109.Roy, R.; Hohng, S.; Ha, T. A Practical Guide to Single Molecule FRET. *Nat. methods* **2008**, *5* (6), 507–516.

110.Wijmenga, S. S.; van Buuren, B. N. M. The Use of NMR Methods for Conformational Studies of Nucleic Acids. *Prog. Nucl. Magn. Reson. Spectrosc.* **1998**, *32* (4), 287–387.

111.Barnwal, R. P.; Yang, F.; Varani, G. Applications of NMR to Structure Determination of RNAs Large and Small. *Arch. Biochem. Biophys.* **2017**, *628*, 42–56.

112.Nelson, D. L.; Cox, M. M. *Lehninger Principles of Biochemistry* **2013**, 1060–1066.

113.Krause, K. M.; Serio, A. W.; Kane, T. R.; Connolly, L. E. Aminoglycosides: An Overview. *CSH Perspect.* **2016**, *6* (6), a027029.

114.Tsai, A.; Uemura, S.; Johansson, M.; Puglisi, E. V.; Marshall, R. A.; Aitken, C. E.; Korlach, J.; Ehrenberg, M.; Puglisi, J. D. The Impact of Aminoglycosides on the Dynamics of Translation Elongation. *Cell Reports* **2013**, *3* (2), 497–508.

115.Noller, H. F. Ribosomal RNA and Translation. *Annu. Rev. Biochem.* **1991**, *60*, 191–227.

116.Gutell, R. R. Collection of Small Subunit (16S- and 16S-Like) Ribosomal RNA Structures. *NAR.* **1993**, *21* (13), 3051–3054.

117.Kondo, J.; François, B.; Alexandre Urzhumtsev; Westhof, E. Crystal Structure of the *Homo Sapiens* Cytoplasmic Ribosomal Decoding Site Complexed with Apramycin. *Angew. Chem.* **2006**, *45* (20), 3310–3314.

118.Ning, W.; Fei, J.; Gonzalez, R. L. The Ribosome Uses Cooperative Conformational Changes to Maximize and Regulate the Efficiency of Translation. *PNAS.* **2014**, *111* (33), 12073–12078.

119.Ryu, D. H.; Rando, R. R. Aminoglycoside Binding to Human and Bacterial A-Site RRNA Decoding Region Constructs. *Bioorg. Med. Chem.* **2001**, *9* (10), 2601–2608.

120.Lynch, S. R.; Puglisi, J. D. Structure of a Eukaryotic Decoding Region A-Site RNA. *J. Mol. Biol.* **2001**, *306* (5), 1023–1035.

121.Kondo, J.; Westhof, E. The Bacterial and Mitochondrial Ribosomal A-Site Molecular Switches Possess Different Conformational Substates. *NAR.* **2008**, *36* (8), 2654–2666.

122.Fourmy D, Recht MI, Puglisi JD. Binding of neomycin-class aminoglycoside antibiotics to the A-

site of 16 S rRNA. *J. Mol. Biol*. **1998**, *277* (2), 347-362.

123. Ogle, J. M.; Murphy, F. V.; Tarry, M. J.; Ramakrishnan, V. Selection of TRNA by the Ribosome Requires a Transition from an Open to a Closed Form. *Cell* **2002**, *111* (5), 721–732.

124. Ogle, J. M.; Carter, A. P.; Ramakrishnan, V. Insights into the Decoding Mechanism from Recent Ribosome Structures. *TiBS.* **2003**, *28* (5), 259–266.

125. Taiwo, K. M.; Becette, O. B.; Zong, G.; Chen, B.; Zavalij, P. Y.; T. Kwaku Dayie. Chemo-Enzymatic Synthesis of 13C- and 19F-Labeled Uridine-5′-Triphosphate for RNA NMR Probing. *Monatsh. Chem.* **2021**, *152* (4), 441–447.

126. Becette, O. B.; Zong, G.; Chen, B.; Taiwo, K. M.; Case, D. A.; Dayie, T. K. Solution NMR Readily Reveals Distinct Structural Folds and Interactions in Doubly^{13}C- and^{19}F-Labeled RNAs. *Sci. Adv.* **2020**, *6* (41) eabc6572.

127. Alvarado, L. J.; Longhini, A. P.; LeBlanc, R. M.; Chen, B.; Kreutz, C.; T. Kwaku Dayie. Chemo-Enzymatic Synthesis of Selectively 13C/15N-Labeled RNA for NMR Structural and Dynamics Studies. *Methods Enzymol.* **2014**, *549*, 133–162.

128. Chiarparin, E.; Rüdisser, S.; Bodenhausen, G. Hydrogen Bonds in RNA Base Pairs Investigated by Cross-Correlated Relaxation of Multiple-Quantum Coherence in NMR. *Chemphyschem.* **2001**, *2* (1), 41–45.

129. Nils-Alexander Lakomek; Kaufman, J. D.; Stahl, S. J.; Louis, J. M.; Grishaev, A.; Wingfield, P. T.; Bax, A. Internal Dynamics of the Homotrimeric HIV-1 Viral Coat Protein Gp41 on Multiple Time Scales. *Angew. Chem.* **2013**, *52* (14), 3911–3915.

130. Taiwo, K. M.; Nam, H.; LeBlanc, R. M.; Longhini, A. P.; Dayie, T. K. Cross-Correlated Relaxation Rates Provide Facile Exchange Signature in Selectively Labeled RNA. *J. Magn. Reson.* **2022**, *342*, 107245–107245.

131. Reiter, N. J.; Nikstad, L. J.; Allmann, A. M.; Johnson, R. J.; Butcher, S. E. Structure of the U6 RNA Intramolecular Stem–Loop Harboring an S_P-Phosphorothioate Modification. *RNA.* **2003**, *9* (5), 533–542.

132. Luteran, E. M.; Kahn, J. D.; Paukstelis, P. J. Stability of the PH-Dependent Parallel-Stranded D(CGA) Motif. *Biophys. J.* **2020**, *119* (8), 1580–1589.

133. Wunderlich, C. H.; Spitzer, R.; Santner, T.; Katja Fauster; Tollinger, M.; Kreutz, C. Synthesis of (6-^{13}C) Pyrimidine Nucleotides as Spin-Labels for RNA Dynamics. *JACS.* **2012**, *134* (17), 7558–7569.

134. LeBlanc, R. M.; Longhini, A. P.; Tugarinov, V.; Dayie, T. K. NMR Probing of Invisible Excited States Using Selectively Labeled RNAs. *J. Biomol. NMR.* **2018**, *71* (3), 165–172.

135. Merriman, D. K.; Xue, Y.; Yang, S.; Kimsey, I. J.; Shakya, A.; Clay, M.; Al-Hashimi, H. M. Shortening the HIV-1 TAR RNA Bulge by a Single Nucleotide Preserves Motional Modes over a Broad Range of Time Scales. *Biochem.* **2016**, *55* (32), 4445–4456.

136. Ceccarelli, G.; Giovanetti, M.; Sagnelli, C.; Ciccozzi, A.; d'Ettorre, G.; Angeletti, S.; Borsetti, A.; Ciccozzi, M. Human Immunodeficiency Virus Type 2: The Neglected Threat. *J. Pathol.* **2021**, *10* (11), 1377.

137. Faria, N. R.; Hodges-Mameletzis, I.; Silva, J. C.; Rodés, B.; Erasmus, S.; Paolucci, S.; Ruelle, J.; Pieniazek, D.; Taveira, N.; Treviño, A.; Gonçalves, M. F.; Jallow, S.; Xu, L.; Camacho, R. J.; Soriano, V.; Goubau, P.; de Sousa, J. D.; Vandamme, A.-M.; Suchard, M. A.; Lemey, P. Phylogeographical Footprint of Colonial History in the Global Dispersal of Human Immunodeficiency Virus Type 2 Group A. *J. Gen. Virol.* **2012**, *93* (Pt 4), 889–899.

138. Campbell-Yesufu, O. T.; Gandhi, R. T. Update on Human Immunodeficiency Virus (HIV)-2 Infection. *Clin Infect Dis.*. **2011**, *52* (6), 780–787.

139. Azevedo-Pereira, J. M.; Santos-Costa, Q. HIV Interaction with Human Host: HIV-2 as a Model of a Less Virulent Infection. *AIDS Rev.* **2016**, *18* (1), 44–53.

140. Delling, U.; Reid, L. S.; Barnett, R. W.; Ma, M. Y.; Climie, S.; M Sumner-Smith; Sonenberg, N. Conserved Nucleotides in the TAR RNA Stem of Human Immunodeficiency Virus Type 1 Are Critical for Tat Binding and Trans Activation: Model for TAR RNA Tertiary Structure. *J. Virol.* **1992**, *66* (5), 3018–3025.

141. Dingwall, C.; Ingemar Ernberg; Gait, M. J.; Green, S. M.; Heaphy, S.; Karn, J.; Lowe, A. D.; Singh, M.; Skinner, M. A. HIV-1 Tat Protein Stimulates Transcription by Binding to a U-Rich Bulge in the Stem of the TAR RNA Structure. *EMBO J.* **1990**, *9* (12), 4145–4153.

142. Roy, S.; Delling, U.; Chen, C. H.; Rosen, C. A.; Sonenberg, N. A Bulge Structure in HIV-1 TAR

RNA Is Required for Tat Binding and Tat-Mediated Trans-Activation. *Genes Dev.* **1990**, *4* (8), 1365–1373.

143. Olenginski, L. T.; Dayie, T. K. Quantifying the Effects of Long-Range 13C-13C Dipolar Coupling on Measured Relaxation Rates in RNA. *J. Biomol. NMR.* **2021**, *75* (4-5), 203–211.

144. Vallurupalli, P.; Scott, L.; Williamson, J. R.; Kay, L. E. Strong Coupling Effects during X-Pulse CPMG Experiments Recorded on Heteronuclear ABX Spin Systems: Artifacts and a Simple Solution. *J. Biomol. NMR*. **2007**, *38* (1), 41–46.

145. Dayie, T. K.; Olenginski, L. T.; Taiwo, K. M. Isotope Labels Combined with Solution NMR Spectroscopy Make Visible the Invisible Conformations of Small-To-Large RNAs. *Chem Rev.* **2022**, *122* (10), 9357–9394.

146. Levitt, M. H. *Spin Dynamics: Basics of Nuclear Magnetic Resonance*, 2nd ed.; Wiley: Chichester, 2013; 573–625.

147. Fushman, D.; Cahill, S.; Cowburn, D. The Main-Chain Dynamics of the Dynamin Pleckstrin Homology (PH) Domain in Solution: Analysis of 15N Relaxation with Monomer/Dimer Equilibration. *J. Mol. Biol.* **1997**, *266* (1), 173–194.

148. Hall, J. B.; Fushman, D. Characterization of the Overall and Local Dynamics of a Protein with Intermediate Rotational Anisotropy: Differentiating between Conformational Exchange and Anisotropic Diffusion in the B3 Domain of Protein G. *J. Biomol. NMR.* **2003**, *27* (3), 261–275.

149. Hansen, A. L.; Al-Hashimi, H. M. Dynamics of Large Elongated RNA by NMR Carbon Relaxation. *JACS.* **2007**, *129* (51), 16072–16082.

150. Lakomek, N.; Kaufman, J. D.; Stahl, S. J.; Louis, J. M.; Grishaev, A.; Wingfield, P. T.; Bax, A. Internal Dynamics of the Homotrimeric HIV-1 Viral Coat Protein Gp41 on Multiple Time Scales. *Angew. Chem.* **2013**, *52* (14), 3911–3915.

151. Massi, F.; Peng, J. W. Characterizing Protein Dynamics with NMR R 1ρ Relaxation Experiments. *Methods Mol. Biol.* **2017**, *1688*, 205–221.

152. Lakomek, N.-A.; Ying, J.; Bax, A. Measurement of 15N Relaxation Rates in Perdeuterated Proteins by TROSY-Based Methods. *J. Biomol. NMR.* **2012**, *53* (3), 209–221.

153. Meiboom, S.; Gill, D. Modified Spin-Echo Method for Measuring Nuclear Relaxation Times. *RSI.*

1958, *29* (8), 688–691.

154. Carr, H. Y.; Purcell, E. M. Effects of Diffusion on Free Precession in Nuclear Magnetic Resonance Experiments. *Phys. Rev.* **1954**, *94* (3), 630–638.

155. McConnell, H. M. Reaction Rates by Nuclear Magnetic Resonance. *J. Chem. Phys.* **1958**, *28* (3), 430–431.

156. Carver, J. P.; Richards, R. E. A General Two-Site Solution for the Chemical Exchange Produced Dependence of T2 upon the Carr-Purcell Pulse Separation. *J. Magn. Reson.* **1972**, *6* (1), 89–105.

157. Beckwith, M. A.; Erazo-Colon, T.; Johnson, B. A. RING NMR Dynamics: Software for Analysis of Multiple NMR Relaxation Experiments. *J. Biomol. NMR.* **2020**, *75* (1), 9–23.

158. Kay, L. E.; Torchia, D. A.; Bax, A. Backbone Dynamics of Proteins as Studied by Nitrogen-15 Inverse Detected Heteronuclear NMR Spectroscopy: Application to Staphylococcal Nuclease. *Biochem.* **1989**, *28* (23), 8972–8979.

159. Stelzer, A. C.; Frank, A. T.; Kratz, J. D.; Swanson, M. D.; Gonzalez-Hernandez, M. J.; Lee, J.; Andricioaei, I.; Markovitz, D. M.; Al-Hashimi, H. M. Discovery of Selective Bioactive Small Molecules by Targeting an RNA Dynamic Ensemble. *Nat. Chem. Biol.* **2011**, *7* (8), 553–559.

160. Al-Hashimi, H. M.; Gosser, Y.; Gorin, A.; Hu, W.; Majumdar, A.; Patel, D. J. Concerted Motions in HIV-1 TAR RNA May Allow Access to Bound State Conformations: RNA Dynamics from NMR Residual Dipolar Couplings 1 1Edited by M. F. Summers. *J. Mol. Biol.* **2002**, *315* (2), 95–102.

161. Al-Hashimi, H. M.; Pitt, S. W.; Majumdar, A.; Xu, W.; Patel, D. J. Mg2+-Induced Variations in the Conformation and Dynamics of HIV-1 TAR RNA Probed Using NMR Residual Dipolar Couplings. *J. Mol. Biol.* **2003**, *329* (5), 867–873.

162. Pitt, S. W.; Majumdar, A.; Serganov, A.; Patel, D. J.; Al-Hashimi, H. M. Argininamide Binding Arrests Global Motions in HIV-1 TAR RNA: Comparison with Mg2+-Induced Conformational Stabilization. *J. Mol. Biol.* **2004**, *338* (1), 7–16.

163. Casiano-Negroni, A.; Sun, X.; Al-Hashimi, H. M. Probing Na^+-Induced Changes in the HIV-1 TAR Conformational Dynamics Using NMR Residual Dipolar Couplings: New Insights into the Role of Counterions and Electrostatic Interactions in Adaptive Recognition. *Biochem.* **2007**, *46* (22), 6525–6535.

164.Frank, A. T.; Stelzer, A. C.; Al-Hashimi, H. M.; Ioan Andricioaei. Constructing RNA Dynamical Ensembles by Combining MD and Motionally Decoupled NMR RDCs: New Insights into RNA Dynamics and Adaptive Ligand Recognition. *NAR.* **2009**, *37* (11), 3670–3679.

165.*Data & Reports*. *ACS*. https://www.acs.org/education/policies/acs-approval-program/data-reports.html.

166.Attionu SK, Dill R, Summers MF, Case DA, Marchant J, Dayie TK. Selective [9-^{15}N] Guanosine for Nuclear Magnetic Resonance Studies of Large Ribonucleic Acids. *Chembiochem*. **2025**, *26* (12), e202500206.

167. Kaul, M., Barbieri, C.M. and Pilch, D.S. Aminoglycoside-Induced Reduction in Nucleotide Mobility at the Ribosomal RNA A-Site as a Potentially Key Determinant of Antibacterial Activity. *JACS.* **2006,** *128* (4), 1261-1271.

168.Sharp PA. The centrality of RNA. *Cell* **2009**,*136,* 577–580.

169.Zhao B, Guffy SL, Williams B, Zhang Q. An excited state underlies gene regulation of a transcriptional riboswitch. *Nat ChemBiol*. **2017**,*13,* 968–974.

170.Palmer AG. NMR characterization of the dynamics of biomacromolecules. *Chem. Rev.* **2004**, *104*, 3623–3640.

171.Wagner G. NMR relaxation and protein mobility. *CurrOpinStructBiol*. **1993**, (3), 748–754.

172.Yamazaki T, Muhandiram R, Kay LE. NMR experiments for the measurement of carbon relaxation properties in highly enriched, uniformly 13C,15N-labeled proteins: application to 13Cα carbons. *J. Am. Chem. Soc*. **1994**, *116*, 8266–8278.

173.Peng JW, Wagner G. Mapping of the spectral densities of N-H bond motions in Eglin c using heteronuclear relaxation experiments. *Biochem*. **1992**, *31*, 8571–8586.

174.Abragam A. Principles of nuclear magnetism. *Oxford: Clarendon Press*, **1961.**

175.Kloiber, K., Spitzer, R., Tollinger, M., Konrat, R., & Kreutz, C. Probing RNA dynamics via longitudinal exchange and CPMG relaxation dispersion NMR spectroscopy using a sensitive 13C-methyl label. *NAR.* **2011**, *39* (10), 4340–4351.

176.Alexander Rich and David R. Davies *JACS.* **1956,** *78* (14), 3548-3549.

177.Kim, S. H., Quigley, G. J., Suddath, F. L., McPherson, A., Sneden, D., Kim, J. J., Weinzierl, J., & Rich, A. Three-dimensional structure of yeast phenylalanine transfer RNA: folding of the polynucleotide chain. *Sci.* **1973,** *179* (4070), 285–288.

178.Morris, G. A., & Freeman, R. “Enhancement of Nuclear Magnetic Resonance Signals by Polarization Transfer.” *JACS.* **1979,** *101* (3), 760–762.

179.Rule, G. S.; Hitchens, T. K. *Fundamentals of Protein NMR Spectroscopy*; Springer: Dordrecht, 2005; 328;445.

180. Levitt, M. H. *Spin Dynamics: Basics of Nuclear Magnetic Resonance*, 2nd ed.; Wiley: Chichester, 2008; 336–337.

181.Levitt, M. H. *Spin Dynamics: Basics of Nuclear Magnetic Resonance*, 2nd ed.; Wiley: Chichester, 2008; 33–40.

182.Rule, G. S.; Hitchens, T. K. *Fundamentals of Protein NMR Spectroscopy*; Springer: Dordrecht, 2006; 431–474.

183.Levitt, M. H. *Spin Dynamics: Basics of Nuclear Magnetic Resonance*, 2nd ed.; Wiley: Chichester, 2013; 606–608.

184.Levitt, M. H. *Spin Dynamics: Basics of Nuclear Magnetic Resonance*, 2nd ed.; Wiley: Chichester, 2008; 198–200.

185.Marcotrigiano, Joseph *et al*. Cocrystal Structure of the Messenger RNA 5′ Cap-Binding Protein (eIF4E) Bound to 7-methyl-GDP. *Cell* **1997**, *89* (6), 951-961.

186.Heping Zheng, Ivan G. Shabalin, Katarzyna B. Handing, Janusz M. Bujnicki, Wladek Minor, Magnesium-binding architectures in RNA crystal structures: validation, binding preferences, classification and motif detection, *NAR.* **2015**, *43* (7), 3789–3801.

187.Leonarski, F., D'Ascenzo, L., & Auffinger, P. Mg2+ ions: do they bind to nucleobase nitrogens?. *NAR.* **2017**, *45* (2), 987–1004.

188.Leontis, N. B.; Westhof, E. Geometric nomenclature and classification of RNA base pairs. *RNA.* **2001**, *7* (4), 499–512.

189.Johnson, S. J.; Beese, L. S. Structures of mismatch replication errors observed in a DNA polymerase. *PNAS.* **2004**, *101* (16), 6070–6075.

190. Rangadurai, A., Al-Hashimi, H. M. *et, al*. Dynamics of Hoogsteen base pairs in RNA duplexes revealed by NMR relaxation dispersion. *NAR.* **2020**, *48* (17), 9721–9736.

191. Fay, M. M.; Lyons, S. M.; Ivanov, P. RNA G-quadruplexes in biology: principles and molecular mechanisms. *NAR.* **2017**, *45* (22), 12656–12668.

192. Lin, C.; Yang, D. Human telomeric G-quadruplex structures and their small-molecule ligands: insights into folding topology and ligand binding. *Mol.* **2017**, *22* (10), 1586.

193. Lech, C. J.; Heddi, B.; Phan, A. T. Guanine base stacking in G-quadruplex nucleic acids. *NAR.* **2013**, *41* (3), 2034–2046.

194. Levic J., Micura R., Beilstein. Syntheses of ^{15}N-labeled pre-queuosine nucleobase derivatives. *J. Org. Chem*. **2014**, *10*, 1914.

195. Bieri, M.; Gooley, P. Automated NMR relaxation dispersion data analysis using NESSY. *BMC Bioinform*. **2011,** *12, 421.*